Theoretical Investigations of Heavy Quarkonium Production in Photon-Photon Collisions

Dissertation
zur Erlangung des Doktorgrades
des Fachbereichs Physik
der Universität Hamburg

vorgelegt von
Luminita Mihaila
aus Racari

Hamburg
2002

Gutachter der Dissertation:	Prof. Dr. B. A. Kniehl Prof. Dr. J. Bartels
Gutachter der Disputation:	Prof. Dr. B. A. Kniehl Prof. Dr. G. Kramer
Datum der Disputation:	10.12.2002
Vorsitzender des Prüfungsausschusses:	Prof. Dr. G. Mack
Dekan des Fachbereichs Physik Vorsitzender des Promotionausschusses:	Prof. Dr. F.-W. Büßer

ABSTRACT

We present a theoretical analysis of J/Ψ-meson production in photon-photon collisions within the factorization formalism of Non-Relativistic Quantum Chromodynamics. We include the full next-to-leading-order corrections to the direct process and leading order contributions from single- and double-resolved photons. Our predictions are nicely confirmed by recent experimental data from the DELPHI collaboration at CERN LEP2, while those obtained within the traditional Colour-Singlet Model are disfavoured. The next-to-leading-order cross sections for the direct production of J/Ψ-mesons in association with photons and jets are of comparable size. Since the latter process does not occur within the Colour-Singlet Model, its experimental observation with the predicted production rates would provide evidence for the existence of colour-octet processes in nature.

ZUSAMMENFASSUNG

In dieser Arbeit stellen wir eine theoretische Behandlung der Produktion von J/Ψ-Mesonen in Photon-Photon-Streuung im Rahmen des Faktorisierungsformalismus der nichtrelativistischen Quantenchromodynamik vor. Dies beinhaltet die Berechnung der Korrekturen zur direkten Photon-Photon-Streuung in nächstführender Ordnung in α_s, sowie die Berechnung der Beiträge durch aufgelöste Photonen in führender Ordnung. Die daraus resultierenden Vorhersagen des Farb-Oktett-Modells sind in bemerkenswerter Übereinstimung mit den neuesten experimentellen Daten von LEP2 (CERN), während diejenigen des Farb-Singlett-Modells hierzu im Widerspruch stehen. Weiterhin sind die errechneten Wirkungsquerschnitte der direkten J/Ψ-Produktion in Verbindung mit einerseits Photonen und andererseits Jets in nächstführender Ordnung von vergleichbarer Größe. Da die Produktion von J/Ψ-Mesonen mit Jets im Farb-Singlett-Modell nicht erlaubt ist, wäre eine experimentelle Beobachtung dieses Prozesses ein glänzender Beweis für die Existenz von Farb-Oktett Zuständen in der Natur.

Contents

1 Introduction **1**

1.1 Motivation for studying J/Ψ physics 1

1.2 Physics of bound states in QED and QCD 2

1.2.1 QED 2

1.2.2 QCD 3

1.3 Purpose and outline of this work 4

2 Non-Relativistic Quantum Chromodynamics **5**

2.1 NRQCD as an effective field theory 5

2.1.1 Effective Lagrangian of NRQCD 6

2.1.2 Annihilation into light partons 9

2.1.3 Production from light partons 10

2.2 Projector formalism and Fock state decomposition 12

2.3 Renormalization group equation for operator matrix elements 17

3 J/Ψ production in two-photon collisions at leading order **23**

3.1 Born cross section 24

3.1.1 Phase space for $2 \to 1$ and $2 \to 2$ processes 24

3.1.2 Partonic cross section 27

3.1.3 Hadronic cross section 28

3.2 Direct processes 32

3.3 Single-resolved processes 36

3.4 Double-resolved processes 40

3.5 Comparison with DELPHI data 44

4 Virtual corrections **49**

4.1 Renormalization scheme 50

4.1.1 Heavy-quark self-energy 51

4.1.2 Gluon self-energy . . . 53
4.1.3 Strong coupling constant renormalization . . . 54
4.2 Virtual corrections to $\gamma\gamma \to c\bar{c}[\,^3S_1^{[1]}\,] + \gamma$ . . . 55
4.2.1 Cancellation of UV-, IR-, and Coulomb-singularities . . . 57
4.3 Virtual corrections to $\gamma\gamma \to c\bar{c}[^3S_1^{[1]}] + g$ . . . 59
4.3.1 Cancellation of the divergences . . . 62

5 Real Corrections **65**
5.1 Real corrections to $\gamma\gamma \to c\bar{c}[n] + \gamma$ . . . 72
5.1.1 Soft gluon emission . . . 74
5.1.2 Complete NLO corrections to $\gamma\gamma \to c\bar{c}[^3S_1^{[1]}] + \gamma$ . . . 76
5.2 Real corrections to $\gamma\gamma \to c\bar{c}[n] + g$ . . . 77
5.2.1 Soft-collinear limit of $\gamma\gamma \to c\bar{c}[^3S_1^{[1,8]}] + gg$ . . . 80
5.2.2 Infra-red limit of the process $\gamma\gamma \to c\bar{c}[^3S_1^{[8]}] + q\bar{q}$ . . . 83
5.2.3 Complete NLO corrections to $\gamma\gamma \to c\bar{c}[^3S_1^{[8]}] + g$ . . . 84

6 Numerical analysis **87**
6.1 NLO analysis of the process $\gamma\gamma \to J/\Psi + \gamma$ . . . 87
6.2 NLO analysis of the process $\gamma\gamma \to J/\Psi + g$ . . . 92
6.3 LO analysis of the process $\gamma\gamma \to J/\Psi + 2$ jets . . . 97

7 Conclusions **105**

A Colour algebra **107**

B NRQCD operators **111**
B.1 Order α_s corrections to NRQCD operators . . . 113

C Scalar integrals **117**
C.1 Abelian five-point integrals . . . 119
C.2 Non-Abelian five-point integrals . . . 122

D Angular integrals **125**

Chapter 1

Introduction

1.1 Motivation for studying J/Ψ physics

Since its discovery in 1974, the J/ψ meson has provided a useful laboratory for quantitative tests of Quantum Chromodynamics (QCD) and, in particular, of the interplay between perturbative and non-perturbative phenomena. The factorization formalism of Non-Relativistic QCD (NRQCD) provides a rigorous theoretical framework for the description of heavy-quarkonium production and decay [1]. This formalism implies a separation of short-distance coefficients, which can be calculated perturbatively as expansions in the strong coupling constant α_s, from long-distance matrix elements, which must be extracted from experiment. The relative importance of the latter can be estimated by means of velocity scaling rules, *i.e.* the matrix elements are predicted to scale with a definite power of the heavy-quark (Q) velocity v in the limit $v \ll 1$. In this way, the theoretical predictions are organized as double expansions in α_s and v. A crucial feature of this formalism is that it takes into account the complete structure of the $Q\overline{Q}$ Fock space, which is spanned by the states ${}^{2S+1}L_J^{[a]}$ with definite spin S, orbital angular momentum L, total angular momentum J, and colour multiplicity $a = \underline{1}, \underline{8}$. In particular, this formalism predicts the existence of colour-octet processes in nature. This means that $Q\overline{Q}$ pairs can be produced at short distances in colour-octet states and subsequently evolve into physical (colour-singlet) quarkonia by the non-perturbative emission of soft gluons. In the limit $v \to 0$, the traditional Colour-Singlet Model (CSM) [2, 3] is recovered. The greatest triumph of the NRQCD formalism was that it was able to correctly describe the cross section of inclusive charmonium production in $p\overline{p}$ collisions at the Fermilab Tevatron [4, 5, 6] and in $\gamma\gamma$ collisions at CERN LEP2 [7, 8], which had turned out to be more than one order of magnitude in excess of the theoretical prediction based on the CSM.

In order to convincingly establish the phenomenological significance of the colour-octet processes, it is indispensable to identify them in other kinds of high-energy experiments as well. Studies of charmonium production in ep photoproduction, ep and νN deep-inelastic scattering, e^+e^- annihilation, $\gamma\gamma$ collisions, and b-hadron decays may be found in the literature [see Refs [9, 10]]. Furthermore, the polarization of charmonium, which also provides a sensitive probe of colour-octet processes, was investigated [11, 12, 13]. None of these studies was able to prove or disprove the NRQCD factorization hypothesis. On the one hand, the theoretical predictions to be compared with existing experimental data are, apart from very few exceptions [14, 15, 16], of lowest order (LO) and thus suffer from considerable uncertainties, mostly from the dependences on the renormalization and factorization scales and from the lack of information on the non-perturbative matrix elements. On the other hand, the experimental errors are still rather sizeable. The latter will be dramatically reduced with the upgrades of DESY HERA and the Fermilab Tevatron and with the advent of CERN LHC and hopefully a future e^+e^- linear collider (LC) such as DESY TESLA. On the theoretical side, it is necessary to calculate the next-to-leading-order (NLO) corrections to the hard-scattering cross sections and to include the effective operators which are suppressed by higher powers in v.

1.2 Physics of bound states in QED and QCD

1.2.1 QED

Atoms like muonium ($\bar{\mu}e$) or positronium ($\bar{e}e$) are described quite accurately by simple non-relativistic quantum mechanics, particularly if the Coulomb potential is augmented by various corrections of the Pauli Hamiltonian [17]. Higher accuracy can be achieved by somehow incorporating the covariant perturbation theory of Quantum Electrodynamics (QED). Schwinger [18] and Bethe and Salpeter [19] accomplished this by reformulating the bound state problem in terms of covariant Green functions [known as Bethe-Salpeter Eqs] (BSE). They abandoned non-relativistic quantum mechanics in favour of the relativistic field theory. Corrections to muonium hyperfine splitting up to order α^2 and corrections to the decay rate of orthopositronium up to order α were computed in Refs [20, 21].

However, the BSE, while elegant, have proven quite difficult to be applied in high precision calculations, primarily because they are relativistic equations applied to a non-relativistic problem. These formulations take only little advantage of the radical differences between the physics at non-relativistic momenta and that at relativistic momenta. An alternative solution to the bound state problem was proposed by Caswell and Lep-

age [22], that greatly simplifies the computations. In principle, this approach can be applied to any non-relativistic problem [*i.e.*. low-energy scattering, infrared singularities, etc.]. Rather than replacing non-relativistic quantum mechanics, Caswell and Lepage introduced a new non-relativistic effective theory called Non-Relativistic Quantum Electrodynamics (NRQED). This effective field theory is constructed so that it involves only non-relativistic momenta and reproduces the low-momentum behaviour of QED to any desired accuracy. It adopts a renormalization group strategy and isolates contributions from relativistic and non-relativistic momentum scales. The form of the action in NRQED is uniquely determined by the symmetries and the particle content of the theory. The contributions from QED that involve relativistic loop momenta are absorbed by renormalization of the coupling constant of the various local interactions in NRQED. This is possible since the wavelengths associated with relativistic momenta are much shorter than those associated with non-relativistic momenta, and consequently any effects due to relativistic loop momenta can be described by local interactions. The coupling constants that appear are determined by matching conditions, requiring that the predictions of NRQED agree with those of QED to any desired accuracy. This implies on the one hand the evaluation of on-shell scattering amplitudes in QED. At this step bound states do not enter, only relativistic loop momenta contribute, and the Feynman gauge is the appropriate gauge to be used. On the other hand the properties of the bound states are computed in NRQED. Since only the non-relativistic momenta are present, the convenient gauge is the Coulomb gauge.
Such an approach makes no specific approximation, so that it can be used to study non-relativistic systems in any relativistic field theory. It was extended by Bodwin, Braaten and Lepage [1] to Quantum Chromodynamics .

1.2.2 QCD

One of the earliest applications of perturbative QCD was the calculation of the light hadronic and electromagnetic decay rates of S-wave quarkonia [23]. The calculation was based on the assumption that the annihilation of the heavy quark and anti-quark is a short distance process which, because of the asymptotic freedom of QCD, can be computed in perturbation theory. It was assumed that non-perturbative effects could be factored into $R_S(0)$, the non-relativistic wave function at the origin. The justification for such an assumption was that effects at different energy scales can be factorized. A heavy quark and anti-quark bound state is characterized by two distance scales: (a) its mean radius r_c of the order of 1 fm, at which the effective coupling strength for the binding becomes large

and the perturbative analysis breaks down, and (b) the Compton wavelength of the constituents or their inverse mass $1/M_c$. If $1/M_c$ is much shorter than r_c, the binding effects can be factored out from the annihilation or production process, which are essentially local relative to r_c. This approach is known as the Colour Singlet Model (CSM) [2, 3]. This assumption has been supported by subsequent calculations beyond the leading order [23]. Using a similar approach in the case of P-waves one might expect to be able to calculate their decay rates into light hadrons in terms of a single non-perturbative parameter $R'_P(0)$, the derivative of the non-relativistic wave function at the origin. Explicit calculations at order α_s^3 reveal that infrared divergences are left over [24]. This is a clear indication of sensitivity to non-perturbative effects beyond those contained in $R'_P(0)$.

The CSM has been superseded by a consistent and rigorous framework based on NRQCD [1], that includes the so-called colour octet mechanism. Despite the recent theoretical and experimental developments, the range of applicability of the different approaches is still subject to debate. Because the quarkonium mass is still not very large with respect to the QCD scale, in particular for the charmonium system, non-factorizable power corrections may not be sufficiently suppressed and the NRQCD expansion may not converge very well. In this respect, a global analysis of various processes is necessary to assess the importance of different quarkonium production mechanisms as well as the limitations of particular theoretical frameworks.

1.3 Purpose and outline of this work

Our main goal is to study the production of J/Ψ meson in two-photon collisions, *i.e.* to test the validity of NRQCD, to compare theoretical predictions with the available CERN LEP2 data, and to make, within this framework, predictions for a future e^+e^- linear collider like DESY TESLA. Since we expect different features for J/Ψ production at various colliders, we divide this work into J/Ψ-production with small transverse momenta at CERN LEP2 and J/Ψ-production with large transverse momenta at DESY TESLA.

The NRQCD factorization approach to charmonium production is introduced in Chapter 2 together with the projector formalism, adapted for n-dimensional computations. Chapter 3 summarizes the LO NRQCD predictions for J/Ψ-production in two-photon collisions and confronts them with recent experimental data from CERN LEP2 data.The full (NLO-virtual and real) corrections for J/ψ production in direct photon-photon collisions are considered in Chapters 4 and 5. Chapter 6 presents numerical results for J/Ψ plus photon, one jet, or dijet-system production. Our conclusions are summarized in Chapter 7.

Chapter 2

Non-Relativistic Quantum Chromodynamics

2.1 NRQCD as an effective field theory

In the meson rest frame, the heavy quark and anti-quark are non-relativistic, with relative velocity $v \ll 1$ and relative momentum Mv. The annihilation or production of heavy quarks and anti-quarks can occur only within a distance of order $1/M$ *i.e.* off-shell by an amount of order M. This distance is much smaller than the size of the meson of order $1/(Mv)$. To solve the problem of such bound states, one can think about factorizing the effects from different momentum scales. This involves the separation of the relativistic production and annihilation ($p \sim M$) from non-relativistic binding effects ($p \sim Mv$). A particularly elegant approach for solving this problem is Non-Relativistic Quantum Chromodynamics (NRQCD), an effective field theory consisting of a non-relativistic Schrödinger field theory for the heavy quarks and anti-quarks and a typical relativistic field theory for the light quarks and gluons [1]. It starts from full QCD and at the first step a cutoff Λ of order M is introduced. This cutoff explicitly excludes relativistic heavy quarks from the theory, and light quarks and gluons with momenta of order M as well. This can be justified by the argument that the important momenta for non-perturbative effects of the binding are of order Mv or less. Of course, the relativistic states that are discarded do have some effects on the low energy physics of the theory. The relativistic intermediate states involving heavy quarks and anti-quarks are necessarily highly virtual. They can propagate only over distances of order $1/M$ that are point-like on the scale $1/(Mv)$ of the quarkonium structure. Their effects can be accurately reproduced by local interactions involving low-momentum scales. Such an argument cannot be applied to the virtual states

produced in the annihilation of a heavy quark and anti-quark pair into light partons, since they are not necessarily far from their mass shell. The effects of relativistic light partons, excluded in this ultraviolet cutoff formulation, cannot be reproduced in detail. Nevertheless, the total annihilation width, the total production rate or any other sufficiently inclusive observables can be described accurately.

Generalizing standard renormalization procedures, one can systematically compensate for the removal of the relativistic states by adding new local interactions to the Lagrangian. To leading order in $1/M$, these new interactions are identical in form to interactions already present, and so the net effect is simply to shift bare masses and charges. Beyond leading order in $1/M$, one must extend the Lagrangian to include non-renormalizable interactions that correct the low-energy dynamics order by order in $1/M$. In this reformulation of QCD, all effects that arise from relativistic states are incorporated into the renormalization of the coupling constants of the extended Lagrangian. Thus, in the cutoff theory, relativistic and non-relativistic contributions are automatically separated. This separation is known as the *Factorization Approach* and is the basis for all recent analyses of the annihilation and production of heavy quarkonium.

2.1.1 Effective Lagrangian of NRQCD

One could in principle construct an effective Lagrangian that describes the low-energy $Q\bar{Q}$ sector of QCD by starting with the full Lagrangian and carrying out two transformations:

- make a renormalization group transformation that removes modes with momenta greater than a cutoff Λ.
- make a transformation that removes interactions that change the numbers of heavy quarks and anti-quarks.

Both of these steps are very complicated to carry out in practice. Fortunately, there is an alternative to explicitly constructing the effective Lagrangian and that is the strategy of *Effective Field Theory*. In this approach the construction of the Lagrangian proceeds through the following steps:

- Identify the required fields to describe the low-energy sector of the theory.
- Identify the symmetries that one can maintain in the effective theory.
- Specify the accuracy to which low-energy observables computed in the original theory should be reproduced by the effective theory.

- Write down the most general Lagrangian that is allowed by the symmetry constraints and that achieves the specified level of accuracy.
- Determine the coefficients by matching low-energy observables of the effective theory with those of the full theory.

The symmetries that are still present in an effective theory play a very important role in the construction of the effective Lagrangian. For NRQCD they are as follows:

- $SU(3)$ *gauge symmetry.* Gluon fields enter into the effective Lagrangian only through the gauge covariant derivatives D_t and $\mathbf{D}$.
- *rotational symmetry.* Heavy quarks are non-relativistic and this necessarily breaks down the Lorentz symmetry of QCD to its rotational subgroup.
- *charge conjugation and parity.*

  The charge conjugation transformations of the heavy quark and anti-quarks fields are

$$\Psi \to i\,(\chi^\dagger \sigma_2)^T \quad \text{and} \quad \chi \to -i\,(\Psi^\dagger \sigma_2)^T.$$

  The parity transformations of the heavy quark and anti-quark fields are

$$\Psi(t,\mathbf{r}) \to \Psi(t,-\mathbf{r}) \quad \text{and} \quad \chi(t,\mathbf{r}) \to -\chi(t,-\mathbf{r}).$$

- *heavy-quark phase symmetry.* This imposes the conservation of the number of heavy quarks and anti-quarks *separately.* Its action on the fields is

$$\Psi \to e^{i\,\alpha}\,\Psi \quad , \quad \chi \to e^{i\,\beta}\,\chi.$$

- *heavy-quark spin symmetry.* The two spin components of the heavy quark and anti-quark are mixed by independent unitary transformations:

$$\Psi \to U\,\Psi \quad , \quad \chi \to V\,\chi,$$

  where U and V are $SU(2)$ matrices. This is only an approximate symmetry, holding up to relative corrections of order v^2.

The most general effective Lagrangian consistent with these symmetries can be written as

$$\mathcal{L}_{NRQCD} = \mathcal{L}_{light} + \mathcal{L}_{heavy} + \delta\mathcal{L}, \tag{2.1}$$

with

$$\mathcal{L}_{light} = -\frac{1}{2}\, G_{\mu\nu}\, G^{\mu\nu} + \sum_{q=1}^{n_f} \bar{q}\, i\, \not{D} q, \tag{2.2}$$

where $G_{\mu\nu}$ is the gluon field-strength tensor, q is the Dirac spinor field for the light quarks, $D^\mu = \partial^\mu + i\ g\ A^\mu$ where $A^\mu = (\phi, \mathbf{A})$ is the $SU(3)$ gauge field, g is the QCD coupling constant, the sum is over the n_f flavours of light quarks, and

$$\mathcal{L}_{heavy} = \Psi^\dagger \left(iD_t + \frac{\mathbf{D}^2}{2M} \right) \Psi + \chi^\dagger \left(iD_t + \frac{\mathbf{D}^2}{2M} \right) \chi, \tag{2.3}$$

where Ψ is the Pauli spinor field that annihilates a heavy quark, χ is the Pauli spinor field that creates a heavy anti-quark, and D_t and $\mathbf{D}$ are the time and space components of the gauge covariant derivative D^μ. The relativistic effects are reproduced through the correction term $\delta\mathcal{L}$ in the Lagrangian. The level of accuracy is specified by the order in v with which the energy levels of quarkonium must be reproduced. The terms already shown in $\mathcal{L}_{NRQCD}$ give an accuracy of the energy levels of order Mv^4. A redefinition of the field Ψ (χ) can be used to eliminate terms in which D_t acts on Ψ (χ), as is shown below. Because of these redefinitions, NRQCD will not reproduce the low-energy behaviour of Green's functions of QCD. It will only agree with full QCD for on-shell quantities. The minimal form of NRQCD is obtained by setting $\delta\mathcal{L} = 0$. It contains two parameters: the heavy-quark mass M and coupling constant g. These parameters can be tuned as functions of the QCD coupling constant α_s, the heavy-quark mass parameter m_Q, and the ultraviolet cutoff Λ of NRQCD, so that the splittings between the quarkonium energy levels are reproduced up to errors of order Mv^4.

If one wishes to reduce the errors in the quarkonium energy levels below Mv^4, it is necessary to add additional terms in $\delta\mathcal{L}$. It can be shown that to reduce the errors to order Mv^6, it is necessary and sufficient to take these terms to be :

$$\begin{aligned}
\delta\, \mathcal{L}_{bilin} &= \frac{c_1}{8\, M^3} \left[\Psi^\dagger\, (\mathbf{D}^2)^2\, \Psi - \chi^\dagger\, (\mathbf{D}^2)^2\, \chi \right] \\
&+ \frac{c_2}{8\, M^2} \left[\Psi^\dagger\, (\mathbf{D}\cdot\ g\, \mathbf{E} - g\, \mathbf{E}\cdot\ \mathbf{D}) \Psi + \chi^\dagger\, (\mathbf{D}\cdot\ g\, \mathbf{E} - g\, \mathbf{E}\cdot\ \mathbf{D}) \chi \right] \\
&+ \frac{c_3}{8\, M^2} \left[\Psi^\dagger\, (i\mathbf{D}\times\ g\, \mathbf{E} - g\, \mathbf{E}\times\ i\, \mathbf{D}) \cdot \boldsymbol{\sigma}\, \Psi + \chi^\dagger\, (i\mathbf{D}\times\ g\, \mathbf{E} - g\, \mathbf{E}\times\ i\, \mathbf{D}) \cdot \boldsymbol{\sigma}\, \chi \right] \\
&+ \frac{c_4}{8\, M} \left[\Psi^\dagger\, (g\, \mathbf{B}\cdot\boldsymbol{\sigma}) \Psi + \chi^\dagger\, (g\, \mathbf{B}\cdot\boldsymbol{\sigma}) \chi \right],
\end{aligned} \tag{2.4}$$

where $E^i = G^{0i}$ and $B^i = \frac{1}{2}\epsilon^{i\,j\,k}, G^{j\,k}$ are the electric and the magnetic components of the gluon field-strength tensor $G^{\mu\,\nu}$. Mixed two-fermion operators involving $\chi^\dagger$ and Ψ (or

$\Psi^\dagger$ and χ) correspond to the annihilation (or the creation) of a $Q\bar{Q}$ pair. Such terms are excluded from the Lagrangian as part of the definition of NRQCD. The effects of such annihilation or creation processes on low-energy amplitudes can be reproduced by adding four-fermion operators such as $\Psi^\dagger\chi\chi^\dagger\Psi$ to the effective Lagrangian.

2.1.2 Annihilation into light partons

As was explained in the last Section, the annihilation of a $Q\bar{Q}$ pair cannot be described accurately within NRQCD. Nevertheless, the annihilation rate (given to the squared amplitude summed over all final states) can be precisely described. Since the annihilation of a $Q\bar{Q}$ pair occurs within a distance of order $1/M$ the annihilation contributes to a low-energy $Q\bar{Q} \to Q\bar{Q}$ scattering. It can be mimicked within NRQCD by local 4-fermion operators that annihilate a pair of $Q\bar{Q}$ at the space-time point (x_1) and recreate it at another space-time point (x_2), so that the numbers of heavy quarks and anti-quarks are individually conserved. The optical theorem relates the annihilation rate to the imaginary parts of the $Q\bar{Q} \to Q\bar{Q}$ scattering amplitudes. This implies that the coefficients of $\delta\mathcal{L}$ must have imaginary parts and that is the manifestation of the annihilation in NRQCD.

Using Fierz's decomposition relations [25] over colour and spin subspaces [App. A and B], one can rewrite the generic 4-fermionic operators $\Psi^\dagger\Psi\chi^\dagger\chi$ as

$$\begin{aligned}\Psi^\dagger\Psi\chi^\dagger\chi &= \frac{1}{2\,N_c}\left(\Psi^\dagger\chi\chi^\dagger\Psi + \Psi^\dagger\sigma^i\chi\cdot\chi^\dagger\sigma^i\Psi\right)\\ &+ \Psi^\dagger\,T^a\chi\,T^a\chi^\dagger\Psi + \Psi^\dagger\,T^a\sigma^i\chi\,T^a\sigma^i\chi^\dagger\Psi. \qquad (2.5)\end{aligned}$$

One can identify the following operators:

$$\begin{aligned}\mathcal{O}_1[^1S_0] &= \frac{1}{2\,N_c}\,\Psi^\dagger\chi\chi^\dagger\Psi,\\ \mathcal{O}_1[^3S_1] &= \frac{1}{2\,N_c}\,\Psi^\dagger\sigma^i\chi\chi^\dagger\sigma^i\Psi,\\ \mathcal{O}_8[^1S_0] &= \Psi^\dagger\,T^a\chi\,T^a\chi^\dagger\Psi,\\ \mathcal{O}_8[^3S_1] &= \Psi^\dagger\,T^a\sigma^i\chi\,T^a\sigma^i\chi^\dagger\Psi, \qquad (2.6)\end{aligned}$$

where the subscript 1 or 8 indicates the colour structure, the arguments $^{2\,S+1}L_J$ indicate the spin and the angular-momentum state of the $Q\bar{Q}$ pair. Using the velocity-scaling rules [26, 27] all these operators scale like M^6 [called dim-6 operators]. Introducing also the spatial part of the covariant derivatives inside these operators, one obtains the P-wave operators that scale like M^8 [see App. A and B]. The normalization of the operators agrees with Ref. [15] and differs from Ref. [1] by a factor $1/(2\,N_c)$ for colour-singlet operators.

As can be understood from Eq. (2.5), the colour-singlet and colour-octet operators are introduced together, and it is natural to treat them on an equal footing. This is in contrast to the CSM, which selects only the colour-singlet operators (corresponding to the projection onto the dominant Fock state of a quarkonium state H). The way in which we have introduced these operators shows that they are corrections to the LO Lagrangian, and the velocity scaling-rules provide us with their dependence on v^2. It is the balance between the suppression in v^2 and the enhancement in α_s, coming from the hard scattering, which will decide on the dominant contributions for a given heavy-quark state and a hard process. Note that there is no *a priori* motivation to exclude the colour-octet operators in favour of the colour-singlet ones. In the non-perturbative evolution from the on-shell $Q\bar{Q}$ pair to a bound state, soft gluons will be emitted, which change the colour, spin and angular momentum of the $Q\bar{Q}$ system.

The 4-fermion interactions, representing annihilation in NRQCD, have the general form

$$\delta\mathcal{L}_{4-fermion} = \sum_n \frac{f_n(\Lambda)}{M^{d_n-4}}\,\mathcal{O}_n(\Lambda), \tag{2.7}$$

where $\mathcal{O}_n(\Lambda)$ denotes the local 4-fermion operator listed in App. B. With the help of the optical theorem, we recall that the annihilation rate is $(-2\times)$ the imaginary part of the energy,

$$\Gamma(H \to LH) = 2\ \mathrm{Im}\langle\ H|\delta\mathcal{L}_{4-fermion}|H\ \rangle, \tag{2.8}$$

where LH represents all possible light-hadron final states. This can also be written as

$$\Gamma(H \to LH) = \sum_n \frac{2\ \mathrm{Im}\ f_n(\Lambda)}{M^{d_n-4}}\ \langle\ H|\delta\mathcal{L}_{[n]}|H\ \rangle. \tag{2.9}$$

The coefficients Im $f_n(\Lambda)$ are proportional to the annihilation rate of the initial configuration into light quarks and gluons, and can be computed as a perturbation series in $\alpha_s(M)$. The operator-matrix elements give the probability for finding the heavy quark and anti-quark in the meson in a quantum state with specified colour, spin and angular-momentum quantum numbers [1]. The dependence on the arbitrary factorization scale Λ cancels between the coefficients and the operators.

2.1.3 Production from light partons

As in the case of the annihilation width, we wish to write the production rate as a sum of terms, consisting of a short-distance part, that can be computed in perturbative QCD,

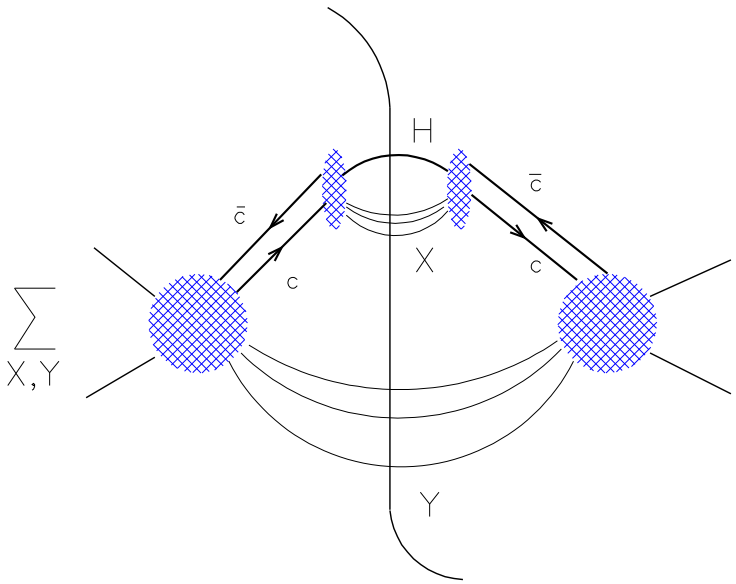

Figure 2.1: Diagrammatic representation of quarkonium bound state production.

and a long-distance part that can be expressed as a matrix element in NRQCD. Such a factorized formulation is based on the cancellation of IR-divergences at all orders of perturbation theory for sufficiently inclusive processes. The derivation of this separation of physics at different scales is usually done in two steps. In the first step, called *topological factorization*, one separates the effects of the *hard* momentum scale of order $Q = M$ from those of the *soft* momentum scale $\Lambda_{QCD} = Mv^2$. This step is similar to the usual factorization methods of perturbative QCD and is also valid for a choice of the hard momentum scale of order M. The additional step is required to separate effects of scale M from those of scale Mv, and is called *NRQCD factorization*.

In Ref. [15] there is a pictorial representation of the first step, which is also reproduced in Fig. 2.1. After cancellations between real- and virtual-soft gluons, one can identify the following structure for a dominant cut-diagram :

- *Hard-scattering sub-diagrams* (to the left and to the right hand side of the cut). They describe the production of the on-shell heavy quark pair within a distance of order $1/M$ and some additional hard partons. The outgoing $Q\bar{Q}$ pair has a small relative momentum of order Mv.

- *jet-like sub-diagram* Y. This consists of single hard parton lines, that extend through the cut and connect the two hard sub-diagrams.

- *Quarkonium sub-diagram.* This also extends through the cut and is attached to the hard sub-diagrams by Q and $\bar{Q}$ lines. It contains the quarkonium bound state and some soft partons produced during the binding process.

For sufficiently inclusive production processes, the Kinoshita-Lee-Nauenberg (KLN) theorem states that the soft-gluon exchanges between jet-like sub-diagrams and quarkonium sub-diagrams cancel, and their effect on the production rate can be neglected [28]. With this constraint satisfied in the cut-diagram, all effects of the hard scale can be factored into hard-scattering sub-diagrams, while all effects of the soft scale Λ_{QCD} are factored into jet-like and quarkonium sub-diagrams. After this first step, effects of the momentum scale Mv are distributed between the hard-scattering diagram (through the Q and $\bar{Q}$ propagators) and the quarkonium diagram (through the gluons with momentum of order $q = Mv$ that are responsible for the binding process). A simple way to disentangle the momentum scale Mv from the hard-scattering sub-diagrams is to make a Taylor expansion in the relative momentum Mv of the heavy quark and anti-quark and then to absorb all resulting Mv-dependent functions into the quarkonium sub-diagrams. Each term in the Taylor series corresponds to a local operator that creates a $Q\bar{Q}$ pair from the vacuum.

2.2 Projector formalism and Fock state decomposition

Assuming the validity of the factorization theorem, production of a quarkonium in the hadronic state H can be expressed as

$$\mathcal{M} = \mathcal{T}_{i\,j}(Q\bar{Q} \;+\; Y)\langle H\; X|\Psi^\dagger\chi|0\rangle, \tag{2.10}$$

where $\mathcal{T}_{i\,j}$ is the matrix element for the hard-scattering sub-diagrams to produce an on-shell heavy-quark and anti-quark pair and some additional, hard partons, and $\langle H\; X|\Psi^\dagger\chi|0\rangle$ is the projection of the the final hadronic state $Q\bar{Q}$ onto the space of states containing the quarkonium state H and unspecified hadrons.
Summing over a complete set of $Q\bar{Q}$ states, one obtains

$$\begin{aligned}\mathcal{M} &= \sum_n \mathcal{T}_{i\,j}(Q\bar{Q} \;+\; Y)\langle H\; X|Q\;\bar{Q}[n]\rangle\langle Q\;\bar{Q}[n]|\Psi^\dagger\chi|0\rangle \\ &\equiv \sum_n \langle H\; X|Q\;\bar{Q}[n]\rangle Tr[\mathcal{T}\;\Pi^{[n]}] = \sum_n \langle H\; X|Q\;\bar{Q}[n]\rangle\mathcal{A}_{[n]},\end{aligned} \tag{2.11}$$

where $\Pi^{[n]}$ selects the colour, spin and angular-momentum quantum numbers of the quark pair, $\langle H\;\; X|Q\;\;\bar{Q}[n]\rangle$ is the probability amplitude that the quark pair in the state $[n]$

hadronize into the quarkonim state H. We can express the quark pair state $|Q\ \bar{Q}[n]\rangle$ with the help of a creation bilinear operator [see App. A and B] as

$$|Q\bar{Q}[n]\rangle = \Psi^\dagger \mathcal{K}_n \chi|0\rangle \equiv \mathcal{O}^\dagger_{bilin}[n]|0\rangle \quad , \quad \langle H\ X|Q\ \bar{Q}[n]\rangle = \langle H\ X|\mathcal{O}^\dagger_{bilin}[n]|0\rangle, \quad (2.12)$$

$$\langle Q\bar{Q}[n]| = \langle 0|\chi^\dagger \mathcal{K}'_n \Psi \equiv \langle 0|\mathcal{O}_{bilin}[n] \quad , \quad \langle Q\ \bar{Q}[n]|H\ X\rangle = \langle 0|\mathcal{O}_{bilin}[n]|H\ X\rangle. \quad (2.13)$$

Introducing these definitions into the expression for the squared-matrix element, we obtain

$$|\mathcal{M}|^2 \ \sim \ \sum_n \sum_X \sum_{m_J, col} \langle H\ X|Q\ \bar{Q}[n]\rangle\langle Q\ \bar{Q}[n]|H\ X\rangle |\mathcal{A}_{[n]}|^2. \quad (2.14)$$

It is useful to define the projector onto the sub-space of states containing quarkonium states H,

$$\mathcal{P}^H = \sum_X \sum_{m_J, colour} |H\ X\rangle\langle H\ X|. \quad (2.15)$$

The quarkonium state H is specified by its colour, spin, angular momentum and total angular momentum quantum numbers, and the previous sums are over the final states X, the colour and the $2\ J+1$ spin degrees of freedom. With the projector defined as before, it is convenient to rewrite the first factor in the sum (2.14) as

$$\begin{aligned} & \sum_X \sum_{m_J, colour} \langle Q\ \bar{Q}[n]|H\ X\rangle\langle H\ X|Q\ \bar{Q}[n]\rangle \\ = & \sum_X \langle 0|\mathcal{O}_{bilin}[n]|H\ X\rangle\langle H\ X|\mathcal{O}^\dagger_{bilin}[n]|0\rangle \\ = & \ \langle 0|\mathcal{O}_{bilin}[n]\mathcal{P}^H\mathcal{O}^\dagger_{bilin}[n]|0\rangle \equiv \ \langle \mathcal{O}^H[n]\rangle. \end{aligned} \quad (2.16)$$

Now, we can write the expression for the total cross section as a sum of terms, which can be expressed as a product of a short-distance hard-scattering cross section and the expectation value of an operator that describes non-perturbative binding effects:

$$d\sigma(H+X) = \sum_n d\hat{\sigma}(Q\bar{Q}[n]+X)\langle \mathcal{O}^H[n]\rangle, \quad (2.17)$$

where $d\hat{\sigma}(Q\bar{Q}[n]+X)$ is computed in perturbative QCD and $\langle \mathcal{O}^H[n]\rangle$ gives the probability for a $Q\bar{Q}$ pair in state $[n]$ to form an H particle. The latter is determined either in NRQCD or treated as phenomenological parameters.

This formalism takes into account the complete structure of the Fock space. The sum is over all states $[n]$ that can produce an H particle. To compute $d\sigma(H+X)$, one should consider not only the dominant Fock state $Q\bar{Q}$, which has the same quantum numbers as the particle H, but also higher Fock states that contain additional gluons or $q\bar{q}$ pairs. For example, the most important contributions to J/Ψ particle production are

$$
\begin{aligned}
|J/\Psi\rangle \quad &= \quad \Psi^{J/\Psi}|c\bar{c}[^3S_1^{[1]}]\rangle + \Psi_g^{J/\Psi}|c\bar{c}[^3P_J^{[8]}] + g\rangle \\
&+ \quad \Psi_g^{J/\Psi}|c\bar{c}[^1S_0^{[8]}] + g\rangle + \Psi_{gg}^{J/\Psi}|c\bar{c}[^3S_1^{[8]}] + gg\rangle + ... \qquad (2.18)
\end{aligned}
$$

The heavy-quark pair, produced at the hard scale, can be either in a colour-singlet or in a colour-octet state, but they evolve non-perturbatively into a physical state emitting soft gluons. The wavelengths of the gluons are much larger than the dimension of the bound state $1/Mv$ or the hard interaction distances $1/M$, and they cannot be described in QCD. Rather than QCD we should apply the multipole expansion technique. The probability that a higher Fock state evolves into a physical state can be estimated using the *velocity-scaling rules* [26, 27].

In the Coulomb gauge, the scalar potential does not propagate, and the dynamical gluons are created and annihilated by the vector potential $\mathbf{A}$. Using velocity-scaling rules, we can organize $\mathcal{L}_{NRQCD}$ as an expansion in powers of v. At order v^0 there is no coupling between $\mathbf{A}$ and Ψ or χ, so that the probabilities of higher Fock states are suppressed by powers of v. The $|Q\bar{Q}g\rangle$ states with the highest probability are those that couple to the dominant $|Q\bar{Q}\rangle$ state via order v^1 of the Lagrangian $\mathcal{L}_{NRQCD}$:

$$
\mathcal{L}_1 = -\frac{1}{M}\Psi^\dagger(ig\mathbf{A}\cdot\nabla)\Psi + \frac{c_4}{2M}\Psi^\dagger(\nabla\times g\mathbf{A})\cdot\boldsymbol{\sigma}\Psi + charge\ conjugate. \qquad (2.19)
$$

- We first consider the term $\Psi^\dagger(ig\mathbf{A}\cdot\nabla)\Psi$ and refer to the corresponding transition that proceeds through this term as an *electric transition*. Such a transition from the dominant $|Q\bar{Q}\rangle$ state to a $|Q\bar{Q}g\rangle$ will change the angular momentum quantum numbers of the $Q\bar{Q}$, satisfying selection rules $\Delta L = \pm 1, \Delta S = 0$. The probability of this transition scale with v^2 can be deduced from Table 2.1.

- We next consider the term $\Psi^\dagger(\nabla\times g\mathbf{A})\cdot\boldsymbol{\sigma}\Psi$ and refer to a transition that proceeds via this term as a *magnetic transition*. A magnetic transition from the dominant $|Q\bar{Q}\rangle$ state to a $|Q\bar{Q}g\rangle$ will change the spin of the $Q\bar{Q}$ pair and satisfy selection rules like $\Delta L = 0, \Delta S = \pm 1$. The probability of this transition scales with v^4.

Similar arguments can be used to determine the magnitude of the probability for other Fock states. Any such state can be reached by a sequence of electric and magnetic transitions. Both electric and magnetic transitions change the colour state of $Q\bar{Q}$, since the gauge boson is a coloured object: the soft gluon.

As can be seen from factorization formulae, the hard-scattering cross section $d\hat{\sigma}(Q\bar{Q}[n] + X)$ is computed in perturbative QCD as an expansion in power of α_s, and the

$\langle \mathcal{O}^H[n] \rangle$ matrix elements are organized in NRQCD as an expansion in powers of v^2. Thus we can conclude that the cross section $d\sigma(H+X)$ is a double expansion in α_s and v^2. While QCD provides rigorous quantitative predictions, NRQCD provides only a hierarchy, so that the matrix elements $\langle \mathcal{O}^H[n] \rangle$ should be treated as phenomenological parameters.

Table 2.1: Velocity-Scaling Rules

Operator	Estimate
ψ, χ	$(Mv)^{3/2}$
D_t	Mv^2
$\vec{D}$	Mv
$g\vec{E}$	M^2v^3
$g\vec{B}$	M^2v^4
gA_0 (Coulomb gauge)	Mv^2
$g\vec{A}$ (Coulomb gauge)	Mv^3

The short-distance cross sections in (2.17) contain QCD projectors $\Pi^{[n]}$ that select colour, spin and angular-momentum quantum numbers. They have been known since some time ago [29] and have been used since then in analyses of quarkonium production and decay. Ref. [15] extended them to D-dimensions so that they can be used also in computations that involve dimensional regularization. These QCD projectors can be split into:

- *Colour projectors*- separate colour-singlet and colour-octet states

$$C_1 = \frac{\delta_{ij}}{\sqrt{N_C}} \qquad C_8 = \sqrt{2}T^c_{ij}. \tag{2.20}$$

- *Spin projectors*- create Π_0 spin-singlet and Π_1^α spin-triplet states

$$\Pi_0 = \frac{1}{\sqrt{8m^3}}(\frac{P}{2} - q - m)\gamma_5(\frac{P}{2} + q + m), \tag{2.21}$$

$$\Pi_1^\alpha = \frac{1}{\sqrt{8m^3}}(\frac{P}{2} - q - m)\gamma^\alpha(\frac{P}{2} + q + m). \tag{2.22}$$

Using these projectors and equation (2.12), one can express the amplitude for the hard scattering processes, as is shown below. The sums over final polarizations of quarkonium are also listed since they are used in the computation of squared aplitudes (they select the appropriate total angular momentum quantum numbers).

- Spin singlet S states ${}^1S_0$:

$$\mathcal{A}_{S=0,L=0} \;=\; \mathrm{Tr}[C\,\Pi_0\,\mathcal{A}]|_{q=0} \tag{2.23}$$

- Spin triplet S states (${}^3S_1$):

$$\mathcal{A}_{S=1,L=0} \;=\; \epsilon_\alpha \mathrm{Tr}[C\,\Pi_1^\alpha\,\mathcal{A}]|_{q=0} \tag{2.24}$$

$$\sum_{J_z} \epsilon_\alpha \epsilon^*_{\alpha'} = \Pi_{\alpha\,\alpha'} \quad ; \quad N_{^3S_1} = \sum_{J_z} \epsilon_\alpha \epsilon^*_\alpha = \Pi_{\alpha\,\alpha} = D-1 = 3-2\,\epsilon \tag{2.25}$$

- Spin singlet P states (${}^1P_1$):

$$\mathcal{A}_{S=0,L=1} \;=\; \epsilon_\beta \frac{\mathrm{d}}{\mathrm{d}\,q_\beta} \mathrm{Tr}[C\,\Pi_0\,\mathcal{A}]|_{q=0} \tag{2.26}$$

- Spin triplet P states (${}^3P_J$):

  $J=0$

$$\mathcal{A}_{S=1,L=1} = \varepsilon_{\alpha\,\beta} \frac{\mathrm{d}}{\mathrm{d}\,q_\beta} \mathrm{Tr}[C\,\Pi_1^\alpha\,\mathcal{A}]|_{q=0} \tag{2.27}$$

$$\varepsilon^{(0)}_{\alpha\,\beta} \varepsilon^{(0)\,*}_{\alpha'\,\beta'} = \frac{1}{D-1} \Pi_{\alpha\,\beta} \Pi_{\alpha'\,\beta'} \;\; ; \;\; N_0 = \varepsilon^{(0)}_{\alpha\,\beta} \varepsilon^{(0)\,*}_{\alpha\,\beta} = 1 \tag{2.28}$$

  $J=1$

$$\sum_{J_z} \varepsilon^{(1)}_{\alpha\,\beta} \varepsilon^{(1)\,*}_{\alpha'\,\beta'} = \frac{1}{2} \left[\Pi_{\alpha\,\alpha'} \Pi_{\beta\,\beta'} + \Pi_{\alpha\,\beta'} \Pi_{\alpha'\,\beta}\right]$$

$$N_1 = \sum_{J_z} \varepsilon^{(1)}_{\alpha\,\beta} \varepsilon^{(1)\,*}_{\alpha\,\beta} = \frac{(D-1)\,(D-2)}{2} = (3-2\,\epsilon)\,(1-\epsilon) \tag{2.29}$$

  $J=2$

$$\sum_{J_z} \varepsilon^{(2)}_{\alpha\,\beta} \varepsilon^{(2)\,*}_{\alpha'\,\beta'} = \frac{1}{2}\,\left[\Pi_{\alpha\,\alpha'} \Pi_{\beta\,\beta'} + \Pi_{\alpha\,\beta'} \Pi_{\alpha'\,\beta}\right] - \frac{1}{D-1} \Pi_{\alpha\,\beta} \Pi_{\alpha'\,\beta'}$$

$$N_2 = \sum_{J_z} \varepsilon^{(2)}_{\alpha\,\beta} \varepsilon^{(2)\,*}_{\alpha\,\beta} = \frac{(D+1)\,(D-2)}{2} = (5-2\,\epsilon)\,(1-\epsilon) \tag{2.30}$$

These amplitudes will then be squared, summed over the final degrees of freedom and averaged over the initial ones to obtain the short-distance cross section $d\,\hat{\sigma}(Q\bar{Q}[n]+X)$. This can be written as

$$d\,\hat{\sigma}(i\;j \to Q\bar{Q}[{}^{2\,S+1}L_J^{[1,8]}] + X) \;=\; \frac{1}{2\;s} \overline{\sum}_{colour,spin} \sum_{m_J} |\mathcal{A}_{S,L}|^2\; d\Phi, \tag{2.31}$$

where s is the partonic centre-of-mass energy squared and $d\Phi$ is the n-body phase space, n being the number of the final state particles. The matrix element $\langle \mathcal{O}^H[n] \rangle$ includes the sum over the colour and the $2\ J+1$ total angular-momentum states. If we use $SU(3)$ symmetry for the colour sub-space and rotational invariance, we can assume that NRQCD operator matrix elements (OMEs) are identical for all colour and total angular momentum degrees of freedom. We can now write squared matrix elements as

$$|\mathcal{M}|^2 \sim \sum_n \sum_{colour,spin} \sum_{m_J} |\mathcal{A}_{[n]}|^2 \frac{\langle \mathcal{O}^H_{[1,8]}[^{2S+1}L_J] \rangle}{N_{col} N_{pol}}. \tag{2.32}$$

This is useful for recovering the exact expression for the short-distance cross section $d\ \hat{\sigma}(ij \to Q\bar{Q}[^{2\ S+1}L_J^{[1,8]}] + X)$, in which all final degrees of freedom are summed over. Taking this into account, the factorization formula given in Eq. (2.17) becomes:

$$d\sigma(ij \to Q\bar{Q}[^{2S+1}L_J^{[1,8]}] + X) = d\hat{\sigma}(ij \to Q\bar{Q}[^{2S+1}L_J^{[1,8]}] + X) \frac{\langle \mathcal{O}^H_{[1,8]}[^{2S+1}L_J] \rangle}{N_{col} N_{pol}}, \tag{2.33}$$

where $N_{col} = N_c^2 - 1$ and N_{pol} have been introduced in Eq. (2.24-2.30).

2.3 Renormalization group equation for operator matrix elements

Within the NRQCD factorization approach one can find rigorous solutions for the cancellation of Infra-Red- (IR) or Coulomb-singularities. This cancellation can be done by taking into account loop corrections to the NRQCD operators matrix elements. Since we are dealing with loop corrections, we need a regularization scheme to remove divergences present in the theory. We impose the cutoff by using a mass independent regularization scheme, such as dimensional regularization. We have used the technique used in Ref. [15], to explicitly introduce radiative corrections to the NRQCD operators rather than matching between cross sections computed both in full QCD and NRQCD. We focus now on the one-loop corrections to the scattering amplitudes of the operator $\langle \mathcal{O}_8[^3S_1] \rangle$. We consider the amplitude for the scattering of a $Q\bar{Q}$ pair with momenta $\mathbf{p}$ and $-\mathbf{p}$ into a pair with momenta $\mathbf{p}'$ and $-\mathbf{p}'$ with $|\mathbf{p}| = |\mathbf{p}'|$. We shall use a compact notation with suppressed Pauli spinors to write the operators corresponding to the leading-order diagrams as :

$$\mathcal{O}_1[^1S_0] = (\frac{1}{\sqrt{N_c}} \otimes \frac{1}{\sqrt{N_c}})(\frac{1}{\sqrt{2}} \otimes \frac{1}{\sqrt{2}}),$$
$$\mathcal{O}_8[^1S_0] = (\sqrt{2}T^a \otimes \sqrt{2}T^a)(\frac{1}{\sqrt{2}} \otimes \frac{1}{\sqrt{2}}),$$

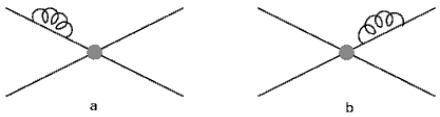

Figure 2.2: Feynman diagrams in NRQCD for the self-energy corrections of a heavy-quark line, that contribute to the evolution of an S-wave four-fermion operator.

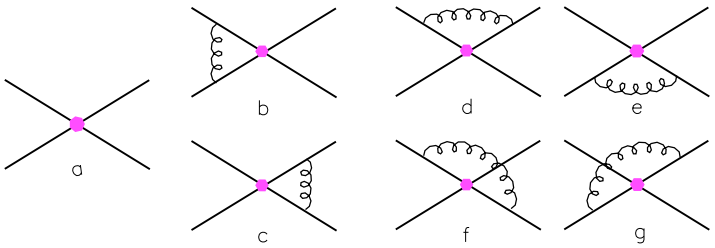

Figure 2.3: Feynman diagrams in NRQCD for vertex-corrections that contribute to the evolution of an S-wave four-fermion operator.

$$\mathcal{O}_1[^3S_1] = (\frac{1}{\sqrt{N_c}} \otimes \frac{1}{\sqrt{N_c}})(\frac{\sigma^i}{\sqrt{2}} \otimes \frac{\sigma^i}{\sqrt{2}}),$$
$$\mathcal{O}_8[^3S_1] = (\sqrt{2}T^a \otimes \sqrt{2}T^a)(\frac{\sigma^i}{\sqrt{2}} \otimes \frac{\sigma^i}{\sqrt{2}}). \tag{2.34}$$

The one-loop corrections include: (i) self-energy insertions to the four heavy quark lines shown in Fig. 2.2 and (ii) vertex-correction diagrams shown in Fig. 2.3, and the corresponding one-loop corrections to S-wave operators have all the same scalar structure. It is convenient to chose the Coulomb gauge to compute contributions coming from all diagrams shown in Fig. 2.2 and Fig. 2.3, because in this gauge one can split the gluon propagator into two pieces: a transverse part,

$$G^{\mu\nu}_{trans}(k^2) = -\frac{i}{k^2}\left(g^{\mu\nu} + \frac{k^\mu k^\nu}{\mathbf{k}^2}\right)(1-\delta_{\mu\,0})(1-\delta_{\nu\,0}) = -\frac{i}{k^2}\left(\delta^{ij} - \frac{k^i k^j}{\mathbf{k}^2}\right), \tag{2.35}$$

and a longitudinal (Coulomb) part,

$$G^{\mu\nu}_{Coul}(k^2) = \frac{i}{k^2}\delta_{\mu\,0}\delta_{\nu\,0}. \tag{2.36}$$

The transverse part is responsible for ultra-violet and infra-red divergences in all the diagrams shown in Fig. 2.2 and Fig. 2.3. The Coulomb part is responsible for the Coulomb singularities that arise from diagrams 2.3(b-c).

- Coulomb gluon exchange

  Using NRQCD Feynman rules in the meson rest frame, where the 4-vector momenta of the incoming Q, $\bar{Q}$ heavy quark and anti-quark and of the exchanged gluon g can be written as $p_Q = (p_0, \mathbf{p})$, $p_{\bar{Q}} = (p_0, -\mathbf{p})$ and $(k_0, \mathbf{k})$, and the subsequent on-shell condition $p_0 = \mathbf{p}^2/2M$, we get for the Coulomb gluon exchange in diagram 2.3.b

$$I_b^{Coul} = -i\, g_s^2 \int \frac{d^4k}{(2\pi)^4} \frac{1}{\mathbf{k}^2} \, \frac{1}{p_0 + k_0 - \frac{(\mathbf{p}+\mathbf{k})^2}{2\,M} + i\epsilon} \, \frac{1}{p_0 - k_0 - \frac{(\mathbf{p}+\mathbf{k})^2}{2\,M} + i\epsilon}. \tag{2.37}$$

  And similarly, for the diagram 2.3.c, we get

$$I_c^{Coul} = -i\, g_s^2 \int \frac{d^4k}{(2\pi)^4} \frac{1}{\mathbf{k}^2} \, \frac{1}{p_0 + k_0 - \frac{(\mathbf{p}'-\mathbf{k})^2}{2\,M} + i\epsilon} \, \frac{1}{p_0 - k_0 - \frac{(\mathbf{p}'-\mathbf{k})^2}{2\,M} + i\epsilon}. \tag{2.38}$$

  The integration over k_0 can be performed by contour integration, closing the loop in the lower half of the complex k_0 plane and picking up the pole at $k_0 = -p_0 + (\mathbf{p}+\mathbf{k})^2/2\,M - i\epsilon$ and $k_0 = -p_0 + (\mathbf{p}'-\mathbf{k})^2/2\,M - i\epsilon$. We furthermore obtain

$$\begin{aligned} I_b^{Coul} &= g_s^2 \int \frac{d^3k}{(2\pi)^3} \frac{1}{\mathbf{k}^2} \, \frac{1}{\mathbf{k}^2 + 2\mathbf{p}\cdot\mathbf{k} - i\epsilon}, \\ I_c^{Coul} &= g_s^2 \int \frac{d^3k}{(2\pi)^3} \frac{1}{\mathbf{k}^2} \, \frac{1}{\mathbf{k}^2 - 2\mathbf{p}'\cdot\mathbf{k} - i\epsilon}. \end{aligned} \tag{2.39}$$

  The last two integrals are divergent, and they must be performed using some regularization technique. As was mentioned above, dimensional regularization is a convenient one for NRQCD. Using the definitions $\mathbf{v} = \mathbf{p}/m$,$\mathbf{v}' = \mathbf{p}'/m$ and $v = |\mathbf{v}| = v' = |\mathbf{v}'|$, we find:

$$\begin{aligned} I_b^{Coul} = \frac{g_s^2}{4\pi} \frac{\pi^2\, M}{4\,|\mathbf{p}|} (1 + i \cdot IR_{div.}) \quad &, \quad I_c^{Coul} = \frac{g_s^2}{4\pi} \frac{\pi^2\, M}{4\,|\mathbf{p}'|} (1 - i \cdot IR_{div.}) \,, \\ I_b^{Coul} + I_c^{Coul} \quad &= \quad \frac{\pi\, \alpha_s}{2\, v}. \end{aligned} \tag{2.40}$$

  A longitudinal gluon exchange does not modify the spin, angular-momentum and colour structure of these operators, except for a colour prefactor defined in App. B

$$\mathcal{C}_{[1]} = C_F \quad , \quad \mathcal{C}_{[8]} = -\frac{1}{2\, N_c}. \tag{2.41}$$

  The overall Coulomb correction to the operator matrix element is therefore

$$\langle \mathcal{O}_{[1,8]}[n] \rangle = \langle \mathcal{O}_{[1,8]}[n] \rangle_{born} \left(1 + \mathcal{C}_{[1,8]} \frac{\pi\, \alpha_s}{2\, v} \right). \tag{2.42}$$

  The Coulomb divergences, which introduce order α_s corrections to the NRQCD operators, cancel exactly against those arising from the virtual corrections, as shown

in Chapter 4. Using renormalized NRQCD operators, one can rigorously prove the cancellation of Coulomb singularities, in contrast with the empirical approach used previously, to absorb them into Bethe-Salpeter wave functions.

- Transverse gluon exchange

  Using the relation (2.34) and the above introduced definitions we find two types of contributions: (i) those arising from the diagrams shown in Fig.2.2(a,b) and in Fig.2.3(b,c), in which the transverse gluon is exchanged between incoming or outgoing heavy quark and anti-quark lines. Such an exchange does not modify the colour, spin and angular-momentum structure of the matrix elements, except for a v^2-dependent prefactor. The specific integrals have the form:

$$I_b^{trans} = ig_s^2 \int \frac{d^4k}{(2\pi)^4} \frac{\mathbf{p}\cdot\mathbf{p} - (\mathbf{p}\cdot\hat{\mathbf{k}})(\mathbf{p}\cdot\hat{\mathbf{k}})}{M^2(k_0^2 - \mathbf{k}^2 + i\epsilon)} \frac{1}{p_0 + k_0 - \frac{(\mathbf{p}+\mathbf{k})^2}{2\,M} + i\epsilon} \frac{1}{p_0 - k_0 - \frac{(\mathbf{p}+\mathbf{k})^2}{2\,M} + i\epsilon}.$$

  After performing a contour integration over k_0 around $k_0 = \mathbf{k} - i\epsilon$ pole, we find

$$I_b^{trans} = -g_s^2 \int \frac{d^3k}{(2\pi)^3} \frac{\mathbf{p}\cdot\mathbf{p} - (\mathbf{p}\cdot\hat{\mathbf{k}})(\mathbf{p}\cdot\hat{\mathbf{k}})}{2M^2\mathbf{k}} \frac{1}{|\mathbf{k}| - \frac{\mathbf{k}^2}{2M} - \frac{\mathbf{p}\cdot\mathbf{k}}{M} + i\epsilon} \frac{1}{|\mathbf{k}| + \frac{\mathbf{k}^2}{2M} + \frac{\mathbf{p}\cdot\mathbf{k}}{M} - i\epsilon}.$$

  Since the NRQCD is valid only at small values of $\mathbf{p}/M$, $\mathbf{p}'/M$, and $\mathbf{k}/M$, it was argued [1] that the correct way to perform this integral is first to expand as a Taylor series in powers of $1/M$ and then integrate over $\mathbf{k}$. Keeping only the first term in the expansion, we find

$$I_b^{trans} = -\frac{g_s^2}{2M^2} \int \frac{d^3k}{(2\pi)^3} \frac{\mathbf{p}\cdot\mathbf{p} - (\mathbf{p}\cdot\hat{\mathbf{k}})(\mathbf{p}\cdot\hat{\mathbf{k}})}{|\mathbf{k}|^3}. \tag{2.43}$$

  This integral is ultra-violet and infra-red divergent so that we must perform it using dimensional regularization, and we find:

$$I_b^{trans} = -\frac{2\alpha_s}{3\pi} \frac{\mathbf{p}\cdot\mathbf{p}}{M^2} \frac{1}{2} \left(\frac{1}{\epsilon_{UV}} - \frac{1}{\epsilon_{IR}} \right) = -\frac{2\alpha_s}{3\pi} v^2 \, \frac{1}{2} \left(\frac{1}{\epsilon_{UV}} - \frac{1}{\epsilon_{IR}} \right). \tag{2.44}$$

  The same result is valid also for contributions coming from diagram shown in Fig. 2.3.c. A similar result is found for any diagram shown in Fig. 2.2:

$$I_a^{trans} = -\frac{2\alpha_s}{3\pi} \frac{\mathbf{p}\cdot\mathbf{p}}{M^2} \frac{1}{4} \left(\frac{1}{\epsilon_{UV}} - \frac{1}{\epsilon_{IR}} \right) = -\frac{2\alpha_s}{3\pi} v^2 \, \frac{1}{4} \left(\frac{1}{\epsilon_{UV}} - \frac{1}{\epsilon_{IR}} \right). \tag{2.45}$$

  In diagrams 2.3.(d-g), the transverse gluon is exchanged between an incoming heavy quark (anti-quark) and outgoing quark(anti-quark) lines. This modifies the colour and angular-momentum structure of the matrix elements, but does not modify the

spin structure. Using a similar technique to those described above, we get for these diagrams

$$I_d^{trans} = \frac{g_s^2}{2M^2}\int \frac{d^3k}{(2\pi)^3}\frac{\mathbf{p}\cdot\mathbf{p}' - (\mathbf{p}\cdot\hat{\mathbf{k}})(\mathbf{p}'\cdot\hat{\mathbf{k}})}{|\mathbf{k}|^3}, \tag{2.46}$$

and after performing the integration

$$I_d^{trans} = \frac{2\alpha_s}{3\pi}\frac{\mathbf{p}\cdot\mathbf{p}'}{M^2}\frac{1}{2}\left(\frac{1}{\epsilon_{UV}} - \frac{1}{\epsilon_{IR}}\right) = \frac{2\alpha_s}{3\pi}\mathbf{v}\cdot\mathbf{v}'\,\frac{1}{2}\left(\frac{1}{\epsilon_{UV}} - \frac{1}{\epsilon_{IR}}\right). \tag{2.47}$$

Using the above computed integrals and those established in App. A and B, we can express NRQCD operator matrix elements, including corrections up to order α_s, as follows:

$$\begin{aligned}\langle\mathcal{O}_8[^3S_1]\rangle &= \langle\mathcal{O}_8[^3S_1]\rangle_{born} + \frac{4\alpha_s}{3\pi M^2}\left(\frac{1}{\epsilon_{UV}} - \frac{1}{\epsilon_{IR}}\right)\\ &\times \left[C_F\sum_j\langle\mathcal{O}_1[^3P_J]\rangle + B_F\sum_j\langle\mathcal{O}_8[^3P_J]\rangle\right].\end{aligned} \tag{2.48}$$

The presence of UV-divergences indicates that the operators need renormalization. The suitable counterterm in the $\overline{\text{MS}}$ scheme is such that:

$$\begin{aligned}\langle\mathcal{O}_8[^3S_1]\rangle = \mu_\Lambda^{-2\epsilon}\Bigg\{&\langle\mathcal{O}_8[^3S_1]\rangle^{(\mu_\Lambda)} + \frac{4\alpha_s}{3\pi M^2}\left(\frac{1}{\epsilon_{UV}} + \ln 4\pi - \gamma_E\right)\\ &\times\left[C_F\sum_j\langle\mathcal{O}_1[^3P_J]\rangle + B_F\sum_j\langle\mathcal{O}_8[^3P_J]\rangle\right]\Bigg\},\end{aligned} \tag{2.49}$$

where μ_Λ is NRQCD renormalization scale.

$$\begin{aligned}\langle\mathcal{O}_8[^3S_1]\rangle_{born} &= \mu_\Lambda^{-2\epsilon}\langle\mathcal{O}_8[^3S_1]\rangle^{(\mu_\Lambda)} + \left(\frac{1}{\epsilon_{IR}} + \ln 4\pi - \gamma_E\right)\left(\frac{\mu}{\mu_\Lambda}\right)^{2\epsilon}\\ &\times \frac{4\alpha_s}{3\pi M^2}\left[C_F\sum_j\langle\mathcal{O}_1[^3P_J]\rangle + B_F\sum_j\langle\mathcal{O}_8[^3P_J]\rangle\right],\end{aligned} \tag{2.50}$$

where α_s is the renormalized strong coupling constant and μ is QCD renormalization scale. A similar expression can be written for the colour-singlet operator:

$$\begin{aligned}\langle\mathcal{O}_1[^3S_1]\rangle_{born} &= \mu_\Lambda^{-2\epsilon}\langle\mathcal{O}_1[^3S_1]\rangle^{(\mu_\Lambda)} + \left(\frac{1}{\epsilon_{IR}} + \ln 4\pi - \gamma_E\right)\left(\frac{\mu}{\mu_\Lambda}\right)^{2\epsilon}\\ &\times \frac{2\alpha_s}{3\pi M^2 N_c}\left[\sum_j\langle\mathcal{O}_8[^3P_J]\rangle\right].\end{aligned} \tag{2.51}$$

The renormalized operator matrix elements corresponding to $\langle \mathcal{O}_8[^1S_0] \rangle$ and $\langle \mathcal{O}_1[^1S_0] \rangle$ can be obtained in a similar way and they are listed in App. A and B. The renormalization of $\langle \mathcal{O}_8, 1[^3P_J] \rangle$ will involve higher order corrections in v^2 that are beyond the scope of this work. The IR-divergences that show up in order α_s corrections to the operator matrix elements in NRQCD will be exactly canceled by the left over IR-divergences in the short distance coefficients, as will be explicitly shown in Chapters 4 and 5. This ensures a well-defined overall result, which solves the inconsistencies of the CSM, specifically the fact that it is unable to explain NLO P-wave decays. Now we have a rigorous framework to study heavy quarkonium production and decay.

In the next Chapters we shall consider only J/Ψ meson production. This implies that the useful operators are S- and P-wave types. We shall not discuss furthermore about relativistic corrections to these operators any further.

Chapter 3

J/Ψ production in two-photon collisions at leading order

In this Chapter we make a leading order (LO) analysis of J/Ψ production in two-photon collisions, considering *direct, single- and double-resolved* processes. As we shall see in the last Section, this level of accuracy is sufficient to explain experimental data from CERN LEP2.

It was explained quite some time ago [30] that the photons can behave as point-like particles and couple directly to the quark lines, and this is called a *direct process*. At large momentum transfer, photons become *resolved* [31], in the sense that they do not behave anymore as point-like particles, but rather as composed objects, and they participate in the interactions through their quark and gluon constituents. If only one photon is resolved and the other one is direct, we refer to this process as *single-resolved*. If both photons are resolved, we refer to this as a *double-resolved process*. J/Ψ particles with relatively small transverse momenta can be produced in direct and resolved processes, because only a small fraction is required from the total available energy. This implies that the photon constituents can carry only a small fraction of the total photon momentum, where parton density functions (PDFs) reach their maximum values. At mild energies, single-resolved processes become dominant as was explained in Ref. [32] for CSM and in Ref. [33] for NRQCD. This sector has already been accessed at CERN LEP2 and, indeed, the experimental data show that 75% of the recorded events are generated in single-resolved processes. To obtain J/Ψ particles with large transverse momenta, a large amount of energy is necessary, which translates into large fractions of energy for the photon constituents (g, q). In this sector, the PDFs fall down rapidly. Although there is a partonic enhancement $\sim \alpha_s/\alpha$ of the resolved processes, we expect that the

PDF	$\langle O_1^{J/\psi}(^3S_1)\rangle$	$\langle O_8^{J/\psi}(^3S_1)\rangle$	$M_{3.4}^{J/\psi}$
MRST98LO	1.3 ± 0.1	4.4 ± 0.7	8.7 ± 0.9
CTEQ5L	1.4 ± 0.1	3.9 ± 0.7	6.6 ± 0.7
unit	GeV^3	$10^{-3}\mathrm{GeV}^3$	$10^{-2}\mathrm{GeV}^3$

Table 3.1: NRQCD matrix elements.

direct process will become dominant for large transverse momentum production. It is the balance between PDF evolution with the fraction of energy and the enhancement of the partonic cross section that selects between the two types of initial state processes.

3.1 Born cross section

In all analyses presented in this work, we use the Factorization Approach of NRQCD [see Chapter 2], that supposes a separation of the hard scattering process from the non-perturbative process of hadronization of the on-shell $c\bar{c}$ pair to a heavy quarkonium state. The hard scattering cross section is computed in perturbative QCD as an expansion in α_s and the long-distance process is described by the operators $\langle \mathcal{O}^H[n]\rangle$. We treat the latter as phenomenological parameters and we chose for our numerical analysis their values extracted from CDF-Tevatron by Ref. [13]. They are also listed in Table 3.1 and we use the same normalization as Ref. [15], where the colour-singlet operators are divided by $2N_c$.

We compute partonic and hadronic cross sections using the usual Feynman rules and the projector formalism described in Chapter 2, which ensures that the $c\bar{c}$ pair is produced with the specified quantum numbers $[n]$. For these processes, it is convenient to evaluate the gluon polarization sum as $\sum_{pol} \varepsilon_\mu(k)\varepsilon_\nu^*(k) = -g_{\mu\nu}$, at the expense of allowing for Fadeev-Popov ghosts of the gluon to appear at non-Abelian gluon vertices.

3.1.1 Phase space for $2 \to 1$ and $2 \to 2$ processes

We consider J/Ψ-particles in the non-relativistic approximation, *i.e.* the relative velocity between the charm quark c and anti-quark $\bar{c}$ in the meson rest-frame is neglected in all diagrams, except for those involving IR- or Coulomb-singularities. This can be expressed

as

$$p_c + p_{\bar{c}} = P_{J/\Psi} \qquad \boldsymbol{p}_c - \boldsymbol{p}_{\bar{c}} = 2m\mathbf{v} \simeq \mathbf{0}. \tag{3.1}$$

We will compute all LO processes in the Center-of-Mass Systems (CMS) of the incoming particles. For the analysis of the partonic system, we divide our computations into two parts.

- The $2 \to 1$ processes, like $a(k_1) + b(k_2) \to J/\Psi(P_{J/\Psi})$, are described by

  the n-dimensional momenta

$$\begin{aligned} k_1 &= (\omega_1, \cdots, 0, 0, \omega_1), \\ k_2 &= (\omega_1, \cdots, 0, 0, -\omega_1), \\ P_{J/\Psi} &= (E_{J/\Psi}, \cdots, 0, 0, 0), \end{aligned} \tag{3.2}$$

  the energy-momentum conservation laws and the on-shell conditions

$$\begin{aligned} k_1 + k_2 &= P_{J/\Psi}, \\ k_1^2 = k_2^2 &= 0, \\ P_{J/\Psi}^2 &= 4m_c^2 \equiv M_{J/\Psi}^2, \end{aligned} \tag{3.3}$$

  and the Mandelstam variables

$$\begin{aligned} s &= 2k_1 \cdot k_2, \\ s_1 &= s - 4m_c^2, \\ t_1 &= -2k_1 \cdot P_{J/\Psi}, \\ t &= t_1 + 4m_c^2, \\ u_1 &= -2k_2 \cdot P_{J/\Psi}, \\ u &= u_1 + 4m_c^2. \end{aligned} \tag{3.4}$$

  Using the on-shell conditions, we get the following relations for the Mandelstam variables

$$\begin{aligned} s &= 4m_c^2, \\ t_1 &= -4m_c^2, \\ u_1 &= -4m_c^2. \end{aligned} \tag{3.5}$$

- The $2 \to 2$ processes like $a(k_1) + b(k_2) \to J/\Psi(P_{J/\Psi}) + X(k_3)$ are characterized by the n-dimensional momenta (in the CMS of the incoming particles)

$$\begin{aligned} k_1 &= (\omega_1, \cdots, 0, 0, \omega_1), \\ k_2 &= (\omega_1, \cdots, 0, 0, -\omega_1), \\ P_{J/\Psi} &= (E_{J/\Psi}, \cdots, -\omega_3 \sin\chi\cos\phi, -\omega_3 \sin\chi \sin\phi, -\omega_3 \cos\chi), \\ k_3 &= (\omega_3, \cdots, \omega_3 \sin\chi\cos\phi, \omega_3 \sin\chi \sin\phi, \omega_3 \cos\chi), \end{aligned} \tag{3.6}$$

the energy-momentum conservation laws and the on-shell conditions

$$\begin{aligned} k_1 + k_2 &= P_{J/\Psi} + k_3, \\ k_1^2 &= k_2^2 = k_3^2 = 0, \\ P_{J/\Psi}^2 &= 4m_c^2 \equiv M_{J/\Psi}^2, \end{aligned} \tag{3.7}$$

and the Mandelstam variables

$$\begin{aligned} s &= 2k_1 \cdot k_2, \\ s_1 &= s - 4m_c^2, \\ t_1 &= -2k_1 \cdot P_{J/\Psi}, \\ t &= t_1 + 4m_c^2, \\ u_1 &= -2k_2 \cdot P_{J/\Psi}, \\ u &= u_1 + 4m_c^2. \end{aligned} \tag{3.8}$$

According to the Eq. (3.6) and Eq. (3.7) we have

$$\begin{aligned} \omega_1 &= \sqrt{s}/2, \\ \omega_3 &= \frac{s_1}{2\sqrt{s}}, \\ E_{J/\Psi} &= \frac{s + 4m_c^2}{2\sqrt{s}}. \end{aligned} \tag{3.9}$$

Using all these relations, we obtain

$$\begin{aligned} t_1 &= -2\omega_1(\, E_{J/\Psi} + \omega_3 \cos\chi\,), \\ u_1 &= -2\omega_1(\, E_{J/\Psi} - \omega_3 \cos\chi\,), \\ s + t + u &= 4m_c^2. \end{aligned} \tag{3.10}$$

3.1.2 Partonic cross section

To compute partonic cross sections of different kinds of processes we use the *Factorization Formula* expressed in Eq. (2.33) and the definition given in Eq. (2.31).

$$d\sigma(\ ij \to Q\bar{Q}[^{2S+1}L_J^{[1,8]}] + X\ ) \;=\; d\hat{\sigma}(\ ij \to Q\bar{Q}[^{2S+1}L_J^{[1,8]}] + X\ )\ \frac{\langle \mathcal{O}^H_{[1,8]}[^{2S+1}L_J]\rangle}{N_{col}N_{pol}}.$$

Another useful ingredient to compute $d\hat{\sigma}$ is the *phase space* for the various topologies involved. We again separate our calculations into two parts, corresponding to the $2 \to 1$ and to the $2 \to 2$ processes, respectively.

- The partonic cross section of a $2 \to 1$ process reads

$$\begin{aligned}
\hat{\sigma} &= K_s\ K_c\ \phi \int \frac{d^n P_{J/\Psi}}{(2\pi)^{n-1}} \delta_+(P^2_{J/\Psi} - 4m_c^2)(2\pi)^n \delta^{(n)}(k_1 + k_2 - P_{J/\Psi}) \sum_{col,pol} |\mathcal{M}_B|^2 \\
&= K_s\ K_c\ \phi\ (2\pi) \int \frac{d^{n-1} P_{J/\Psi}}{2P^0_{J/\Psi}} \delta^{(n)}(k_1 + k_2 - P_{J/\Psi}) \sum_{col,pol} |\mathcal{M}_B|^2 \\
&= K_s\ K_c\ \frac{2\pi}{2s} \frac{\delta(\ \sqrt{s} - 2m_c\ )}{2P^0_{J/\Psi}} \sum_{col,pol} |\mathcal{M}_B|^2 \\
&= K_s\ K_c\ \frac{\pi}{s} \delta(\ s - 4m_c^2\ ) \sum_{col,pol} |\mathcal{M}_B|^2, \qquad (3.11)
\end{aligned}$$

  where $\delta_+(k^2 - m^2) = \delta(k^2 - m^2)\Theta(m)$, K_s is the spin average factor and K_c is the colour average factor. Their explicit values are :

$$K_s^g = K_s^\gamma = \frac{1}{n-2} = \frac{1}{2(1-\epsilon)} \quad , \quad K_s^q = \frac{1}{2}, \qquad (3.12)$$

  and

$$K_c^g = \frac{1}{8} \ , \ K_c^\gamma = 1 \ , \ K_c^q = \frac{1}{3}. \qquad (3.13)$$

- The partonic cross section of a $2 \to 2$ process, in $n = 4 - 2\epsilon$ dimensions, can be written as

$$\begin{aligned}
\hat{\sigma} &= K_s\ K_c\ \phi\ \mu^{(4-n)} \int \frac{d^n P_{J/\Psi}}{(2\pi)^{n-1}} \int \frac{d^n k_3}{(2\pi)^{n-1}} \delta_+(P^2_{J/\Psi} - 4m_c^2)\delta_+(k_3^2) \\
&\times\ (2\pi)^n \delta^{(n)}(k_1 + k_2 - P_{J/\Psi} - k_3) \sum_{col,pol} |\mathcal{M}_B|^2
\end{aligned}$$

$$
\begin{aligned}
&= K_s\, K_c\, \phi\, \mu^{(4-n)} (2\pi)^{2-n} \int \frac{d^{n-1} P_{J/\Psi}}{2 P^0_{J/\Psi}} \int \frac{d^{n-1} k_3}{2 k^0_3} \\
&\times \delta^{(n)}(k_1 + k_2 - P_{J/\Psi} - k_3) \sum_{col,pol} |\mathcal{M}_B|^2 \\
&= K_s\, K_c\, \phi\, \mu^{(4-n)} (2\pi)^{2-n} \int \frac{d^{n-1} P_{J/\Psi}}{2 P^0_{J/\Psi}} \frac{1}{2 k^0_3} \delta(k^0_1 + k^0_2 - P^0_{J/\Psi} - k^0_3) \\
&\times \sum_{col,pol} |\mathcal{M}_B|^2, \qquad (3.14)
\end{aligned}
$$

where the mass parameter μ is introduced to keep the gauge couplings g and e dimensionless in n dimensions. Choosing the CMS defined in Eq. (3.6) and considering the relations between the J/Ψ four-momenta and the Mandelstam variables:

$$
\begin{aligned}
E_{J/\Psi} = -\frac{t_1 + u_1}{2\sqrt{s}} \quad , \quad \cos\chi = \frac{u_1 - t_1}{2\sqrt{s}\, p_{J/\Psi}}, \\
\left| \frac{\partial(E_{J/\Psi}, \cos\chi)}{\partial(t_1, u_1)} \right| = \frac{1}{2s\, p_{J/\Psi}}, \qquad (3.15)
\end{aligned}
$$

we get for the $2 \to 2$ phase space $d\, PS_2$ the following expression

$$
d\, PS_2 = \delta(\, s + t + u - 4m_c^2\,) \left(\frac{t\, u}{4\pi\mu^2 s} \right)^{\frac{n-4}{2}} \frac{1}{8\pi s} \frac{1}{\Gamma\left(\frac{n-2}{2}\right)} dt_1 du_1.
$$

We can now express the double differential cross section as

$$
\frac{d\hat{\sigma}}{dt_1 du_1} = \frac{\phi K_c}{8\pi s} \frac{K_s}{\Gamma(1-\epsilon)} \left(\frac{t\, u}{4\pi\mu^2 s} \right)^{\frac{n-4}{2}} \delta(s + t + u - 4m_c^2) \sum_{col,pol} |\mathcal{M}_B|^2, \qquad (3.16)
$$

and the single differential cross section as

$$
\frac{d\hat{\sigma}}{dt_1} = \frac{\phi K_c}{8\pi s} \frac{K_s}{\Gamma(1-\epsilon)} \left(\frac{t\, u}{4\pi\mu^2 s} \right)^{\frac{n-4}{2}} \sum_{col,pol} |\mathcal{M}_B|^2. \qquad (3.17)
$$

3.1.3 Hadronic cross section

We use the Weizsäcker-Williams approximation (WWA) [34] for the bremsstrahlung photon distribution from an electron

$$
f_{\gamma/e}(x) = \frac{\alpha}{2\pi} \left[\frac{1 + (1-x)^2}{x} \ln \frac{Q^2_{max}(1-x)}{m_e^2 x^2} + 2 m_e^2 x \left(\frac{1}{Q^2_{max}} - \frac{1-x}{m_e^2 x^2} \right) \right], \qquad (3.18)
$$

where $f_{\gamma/e}(x_\pm)$ is the equivalent number of transverse photons radiated by the initial-state positrons and electrons [35], $x = E_\gamma / E_e$ is the fraction of energy transferred from

the electron to the photon, $Q^2_{max} = E^2_e(1-x)\theta^2_{max}$ is the photon maximal virtuality, and θ_{max} is the angular cut that ensures the photon is real. Considering in addition to the WWA, factorization theorems of the QCD parton model [30] and the NRQCD factorization approach [1], the differential cross section of a process like $e^+e^- \to e^+e^-H + X$ can be written as follows

$$d\,\sigma(e^+e^- \to e^+e^-H + X) = \int dx_+ f_{\gamma/e}(x_+) \int dx_- f_{\gamma/e}(x_-)$$
$$\sum_{a,b,d} \int dx_a f_{a/\gamma}(x_a, M) \int dx_b f_{b/\gamma}(x_b, M) \sum_n d\hat{\sigma}(ab \to c\bar{c}[n] + d) \frac{\langle \mathcal{O}^H[n] \rangle}{N_{col} N_{pol}}, \qquad (3.19)$$

where $f_{a/\gamma}(x_a, M)$ are the PDFs of the photon, $\langle \mathcal{O}^H[n] \rangle$ are the OMEs of the H meson listed in Table 3.1 and $d\hat{\sigma}(ab \to c\bar{c}[n] + d)$ are the differential partonic cross sections discussed in the last Section. The integrals are over the longitudinal-momentum fractions of the emitted particles with respect to the emitting ones, and the sums are over $a, b = \gamma, g, q, \bar{q}$ and $d = g, q, \bar{q}$ with $q = u, d, s$. We include the $c\bar{c}$ Fock states $n = {}^3S_1^{[1]}, {}^1S_0^{[8]}, {}^3S_1^{[8]}, {}^3P_J^{[8]}$ if $H = J/\Psi, \Psi'$ and $n = {}^3P_J^{[1]}, {}^3S_1^{[8]}$ if $H = \chi_{cJ}$, where $J = 0, 1, 2$.

With the definition

$$f_{\gamma/\gamma}(x_\gamma, M) = \delta(1 - x_\gamma), \qquad (3.20)$$

Eq. (3.19) accommodates the direct, single-resolved, and double-resolved channels. The presence of parton d is to ensure that p_T can take finite values; if it were absent, then p_T would essentially be zero and it would describe a $2 \to 1$ process. With all these specifications, Eq. (3.19) is quite general, and it accounts for hadronic cross sections for all kinds of LO processes in e^+e^- collisions. This formula can also be written in a very similar form with the formula for the hadronic cross section in ep or $p\bar{p}$ collisions, and this is useful for making a corroboration of the behaviours seen at HERA (ep) and Tevatron ($p\bar{p}$) colliders, and establishing whether there is a dominant CO contribution in J/Ψ production.

We consider the following equivalence:

$$\int_0^1 dx_+ f_{\gamma/e}(x_+) \int_0^1 dx_a f_{a/\gamma}(x_a, M) = \int_0^1 dz_a f_{\gamma/e}(z_a/x_a) \int_{z_a}^1 \frac{dx_a}{x_a} f_{a/\gamma}(x_a, M)$$
$$= \int_0^1 dz_a \left[\int_{z_a}^1 \frac{dx_a}{x_a} f_{\gamma/e}(z_a/x_a) f_{a/\gamma}(x_a, M) \right] \equiv \int_0^1 dz_a F_{a/e}(z_a), \qquad (3.21)$$

where we have introduced $z_a \equiv x_+ \cdot x_a$ and have defined

$$F_{a/e}(z_a) \equiv \int_{z_a}^1 \frac{dx_a}{x_a} f_{\gamma/e}(z_a/x_a) f_{a/\gamma}(x_a, M). \qquad (3.22)$$

The $F_{a/e}(z_a)$ coincides with $f_{\gamma/e}(z_a)$ for unresolved photons. Introducing these notations in Eq. (3.19), we have

$$d\,\sigma(e^+e^- \to e^+e^- H + X) = \int_0^1 dz_a F_{a/e}(z_a) \int_0^1 dz_b F_{b/e}(z_b) \sum_n d\hat{\sigma}(ab \to c\bar{c}[n] + d) \frac{\langle \mathcal{O}^H[n] \rangle}{N_{col} N_{pol}}. \tag{3.23}$$

Hence modulo the difference in parton densities, the production rate at LEP2 in the single-resolved channel should reflect the behaviour seen at HERA and the double-resolved channel that was observed at Tevatron. Experimentally, the resolved and direct processes have a very different topology and they can be easily distinguished. For instance, single-resolved processes have an extra spectator jet occurring when a coloured parton of the photon interacts directly in the hard scattering rather than in the direct processes that involve only colour-singlet photons in the initial states. Usually this jet is in the same direction as the parent photon. Double-resolved processes, where both photons interact through their coloured partons in the hard scattering, will have two such jets.

Limits of integration for the hadronic cross sections

In the next three sections we discuss in detail the J/Ψ production in all kinds of processes at LO. Because in some cases the formulae are rather long we do not give their explicit analytical form, but show some plots to explain their behaviour and to make some remarks about the features that might be observed at an e^+e^- collider. For this purpose, we introduce in addition with the above notations the total hadronic center-of-mass energy S_H, and the transverse momenta and rapidity of the J/Ψ, with the notations p_T and y, respectively, and the same parameters for the associated particle X (if it is produced). With these notations, and using a 4-dimensional phase space formulation, we have

$$\begin{aligned} k_1 &= z_a \frac{\sqrt{S_H}}{2}(1,0,0,1), \\ k_2 &= z_b \frac{\sqrt{S_H}}{2}(1,0,0,-1), \\ P_{J/\Psi} &= (m_T \cosh y, p_T \cos\phi, p_T \sin\phi, m_T \sinh y), \\ k_3 &= (p_T^1 \cosh y_1, p_T^1 \cos\phi_1, p_T^1 \sin\phi_1, p_T^1 \sinh y_1). \end{aligned} \tag{3.24}$$

Using energy-momentum conservation we furthermore get

$$\begin{aligned} p_T \cos\phi &= p_T^1 \cos\phi_1, \\ p_T \sin\phi &= p_T^1 \sin\phi_1, \\ z_a \frac{\sqrt{S_H}}{2} + z_b \frac{\sqrt{S_H}}{2} &= m_T \cosh y + p_T^1 \cosh y_1, \end{aligned}$$

$$z_a \frac{\sqrt{S_H}}{2} - z_b \frac{\sqrt{S_H}}{2} = m_T \sinh y + p_T^1 \sinh y_1. \tag{3.25}$$

The Mandelstam variables can be expressed in terms of the new parameters as

$$\begin{aligned} s &= z_a z_b S_H, \\ t_1 &= -z_a \sqrt{S_H} m_T e^{-y}, \\ u_1 &= -z_b \sqrt{S_H} m_T e^{-y}. \end{aligned} \tag{3.26}$$

The one-particle phase space, expressed with the help of these parameters, becomes

$$\begin{aligned} \frac{d^3 P_{J/\Psi}}{2P^0_{J/\Psi}} &= \frac{p_T}{2} d\, p_T d\, y d\, \phi \ \text{ for a massive particle, and} \\ \frac{d^3 k_3}{2k_3^0} &= \frac{p_T^1}{2} d\, p_T^1 d\, y_1 d\, \phi_1 \ \text{ for a massless particle.} \end{aligned} \tag{3.27}$$

Using the above relations and Eq. (3.23) together with Eq. (3.21), we obtain the differential hadronic cross section as follows:

$$\begin{aligned} d\,\sigma(e^+e^- \to e^+e^- H + X) = \int_{z_a}^1 d\, x_a \frac{z_a}{x_a} f_{\gamma/e}(z_a/x_a) f_{a/\gamma}(x_a, M) \\ \int_{z_b}^1 d\, x_b \frac{z_b}{x_b} f_{\gamma/e}(z_b/x_b) f_{b/\gamma}(x_b, M) \sum_n \frac{d\,\hat{\sigma}}{d\, t_1} d\, p_T^2 d\, y d\, y_1 \frac{\langle \mathcal{O}^H[n] \rangle}{N_{col} N_{pol}}. \end{aligned} \tag{3.28}$$

For a given value of $\sqrt{S}_H$, the accessible phase space is defined by

$$\begin{aligned} & 0 \le p_T \le \frac{S - 4m_c^2}{2\sqrt{S_H}}, \\ & |y| \le \ \text{Arccosh} \frac{S + 4m_c^2}{2\sqrt{S} m_T}, \\ & -\ln \frac{\sqrt{S} - m_T \exp(-y)}{p_T^1} \le y_1 \le \ln \frac{\sqrt{S} - m_T \exp(y)}{p_T^1}, \end{aligned} \tag{3.29}$$

with

$$z_a = \frac{m_T \exp y + p_T^1 \exp y_1}{\sqrt{S}_H} \quad , \quad z_b = \frac{m_T \exp -y + p_T^1 \exp -y_1}{\sqrt{S}_H}. \tag{3.30}$$

All numerical analyses shown in this Chapter have been done using the same input parameters. In particular, we have used $m_c = 1.5$ GeV, $\alpha = 1/137.036$, and evaluate α_s at LO taking $n_f = 3$ active quark flavours, with the renormalization and factorization scale $\mu = \xi_\mu m_T$ and $M = \xi_M m_T$, respectively, with the default values $\xi_\mu = \xi_M = 1$. As for the photon PDFs, we use the LO set from Glück-Reya-Schienbein [36], which is the only

available one implemented in the fixed-flavour-number scheme, with $n_f = 3$.
For the default operator matrix elements (OMEs) $\langle \mathcal{O}^H \rangle$ we have adopted the set determined in Ref. [13] by fitting the Tevatron data Ref. [6] using the LO proton PDFs from Martin-Roberts-Stirling-Throne (MRST98LO). We have employed $\Lambda^{(3)}_{QCD} = 204$ MeV, which corresponds to $\Lambda^{(4)}_{QCD} = 174$ MeV, in order to conform with the fit [13]. Incidentally, the GRS photon PDFs are also implemented with $\Lambda^{(3)}_{QCD} = 204$ MeV [36]. The results for $\langle \mathcal{O}^{J/\Psi}[^1S_0^{[8]}] \rangle$ and $\langle \mathcal{O}^{J/\Psi}[^3P_J^{[8]}] \rangle$ are strongly correlated, and it is known only the linear combination

$$M_r^{J/\psi} = \langle \mathcal{O}^{\psi}[^1S_0^{[8]}] \rangle + \frac{r}{m_c^2} \langle \mathcal{O}^{\psi}[^3P_0^{[8]}] \rangle. \tag{3.31}$$

As default, we choose a democratic split $\langle \mathcal{O}^{\psi}[^1S_0^{[8]}] \rangle = \frac{r}{m_c^2} \langle \mathcal{O}^{\psi}[^3P_0^{[8]}] \rangle = M_r^{J/\psi}/2$ and the heavy quark spin symmetry relations :

$$\langle \mathcal{O}^{\psi}[^3P_J^{[8]}] \rangle = (2\ J + 1) \langle \mathcal{O}^{\psi}[^3P_0^{[8]}] \rangle. \tag{3.32}$$

3.2 Direct processes

We consider further LO J/Ψ production at e^+e- collisions, namely processes like
$e^+e^- \to e^+e^- J/\Psi + X$. If the associated jet or photon described by X is absent we have the $2 \to 1$ process and the J/Ψ transverse momentum vanishes. If X denotes at LO only one parton, then we define the $2 \to 2$ process, etc.

Let us start with the analysis of the direct channel. As we have already discussed, in such a process both photons behave as point-like particles. Fig. 3.2 describes the J/Ψ production in such processes, at the hadronic level. For the partonic level we should look at the corresponding Feynman diagrams.

- For $2 \to 1$ processes like $\gamma\gamma \to c\bar{c}[n]$, the subsequent Feynman diagrams are shown in Fig. 3.2. At this processes, the $c\bar{c}$ pair can be produced only in $^1S_0^{[1]}$ or $^3P_J^{[1]}$ with $J = 0, 2$ (Furry's theorem). In processes like
  $\gamma\gamma \to \chi_{c0}(^3P_0^{[1]})$ or $\gamma\gamma \to \chi_{c2}(^3P_2^{[1]})$ [37, 38, 39] ,
  higher charmonium states are produced, that can radiate a soft photon and reach a lighter state, for instance J/Ψ, with the branching fractions
  $Br(\chi_{c0} \to J/\Psi + \gamma) = (0.66 \pm 0.18)\%$, and $Br(\chi_{c2} \to J/\Psi + \gamma) = (13.5 \pm 1.1)\%$.
  NRQCD predicts for the P-wave OMEs a suppression of order v^2. We can conclude that there is no direct J/Ψ production in $2 \to 1$ processes. The probability for indirect production is not zero, but is rather small. These processes are interesting from

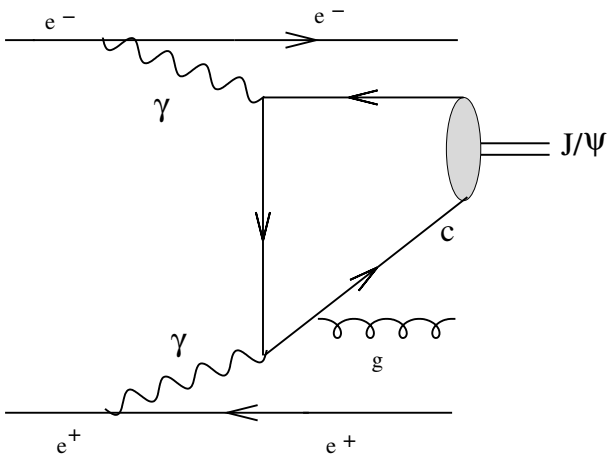

Figure 3.1: Diagrammatic representation of J/Ψ production in e^+e^- collisions, when only the direct process is considered.

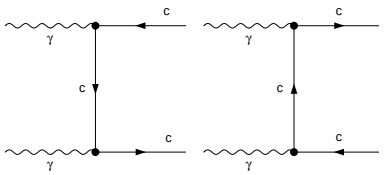

Figure 3.2: Feynman diagrams for $\gamma\gamma \to c\bar{c}$.

a theoretical point of view, because they provide the tool for the renormalization of the OMEs involved at NLO.

- In $2 \to 2$ processes like $\gamma\gamma \to c\bar{c} + X$, where $X = g, \gamma$ the possible $c\bar{c}$ final states are
  $\gamma\gamma \to c\bar{c}[^3S_1^{[1]}] + \gamma$,
  $\gamma\gamma \to c\bar{c}[^1P_1^{[1]}] + \gamma$ [40, 41, 33, 42], and
  $\gamma\gamma \to c\bar{c}[^3S_1^{[8]}] + g$,
  $\gamma\gamma \to c\bar{c}[^1P_1^{[8]}] + g$ [40, 41, 33, 42].
  Their corresponding Feynman graphs are shown in Fig. 3.3.

We give below the partonic cross sections for the $^3S_1$ states, computed in $n = 4 - 2\epsilon$ dimensions, since they are used further when a subsequent NLO analysis is presented.

We find

$$\frac{d\sigma}{dt}\left(\gamma\gamma \to c\bar{c}[^3S_1^{[8]}]g\right) = \frac{1}{2s}\,\frac{1}{8\pi s}\,\frac{1}{4(1-\epsilon)^2}\,\frac{1}{\Gamma(1-\epsilon)}\left(\frac{4\pi\mu^2 s}{tu}\right)^{\epsilon}(4\pi)^3\alpha_s Q_c^4\alpha^2 M$$

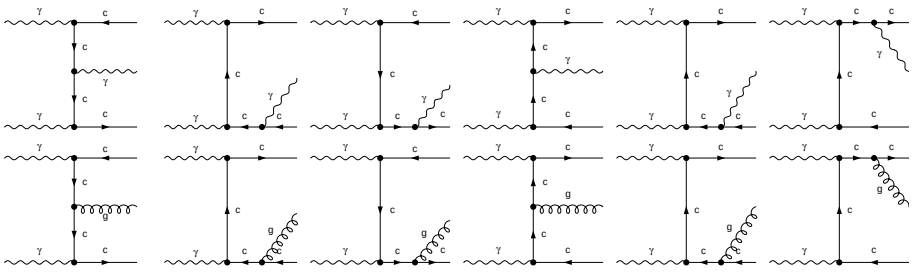

Figure 3.3: Feynman graphs for $\gamma\gamma \to c\bar{c}\gamma(g)$.

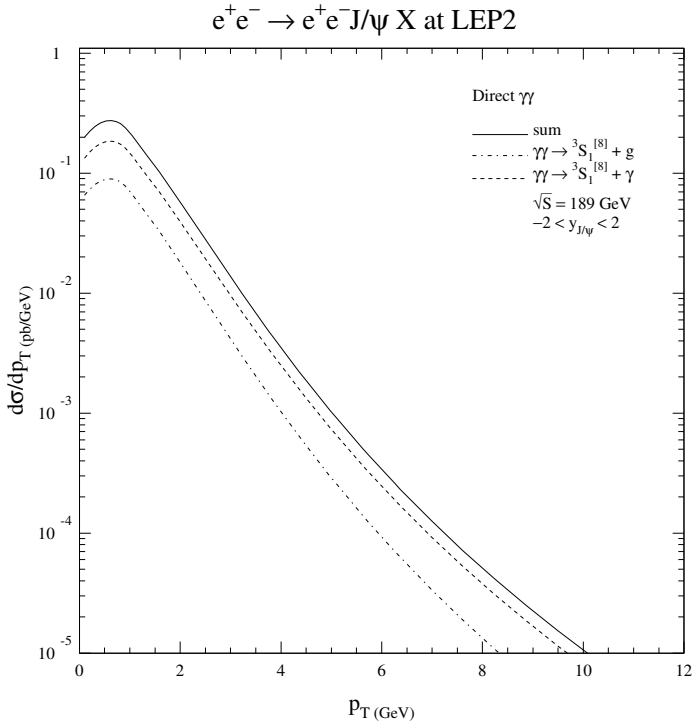

Figure 3.4: Transverse-momentum distribution $d\,\sigma/d\,p_T$, integrated over rapidity interval $|y| \leq 2$, of the $\gamma\gamma \to J/\Psi + X$, via bremsstrahlung at LEP2. The contribution corresponding to the two possible final states are also shown separately.

$$\frac{512 N_c C_F}{3-2\epsilon} \frac{\langle \mathcal{O}_8^{J/\psi}[^3S_1]\rangle}{N_{col}^{[8]}} \frac{(2-5\epsilon)stu(s+t+u) + 2(1-\epsilon)^2(s^2t^2+s^2u^2+t^2u^2)}{(s+t)^2(s+u)^2(t+u)^2}, \quad (3.33)$$

where $Q_c = 2/3$ and $M/2 = m_c$ are the fractional electric charge and the mass of the charm quark, respectively, s, t, and u are the Mandelstam variables. The prefactor $1/(4(1-\epsilon)^2)$ stems from the average over the photon polarization, $N_c = 3$, $C_F = (N_c^2-1)/(2N_c)$, and

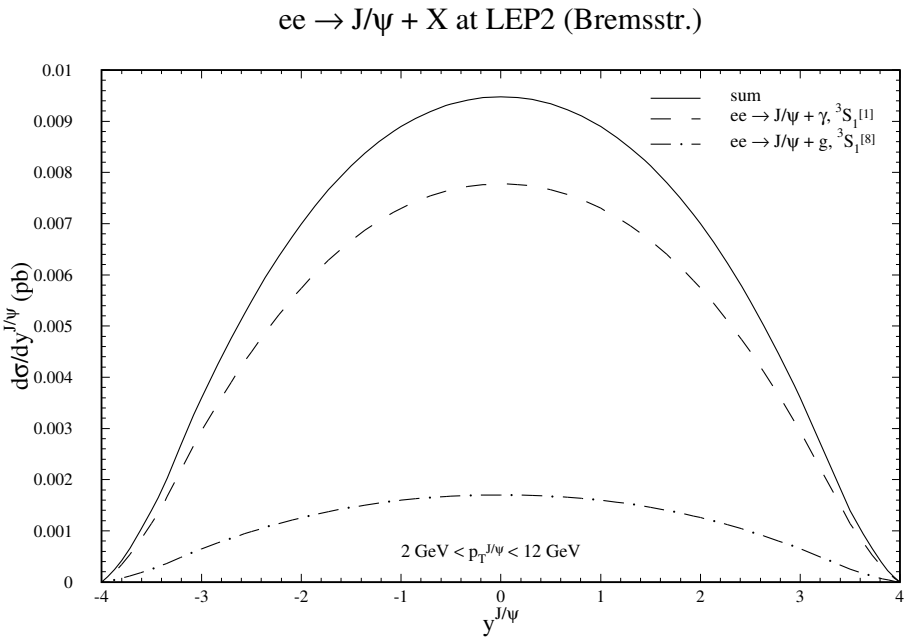

Figure 3.5: Rapidity distribution $d\sigma/dy$, integrated over the transverse-momentum interval $2\langle p_T \langle 12$ GeV, of $\gamma\gamma \to J/\psi + X$, where X represents a gluon jet or a prompt photon, via bremsstrahlung at LEP2. The contributions corresponding to these two final states are also shown separately.

$N_{col}^{[8]} = N_c^2 - 1$.
The expression for $d\sigma/dt\left(\gamma\gamma \to c\bar{c}\left[^3S_1^{[1]}\right]\gamma\right)$ emerges from Eq. (3.33) through the substitution

$$C_F\alpha_s\frac{\langle\mathcal{O}_8^{J/\Psi}\left[^3S_1\right]\rangle}{N_{col}^{[8]}} \to Q_c^2\alpha\frac{\langle\mathcal{O}_1^{J/\Psi}\left[^3S_1\right]\rangle}{N_{col}^{[1]}}. \tag{3.34}$$

The process with a photon in the final state is suppressed by the electromagnetic coupling α. A $c\bar{c}$ pair in $^3S_1^{[8]}$ state can hadronize into a J/Ψ through two successive electric (E_1) transitions that translate into a suppression of order v^4. Since the NRQCD velocity scaling rules are only qualitative, we need the values of the operators extracted from the experimental data to get the final prediction for each of the processes. As can be seen from Fig. 3.4, where the J/Ψ transverse momentum distribution in direct two-photon collisions is shown, the production rate from a $^3S_1^{[1]}$ state is almost an order of magnitude larger than that from a $^3S_1^{[8]}$ state, and this is due to the very small ratio $\langle\mathcal{O}_8[^3S_1]\rangle/\langle\mathcal{O}_1[^3S_1]\rangle \simeq 10^{-3}$ that obviously cannot be compensated by α_s/α. We conclude

that in direct two photon collisions the production of J/Ψ and a prompt γ is the dominant process.

In Fig. 3.5 we present the distribution in rapidity of the J/Ψ meson for $\gamma\gamma \to J/\Psi + X$, where X represents a gluon jet (dot-dashed lines) or a prompt photon (dashed lines). The solid lines refer to the sum of the contributions. Since we assumed the same experimental set-up for the electron and positron beams, the rapidity distribution displayed are all symmetric about $y = 0$. Non-vanishing cross sections also have processes like $\gamma\gamma \to c\bar{c}[^1P_1^{[1]}] + \gamma$ or like $\gamma\gamma \to c\bar{c}[^1P_1^{[8]}] + g$, but the values for the OMEs are very small and they have not yet been observed experimentally. But they present IR-divergences, and in this limit they factorize with the cross section of the process $\gamma\gamma \to c\bar{c}[^1S_0^{[1]}]$ and the corresponding $1/\epsilon_{IR}$ pole. In the infrared limit, they are just $2 \to 1$ processes with a radiated soft gluon or photon. The infrared pole will be absorbed into the renormalization of the $^1S_0^{[8]}$ operator ME. The exact cancellation of the divergences can be simply deduced from relations given in App. B.

3.3 Single-resolved processes

We consider now the processes where a photon behaves as a point-like particle and the other one enters into interactions through its gluon and quark constituents. Fig. 3.6 shows the single-resolved J/Ψ production at the hadronic level, and as can be seen an additional spectator jet is produced. If this additional parton to the $c\bar{c}$ pair is absent, we get the $2 \to 1$ processes, otherwise we recover the $2 \to 2$ processes.

- At the partonic level, in the $2 \to 1$ processes like $\gamma g \to c\bar{c}[8]$, the $c\bar{c}$ pair can be produced in the following states
  $\gamma g \to c\bar{c}[^1S_0^{[8]}]$,
  $\gamma g \to c\bar{c}[^3P_0^{[8]}]$,
  $\gamma g \to c\bar{c}[^3P_2^{[8]}]$ [37, 38, 39].
  Their corresponding Feynman diagrams are similar to those shown in Fig. 3.2, with one of the initial photons replaced with a gluon.

In these processes, only colour-octet states can be produced. They are obviously only intermediate states and they radiate soft gluons in the hadronization process. These higher Fock states will reach a J/Ψ hadronic state via a magnetic (M_1) transition in the case of $^1S_0^{[8]}$,or via an electric (E_1) transition in the case of $^3P_J^{[8]}$. To make a correct estimate of the size of the production rates, we should take into account the velocity-scaling rules predicted by the NRQCD for the operators. If we account for all phenomena

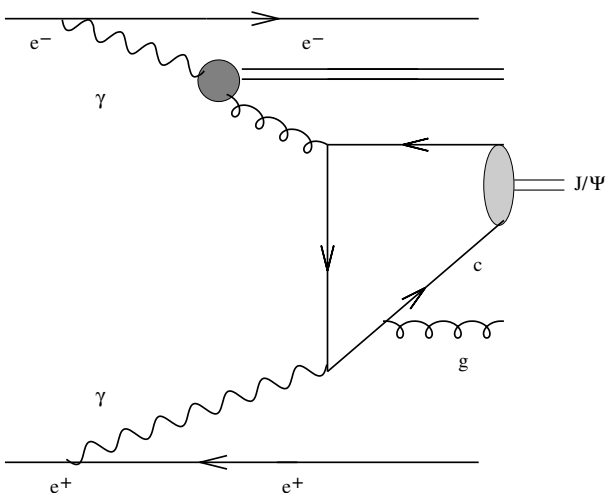

Figure 3.6: Diagrammatic representation of the J/Ψ production at the hadronic level, in e^+e^- collisions, when only the single-resolved partonic process is considered.

involved, the probability that a colour-octet $^1S_0$ state hadronizes into a J/Ψ-state scales with the same power of v, namely v^4, as those for the colour-octet ^3P_j states.

- In the $2 \to 2$ processes like $\gamma\gamma \to c\bar{c}[n] + X$, the $c\bar{c}$ pair can be produced both in colour-singlet and colour-octet states as
  $\gamma g \to c\bar{c}[^3S_1^{[1]}] + g$ [2] ,
  $\gamma g \to c\bar{c}[^1P_1^{[1,8]}] + g$,
  $\gamma g \to c\bar{c}[^3S_1^{[8]}] + \gamma$ [43, 44],
  $\gamma g \to c\bar{c}[^1P_1^{[8]}] + \gamma$,
  $\gamma g \to c\bar{c}[8] + g$ and
  $\gamma q \to c\bar{c}[8] + q$, where $[8] = {}^3S_1^{[8]}$, ${}^1S_0^{[8]}$, ${}^3P_J^{[8]}$, with $J = 0, 1, 2$ [11, 37, 38].

The Feynman diagrams corresponding to processes like $\gamma g \to c\bar{c}[n] + g$ are shown in Fig. 3.7, together with the diagrams involving the subsequent Fadeev-Popov ghosts. The Feynman diagrams for processes like $\gamma g \to c\bar{c}[n] + \gamma$ are very similar to those shown in Fig. 3.3, with the obvious replacement of an initial photon with a gluon. Fig. 3.8 shows the Feynman diagrams for the case of a quark as a constituent of the photon. Except for the cross sections of the processes $\gamma g \to c\bar{c}[^3S_1^{[1,8]}] + g$, which can be obtained from Eq. (3.33) by multiplying with the following conversion factors:

$$\frac{1}{N_c^2}\,K_c^g \quad \text{for} \quad {}^3S_1^{[1]} \quad \text{state} \;, \quad B_F\,K_c^g \quad \text{for} \quad {}^3S_1^{[8]} \quad \text{state}, \tag{3.35}$$

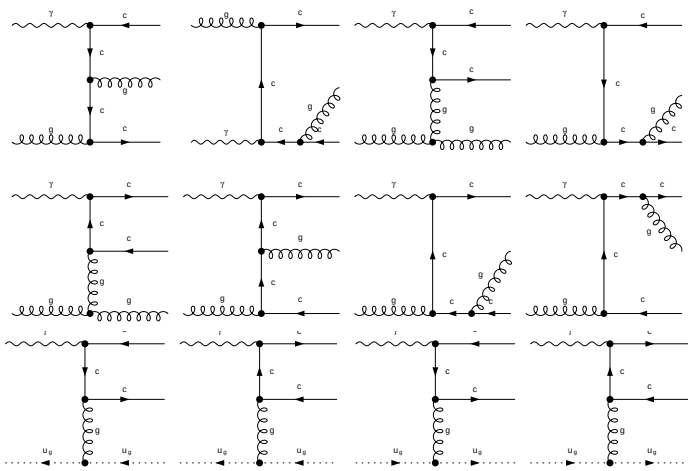

Figure 3.7: Feynman diagrams for the process $\gamma g \to c\bar{c}[n] + g$.

the subsequent formulae for the other processes are rather long and we do not give their explicit expressions. We have analytically calculated the cross sections of all these LO process and compared our results with the literature. We show transverse-momentum distributions for some of them, in order to get their main behaviour.

In processes like $\gamma g \to c\bar{c} + g$, both colour-singlet and colour-octet states can be produced. It is important to note that, for the single-resolved processes, only those producing ${}^3S_1^{[1,8]}$ states remain finite in the limit of vanishing transverse momentum $p_T \to 0$. The $2 \to 2$ processes producing ${}^1S_0^{[8]}$, ${}^3P_J^{[8]}$ suffer from infrared- and collinear-divergences. In fact, these $2 \to 2$ processes at $p_T \to 0$ are just $2 \to 1$ processes with a soft-collinear emission. Processes like $\gamma g \to {}^3P_J^{[8]} + g$ or $\gamma g \to {}^1S_0^{[8]} + g$ involve the splitting of the initial gluon into two gluons. In the soft-collinear limit, their cross sections factorize into the gluon splitting function and the cross section of the subsequent $2 \to 1$ process. In a full NLO analysis, these singularities would be factorized at a scale M and absorbed into the bare PDFs so as to renormalize the latter.

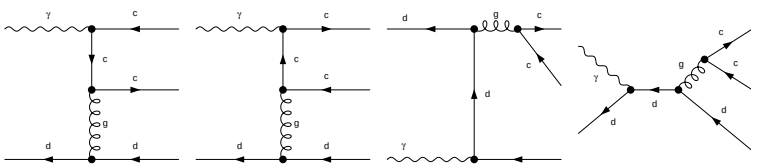

Figure 3.8: Feynman diagrams for the process $\gamma q \to c\bar{c}[n] + q$.

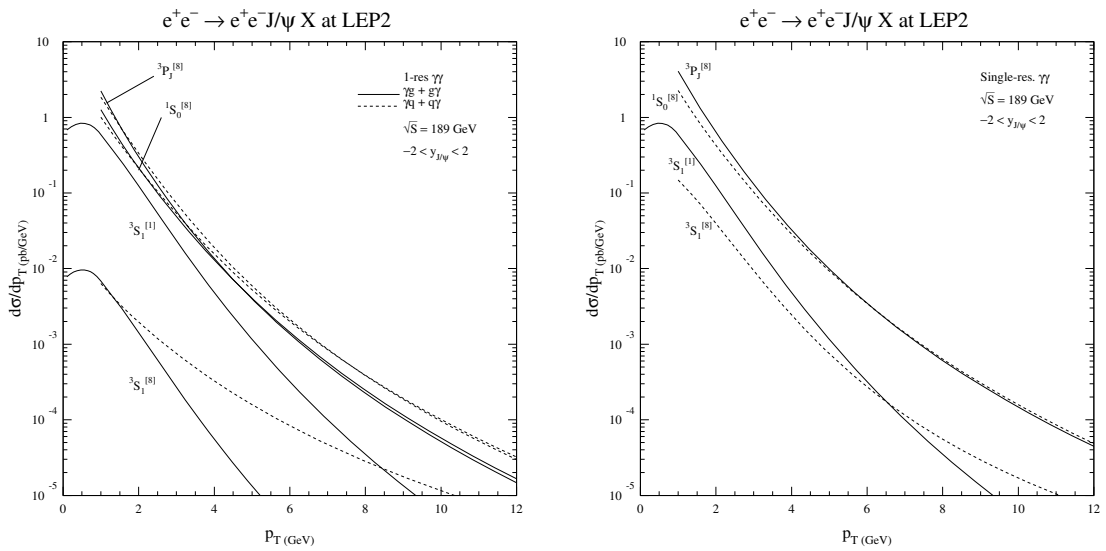

Figure 3.9: Transverse-momentum distribution $d\ \sigma/d\ p_T$, integrated over the rapidity interval $|y| \leq 2.$, of $\gamma g \to c\bar{c}[n] + g$ and $\gamma q \to c\bar{c}[n] + q$, via bremsstrahlung at LEP2. The contributions due to various channels are shown separately. Also the contributions due to different partons are shown separately on the left-hand side and their sum on the right-hand side.

If the photon participates at the hard scattering through its light quarks $q = d$, u, s, then only colour-octet ${}^1S_0$, ${}^3P_J$ states can be produced. All $2 \to 2$ processes are in this case infrared- and collinear-divergent. Here there are no corresponding $2 \to 1$ LO processes. However the J/Ψ is produced by the fragmentation of a gluon. The soft-collinear divergences must therefore be absorbed into the fragmentation functions in this case.

Also processes like $\gamma g \to c\bar{c}[{}^1P_1^{[8]}] + g$ are affected by infrared-singularities and these will be absorbed into the renormalization of the ${}^1S_0^{[8]}$ matrix element. Namely, in the IR-limit the cross section for this process factorizes like:

$$d\,\sigma(\gamma g \to c\bar{c}[{}^1P_0^{[8]}] + g) \sim \frac{1}{\epsilon_{IR}}\, B_F \frac{4\,\alpha_S}{3\pi m_c^2} d\,\sigma(\gamma g \to c\bar{c}[{}^1S_0^{[8]}]) \tag{3.36}$$

which is exactly canceled by the order α_S NRQCD corrections for the $\langle \mathcal{O}_8[{}^1S_0] \rangle$ [see Eq. B.29]. There is also a finite remainder from this renormalization procedure, which is proportional to $\langle \mathcal{O}_8[{}^1P_1] \rangle$. The same set of arguments are true also for ${}^1P_1^{[1]}$ states, with the corresponding colour prefactor replacement $B_F \to C_F$. In Fig. 3.9 we present transverse-momentum spectra for the individual channels: ${}^3S_1^{[1,8]}$, ${}^1S_0^{[8]}$, ${}^3P_J^{[8]}$. In the left-

hand side figure, the solid lines correspond to the gluon contributions and the dotted lines to the quark contributions. In the right-hand side figure we show the sum of the gluon and quark contributions. The slopes of the p_T-distributions of the ${}^1S_0^{[8]}$ and ${}^3P_J^{[8]}$ channels are very similar. The slopes of CS and CO ${}^3S_1$ are very different from these. This behaviour is well known and has been used to extract the OMEs from CDF-Tevatron data. The contribution involving the linear combination

$$M_r^{J/\psi} = \langle \mathcal{O}^{\psi}[{}^1S_0^{[8]}] \rangle + \frac{r}{m_c^2} \langle \mathcal{O}^{\psi}[{}^3P_0^{[8]}] \rangle$$

is separated from that of the ${}^3S_1$ terms.

The gluon as well as the quark contributions are very much dependent on the chosen parametrization for the parton densities. In the above figures, we have used our default settings, namely GRS-parametrization for the photon PDFs. As a general remark, the gluon contribution decreases more rapid by with increasing p_T due to the gluon PDF behaviour.

We also have not included in Fig. 3.9 the contribution due to prompt photon production. It was shown for the direct case where it is dominant. There are two reasons for this exclusion: one is that they are rather small and do not change the overall behaviour, the other one is that in the last Section, where a direct comparison with DELPHI-data is shown, they have to be excluded due to experimental settings.

3.4 Double-resolved processes

We have defined the double-resolved processes in the first Section of this Chapter. A representation of these types of interactions in e^+e^- collisions at the hadronic level is shown in Fig. 3.10. As before, we divide the analysis in two parts.

- At the partonic level, in the $2 \to 1$ processes, the $c\bar{c}$ pair can be produced as
  $gg \to c\bar{c}[{}^1S_0^{[1,8]}]$,
  $gg \to c\bar{c}[{}^3P_J^{[1,8]}]$ with $J = 0, 1, 2$ [see Ref. [15, 5]],
  $q\bar{q} \to c\bar{c}[{}^3S_1^{[8]}]$ [see Ref. [15, 5]].

The corresponding Feynman graphs are shown in Figs 3.11 and 3.12. For processes like $gg \to c\bar{c}$ we should include also Fadeev-Popov ghosts, and the partonic cross sections are then obtained by subtracting the ghost contributions from the gluon contributions.

- In double-resolved $2 \to 2$ processes all possible $c\bar{c}$ final states can be produced:
  $gg \to c\bar{c}[{}^3S_1^{[1]}] + g$ [see Ref. [3]],

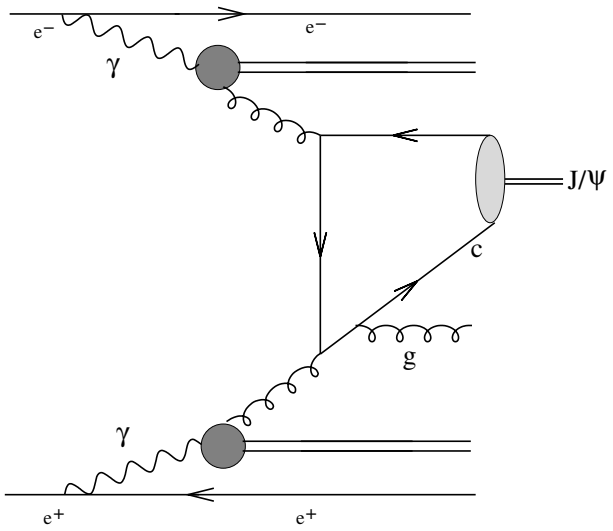

Figure 3.10: Diagrammatic representation of the J/Ψ production at the hadronic level, ine^+e^- collisions, where the double-resolved partonic process is involved.

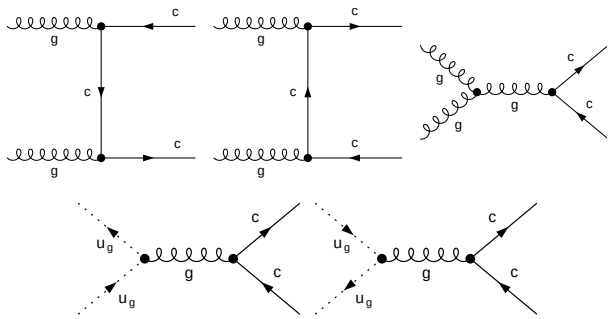

Figure 3.11: Feynman graphs corresponding to partonic processes like $gg \to c\bar{c}[n]$.

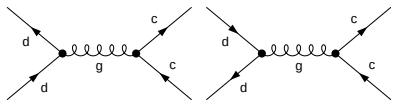

Figure 3.12: Feynman graphs corresponding to partonic processes like $q\bar{q} \to c\bar{c}[n]$.

$gg \to c\bar{c}[^3P_J^{[1]}] + g$ [see Ref. [24]],
$gg \to c\bar{c}[8] + g$ where $[8] = {}^3S_1^{[8]}$, ${}^1S_0^{[8]}$, ${}^3P_J^{[8]}$ [see Ref. [11, 5]],
$gg \to c\bar{c}[^3S_1^{[1]}] + \gamma$, $gg \to c\bar{c}[^3P_J^{[1]}] + \gamma$ [see Ref. [44]],
$gg \to c\bar{c}[8] + \gamma$ [see Ref. [43]],

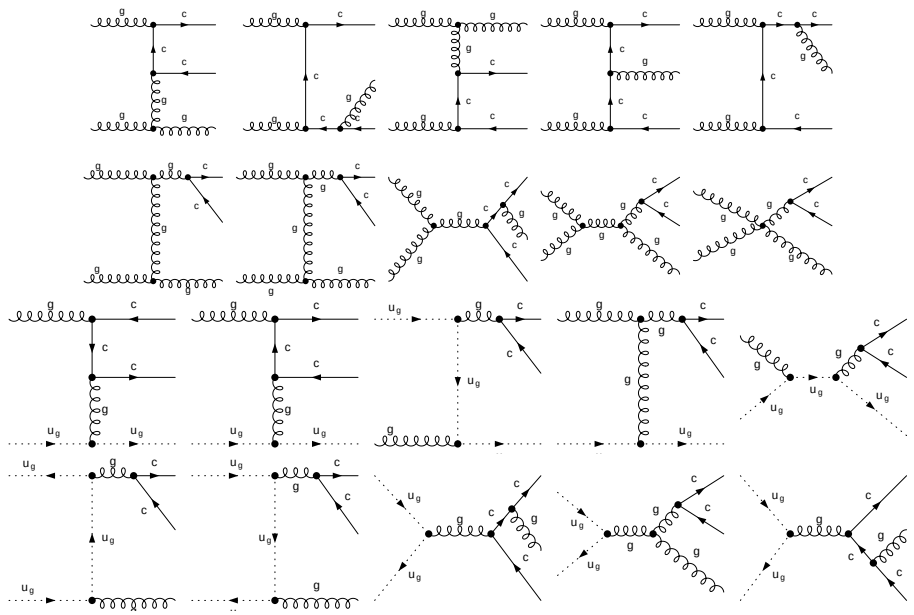

Figure 3.13: Feynman graphs for the partonic process $gg \to c\bar{c} + g$.

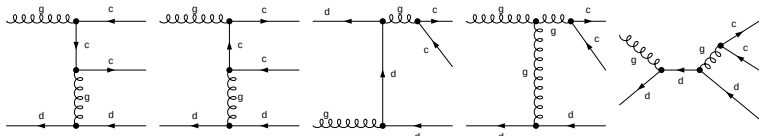

Figure 3.14: Feynman graphs for the partonic process $gq \to c\bar{c} + q$.

$gq \to c\bar{c}[^3P_J^{[1]}] + q$ [see Ref. [3]],
$gq \to c\bar{c}[8] + q$ [see Ref. [11, 5]],
$q\bar{q} \to c\bar{c}[^3P_J^{[1]}] + g$ [see Ref. [3]],
$q\bar{q} \to c\bar{c}[8] + g$ [see Ref. [11, 5]].

The corresponding Feynman graphs are shown in Figs 3.13, 3.14 and 3.15. For the process $gg \to c\bar{c} + g$, we have not shown the graphs that differ from those already exhibited only by the fermionic flow on the charm quark (anti-quark) lines or ghost (anti-ghost) lines.

For the processes like $gq \to c\bar{c}q$, we do not show the diagrams obtained by reversing the fermionic flow for the light quark lines, which would describe the equivalent process with an anti-quark initiating parton. For the same reasons that we have mentioned in the last Section, we do not present specific contributions for processes where a prompt photon is produced. As in the case of single-resolved processes, to get the full double-resolved contribution, we should sum over the subsequent contributions generated in all

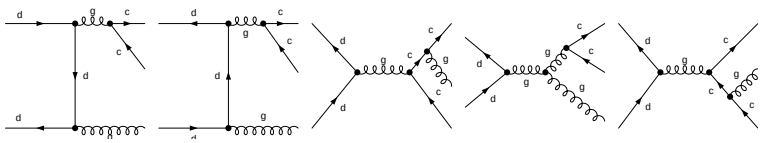

Figure 3.15: Feynman graphs for the partonic process $q\bar{q} \to c\bar{c} + g$.

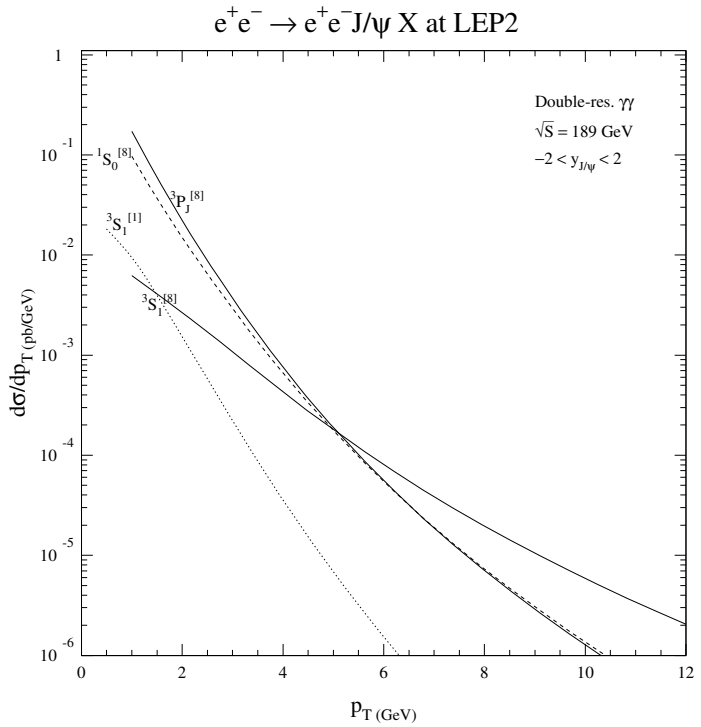

Figure 3.16: Transverse-momentum distribution $d\sigma/dp_T$, integrated over the rapidity interval $|y| \leq 2$, of the double-resolved contribution, via bremsstrahlung at LEP2. The individual contributions due to various channels are shown separately.

possible interactions between partonic constituents of each of the two photons, namely gg, gq, qg, $q\bar{q}$. Also for processes like $gg \to c\bar{c} + g$, the Fadeev-Popov ghost contributions should be subtracted from the pure gluon-gluon contributions.

The subprocess cross sections for double-resolved processes are the same as those for $p\bar{p}$ collisions, since the parton content of both photons is resolved in this case. With the exception of the S-wave production, the corresponding cross sections have large analytical formulae and we shall not present them explicitly. We show in Fig. 3.16 the transverse-momentum distributions for the individual channels. This provides us with information

about their hierarchy and their behaviours in different kinematical regions. As in the single-resolved case, the cross sections corresponding to the production of the ${}^3S_1^{[8]}$, ${}^1S_0^{[8]}$, ${}^3P_J^{[8]}$ states exhibit infrared-collinear divergences. As we have already discussed, some of these singularities would be absorbed into the photon PDFs renormalization, and the remaining ones into the NRQCD operator renormalization. The subsequent cross section for the production of the ${}^3S_1^{[1]}$ is again finite in the limit $p_T \to 0$.

In the double-resolved processes, it turns out that the ${}^3S_1^{[8]}$ term is dominant at large transverse momentum as can be seen from Fig. 3.16. The ${}^1S_0^{[8]}$ and the ${}^3P_J^{[8]}$ terms dominate at low p_T. We should notice that the CO contribution is much larger than the CS term, as it was also in the single-resolved case. Hence, even if the CO matrix elements were overestimated in the extraction from Tevatron data, the CO contribution is still substantial. In the next Section we shall see that the CO contribution is indispensable in explaining the experimental data recorded at LEP2 with the DELPHI detector.

We should also notice that the NRQCD factorization in the small p_T region might be affected by large higher twist corrections. At low p_T, higher twist effects are induced by the interaction of the heavy-quark and anti-quark pair with the forward jets [27]. The effects of these phenomena as well as the diffractive processes are beyond the scope of this work.

3.5 Comparison with DELPHI data

Very recently, the DELPHI Collaboration has presented preliminary data on the inclusive cross section of J/ψ photoproduction in $\gamma\gamma$ collisions ($e^+e^- \to e^+e^- J/\psi + X$) at CERN LEP2, taken as a function of the J/ψ transverse momentum (p_T) [8]. The J/ψ mesons were identified through their decays to $\mu^+\mu^-$ pairs, and events where the system X contains a prompt photon were suppressed by requiring that at least four charged tracks were reconstructed. The luminosity-weighted average e^+e^- center-of-mass (c.m.) energy was $\sqrt{s} = 197$ GeV, the scattered positrons and electrons were anti-tagged, with maximum angle $\theta_{\max} = 32$ mrad, and the $\gamma\gamma$ c.m. energy was constrained to be $W \leq 35$ GeV in order to reject the major part of the non-two-photon events. The total cross section was found to be $\sigma(e^+e^- \to e^+e^- J/\psi + X) = (45.3 \pm 18.8)$ pb.

In this Section, we confront this data with up-to-date theoretical predictions based on NRQCD and the CSM, in order to find out if it is able to discriminate between the two. In want of the full next-to-leading-order (NLO) corrections, it is indispensable to perform a comprehensive and conservative analysis of the theoretical uncertainties. Doing this, we shall find that this data clearly favours the NRQCD prediction, while the CSM one

significantly falls short of it.

In $\gamma\gamma$ collisions, J/ψ mesons can be produced directly, or via radiative or hadronic decays of heavier charmonia, such as χ_{cJ} and ψ' mesons, or via weak decays of b hadrons. The respective decay branching fractions are $B(\chi_{c0} \to J/\psi+\gamma) = (0.66\pm0.18)\%$, $B(\chi_{c1} \to J/\psi+\gamma) = (27.3\pm1.6)\%$, $B(\chi_{c2} \to J/\psi+\gamma) = (13.5\pm1.1)\%$, $B(\psi' \to J/\psi+X) = (55\pm5)\%$, and $B(B \to J/\psi+X) = (1.16\pm0.10)\%$ [45]. The OPAL Collaboration has recently measured the total cross section of open-bottom production in $\gamma\gamma$ collisions at LEP2, under similar kinematic conditions as DELPHI [8] ($\sqrt{s} = 194$ GeV, $\theta_{\max} = 33$ mrad, and $10 \le W \le 60$ GeV), to be $\sigma(e^+e^- \to e^+e^-b\overline{b}+X) = (14.2\pm5.9)$ pb [46]. The cross section for J/ψ mesons from b-hadron decays may thus be estimated to be (0.33 ± 0.14) pb, which is less than 1% of the total J/ψ cross section measured by DELPHI and can be safely neglected. The cross sections of the four residual indirect production channels may be approximated by multiplying the direct-production cross sections of the respective intermediate charmonia with their decay branching fractions to J/ψ mesons.
We have discussed in the previous Sections about all contributing partonic subprocesses. A data-theory comparison accounts for all three types of processes: direct, single- and double-resolved. As can be seen from Figs 3.4, 3.9 and 3.16, the single-resolved channel is dominant. Taking the total cross section as a reference quantity, the direct, single-resolved, and double-resolved channels account for 1%, 98%, and 1% of the NRQCD prediction respectively. The situation is very similar for the CSM, except that direct photoproduction is forbidden at LO.

In our numerical analysis, we use as default input parameters the same settings as those discussed in the Section 3.1. In order to get an estimate of the theoretical uncertainties, we vary the scale parameters ξ_μ and ξ_M between 1/2 and 2 about the default value 1. We describe the sensitivity to the operator MEs, taking for comparison their values determined by fitting Tevatron-data using LO proton PDFs from CTEQ Collaboration [48].

In the cases $\psi = J/\psi, \psi'$, the fit results for $\langle\mathcal{O}^\psi[^1S_0^{[8]}]\rangle$ and $\langle\mathcal{O}^\psi[^3P_0^{[8]}]\rangle$ are strongly correlated, and one is only sensitive to the linear combination $M_r^{J\psi}$ Eq. (3.31) with an appropriate value of r . Since the cross sections are sensitive to a different linear combination of $\langle\mathcal{O}^\psi[^1S_0^{[8]}]\rangle$ and $\langle\mathcal{O}^\psi[^3P_0^{[8]}]\rangle$ which is shown in Eq. (3.31), we write $\langle\mathcal{O}^\psi[^1S_0^{[8]}]\rangle = \kappa M_r^{J\psi}$ and $\langle\mathcal{O}^\psi[^3P_0^{[8]}]\rangle = (1-\kappa)\,(m_c^2/r)\,M_r^{J\psi}$ and vary κ between 0 and 1 about the default value 1/2.
In order to estimate the theoretical uncertainties in our predictions, we vary the unphysical parameters ξ_μ, ξ_M, and κ as indicated above, take into account the experimental errors on m_c, the decay branching fractions, and the default MEs, and switch from our

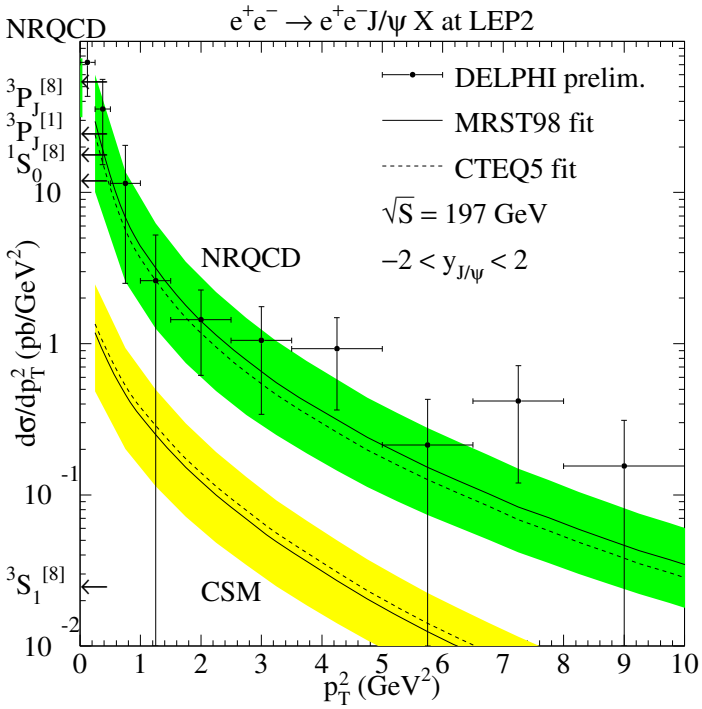

Figure 3.17: The cross section $d\sigma/dp_T^2$ of $e^+e^- \to e^+e^- J/\psi + X$ measured by DELPHI [8] as a function of p_T^2 is compared with the theoretical predictions of NRQCD and the CSM. The solid and dashed lines represent the central predictions obtained with the ME sets referring to the MRST98LO [47] (default) and CTEQ5L [48] PDFs, respectively, while the shaded bands indicate the theoretical uncertainties on the default predictions. The arrows indicate the NRQCD prediction for $p_T = 0$ and its ${}^3P_J^{[1]}$, ${}^1S_0^{[8]}$, ${}^3S_1^{[8]}$, and ${}^3P_J^{[8]}$ components.

default ME set to the CTEQ5L one, properly adjusting $\Lambda^{(3)}_{\rm QCD}$. We then combine the individual shifts in quadrature, allowing for the upper and lower half-errors to be different. In Fig. 3.17, we confront the p_T^2 distribution of $e^+e^- \to e^+e^- J/\psi + X$ measured by DELPHI [8] with our NRQCD and CSM predictions. The solid lines and shaded bands represent the central results, evaluated with our default settings, and their uncertainties, respectively. We observe that the DELPHI data clearly favours the NRQCD prediction, while it significantly overshoots the CSM one.

This is even more apparent from the data-over-theory representations shown in Fig. 3.18. This qualitative observation can be substantiated by considering the χ^2 values for the $N = 9$ data points with $p_T^2 \geq 0.25$ GeV^2. In fact, the NRQCD central prediction yields $\chi^2/N = 0.49$, which is to be compared with 1.79 for the CSM one. The situ-

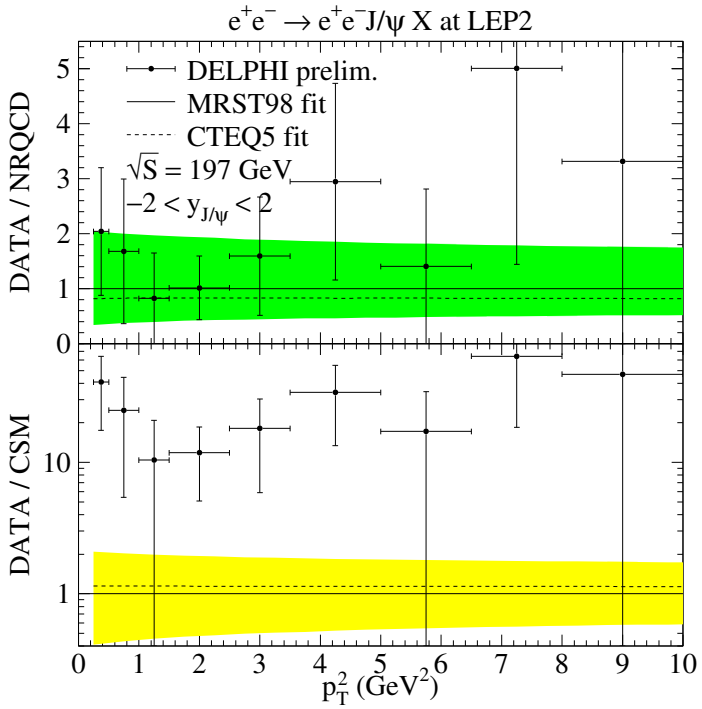

Figure 3.18: Data-over-theory representation of Fig. 3.17.

ation is very similar for the MEs pertinent to the CTEQ5L PDFs (dashed lines), the corresponding results being 0.62 and 1.76, respectively. As for the integral over the range $1 \leq p_T^2 \leq 10$ GeV^2, the DELPHI, NRQCD, and CSM results read (6.4±2.0) pb, $4.7^{+1.9}_{-1.2}$ pb, and $0.39^{+0.16}_{-0.09}$ pb, respectively, *i.e.*, the DELPHI measurement and the NRQCD prediction mutually agree within errors, while the CSM prediction falls significantly short of the DELPHI result, by a factor of 16 as far as the central values are concerned.

In NRQCD, 91% of the J/ψ mesons are directly produced, while 9% stem from the decays of χ_{cJ} and ψ' mesons. In the CSM, direct production happens less frequently, in 77% of all cases. As explained above, the contribution from b-hadron decays is negligible. Consequently, the ratio of direct and indirect lends itself as a useful discriminator between NRQCD and the CSM, and it would be desirable to measure it in $\gamma\gamma$ collisions.

In NRQCD, the most important error sources include the variations of ξ_μ, m_c, and κ, which, in average, make up 55%, 24%, and 11% of the total error squared, $(\delta_\uparrow\sigma)^2 + (\delta_\downarrow\sigma)^2$, respectively. In the CSM, the largest errors are related to ξ_μ (59%), m_c (30%), and ξ_M (7%).

It is generally believed that the magnitude of unknown higher-order corrections may be

estimated by scale variations of the known results. For the single-resolved channel, which greatly dominates our results, the NLO corrections in the CSM are known to be moderate at small values of p_T.

Chapter 4

Virtual corrections

In this Chapter we consider virtual corrections to the processes $\gamma\gamma \to c\bar{c}[n] + \gamma$ and $\gamma\gamma \to c\bar{c}[n] + g$. Virtual corrections of order $\alpha^3\alpha_s$ or $\alpha^2\alpha_s^2$ come from the interference of the Born amplitudes with the virtual diagrams. At this order of accuracy, these are one-loop diagrams. They contain IR-, UV- and Coulomb-singularities. The UV-divergences are removed by renormalization (redefinition of the fields and parameters of the bare Lagrangian) of the charm-quark mass, gluon field, quark fields and the strong-coupling constant. IR-singularities cancel in the sum of virtual and real corrections. This is guaranteed by the Bloch-Nordsieck and Kinoshita-Lee-Nauenberg (KLN) theorems [49, 28]. Real corrections also contain another type of singularities, called collinear or mass singularities, which will be dealt with by the mass factorization procedure. Basically this amounts to a redefinition of the parton densities of the incoming hadrons.

For the regularization of all these singularities we have used *dimensional-regularization* with $n = 4 - 2\epsilon$. As is well known, this regularization scheme preserves the gauge and Poincaré invariance but it breaks down the scale invariance. The simplest prescription for this scheme is

$$\int \frac{d^4q}{(2\pi)^4} \to \mu^{(4-n)} \int \frac{d^nq}{(2\pi)^n}, \tag{4.1}$$

thereby explicitly introducing the scale invariance breaking parameter μ, arbitrary chosen and with the dimension of $[Mass]$. As a direct consequence, all singularities arise as poles like $1/\epsilon$ or $1/\epsilon^2$. When a IR- and a collinear singularity occur at the same kinematical point, we get a double pole. Therefore we have to compute all diagrams up to order ϵ^2.

In our computation we will also encounter Coulomb-singularities. These arise when a longitudinal gluon is exchanged between the external heavy quark and and anti-quark legs. These can be regularized either with a small mass given to the gluon, or by introducing a small relative velocity between the heavy quark and anti-quark. Depending on the

regularization scheme, the Coulomb-singularities appear as $1/m_g$ or as $1/v$ terms in the final result. These are eliminated after considering radiative corrections to the OME within NRQCD, as we discussed in Chapter 2.

4.1 Renormalization scheme

The idea of *renormalization* is to calculate physical quantities with *bare* parameters that are divergent. These parameters are then renormalized, leading to a finite result for the physical quantities. This remarkable feature is called *renormalizability* and was first proven by 't Hooft [50, 51] for the non-Abelian gauge theories.

The bare parameters and fields are expressed in terms of the *renormalized* parameters and fields by means of the renormalization transformations

- gluon field renormalization : $A_\mu^0 = \sqrt{Z_3} A_\mu$,
- quark field renormalization: $\Psi_Q^0 = \sqrt{Z_2}\Psi_Q$,
- mass renormalization: $m_Q^0 = Z_m m_Q$,
- coupling renormalization : $g_s^0 = Z_g g_s$,

where the bare quantities are labeled by a superscript 0. The quantities $Z_i = 1 + \delta Z_i$, with $i = 2, 3, m, g$, are called *renormalization constants* and contain UV-divergences. The divergences are unique, but there is a freedom in choosing the finite part that is shifted into the renormalization constants. This choice defines the renormalization scheme.

We have used the *On-shell* [52, 53] prescription to fix the renormalized mass at the pole mass for the heavy quark flavour present in the computations. As compared to the $\overline{\rm MS}$ mass, the pole mass is independent of the scheme, the renormalization scale, and the gauge parameter. Thus it is a 'good' mass parameter to be used.

The Slavnov-Taylor identity for the renormalization constants is [54]

$$Z_g \sqrt{Z_3} = \frac{Z_1}{Z_3} = \frac{Z_{1h}}{Z_{3h}} = \frac{Z_{1f}}{Z_2} = \frac{Z_4}{Z_1}, \tag{4.2}$$

where Z_1, Z_{1h}, Z_{1f}, Z_4 are triple-gluon vertex, triple gluon-ghost vertex, quark-gluon vertex and four-gluon vertex renormalization constants [see *i.e.* Ref. [55]]. This identity is valid only if we have assumed the universality of the renormalized coupling g_s, and hence there is only one Z_g. A violation of this identity would amount to breaking the local gauge symmetry of the renormalized Lagrangian.

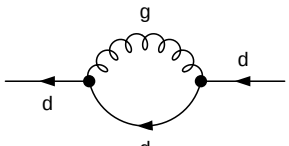

Figure 4.1: Generic Feynman diagram for the one-loop quark self-energy.

We wish to have $n_{lf} = 3$ light quark active flavours (u,d,s) in the running strong coupling constant α_s. We do not consider further heavy-quark loop contributions to virtual corrections, as well as the splitting of the final gluon into a heavy quark and anti-quark pair in real corrections. If we chose $n_{lf} = 4$ active flavours, we should also take into account charm-quark contributions in virtual and real corrections. However, after decoupling of m_c, they are suppressed by $(1/m_c)$ relative to light quark contributions [56]. Since in the development of NRQCD, $(1/m_c)$ is considered as a Taylor expansion parameter, and we have truncated the series at the first two terms, we neglect charm quark and anti-quark contributions in the NLO corrections.

4.1.1 Heavy-quark self-energy

The unnormalized quark self energy can be computed using the Feynman diagram shown in Fig. 4.1 as follows:

$$\begin{aligned}
-i\Sigma^q(k) &= -g_s^2\mu^{2\epsilon}(T^aT^a)_{ij}\int\frac{d^nq}{(2\pi)^n}\frac{1}{q^2}\gamma^\mu\frac{1}{(\not k+\not q-m)}\gamma_\mu \\
&= -g_s^2\mu^{2\epsilon}(T^aT^a)_{ij}\int\frac{d^nq}{(2\pi)^n}\frac{(2-n)(\not k+\not q)+nm}{q^2[(q+k)^2-m^2]} \\
&= \frac{i}{16\pi^2}(4\pi)^\epsilon g_s^2\left(\frac{\mu}{m}\right)^{2\epsilon}(T^aT^a)_{ij}\Gamma(\epsilon)\int_0^1 d\,x\frac{(2-n)(1-x)\;\not k+nm}{[\frac{k^2}{m^2}(x^2-x)+x]^\epsilon}. \quad (4.3)
\end{aligned}$$

The renormalized quark self-energy is obtained from the unrenormalized quark self-energy, by introducing the corresponding counterterm δZ_m for the quark mass renormalization and the counterterm δZ_2 for the renormalization of the quark wave function:

$$\begin{aligned}
\Sigma^q(\not k,m) &= \delta_{ij}[Am+B(\not k-m)], \\
\Sigma_c(\not k,m) &= -\delta_{ij}[(Z_2-1)\;\not k-(Z_2Z_m-1)m], \\
\Sigma_R^q(\not k,m) &= \Sigma^q(\not k,m)+\Sigma_c(\not k,m)=\delta_{ij}[(A+\delta Z_m)m+(B-\delta Z_2)(\not k-m)]. \quad (4.4)
\end{aligned}$$

The renormalized quark self-energy has to be UV-finite. In the *on-shell* renormalization scheme the renormalization conditions for the quark self-energy are

$$\Sigma_R^q(\not k=m)=0, \quad (4.5)$$

$$\frac{\partial}{\partial \not{k}}\Sigma_R^q(\not{k})|_{\not{k}=m} = 0. \tag{4.6}$$

From these conditions one gets further

$$\delta_{ij} m \delta Z_m = -\Sigma^q(\not{k} = m), \tag{4.7}$$

$$\delta_{ij}\delta Z_2 = \frac{\partial}{\partial \not{k}}\Sigma^q(\not{k})|_{\not{k}=m}. \tag{4.8}$$

The explicit forms of the above equalities are

$$\begin{aligned}
\delta Z_m^{OS} &= -3C_F\left(\frac{g_s}{4\pi}\right)^2\left(\frac{1}{\epsilon_{UV}} - \gamma_E + \ln\left(\frac{4\pi\mu^2}{m^2}\right) + \frac{4}{3}\right) \\
&= -3C_F\left(\frac{g_s}{4\pi}\right)^2\left(\frac{1}{\hat{\epsilon}_{UV}} + \ln\left(\frac{\mu^2}{m^2}\right) + \frac{4}{3}\right),
\end{aligned} \tag{4.9}$$

$$\begin{aligned}
\delta Z_2^{OS} &= -C_F\left(\frac{g_s}{4\pi}\right)^2\left(\frac{1}{\epsilon_{UV}} - \gamma_E + \ln\left(\frac{4\pi\mu^2}{m^2}\right) + 2\right) \\
&- C_F\frac{g_s}{4\pi}\left[2\left(\frac{1}{\epsilon_{IR}} - \gamma_E + \ln\left(\frac{4\pi\mu^2}{m^2}\right)\right) + 2\right] \\
&= -C_F\left(\frac{g_s}{4\pi}\right)^2\left[\frac{1}{\hat{\epsilon}_{UV}} + \ln\left(\frac{\mu^2}{m^2}\right) + 2\right] \\
&\quad -C_F\left(\frac{g_s}{4\pi}\right)^2\left[2\frac{1}{\hat{\epsilon}_{IR}} + \ln\left(\frac{\mu^2}{m^2}\right) + 2\right],
\end{aligned} \tag{4.10}$$

where

$$\frac{1}{\hat{\epsilon}_{UV}} = \frac{1}{\epsilon_{UV}} - \gamma_E + \ln(4\pi) \tag{4.11}$$

and

$$\frac{1}{\hat{\epsilon}_{IR}} = \frac{1}{\epsilon_{UV}} - \gamma_E + \ln(4\pi). \tag{4.12}$$

Including the renormalized parameters and fields, one obtains the renormalized Green functions $G_R^{(n)}(p_1, \cdots, p_n)$, and the renormalized vertex functions $\Gamma_R^{(n)}(p_1, \cdots, p_n)$, which are the renormalized one-particle irreducible n-point functions. The renormalized two-point function $\Gamma_R^{(2)}$ is the inverse of the propagator up to a factor

$$\Gamma_R^{(2)}(p, -p)G_R^{(2)}(p, -p) = -1. \tag{4.13}$$

The on-shell renormalization conditions ensure that the real parts of the poles of the propagators are given by the mass parameters of the Lagrangian and therefore they are the physical particle masses. Furthermore, the propagators are required to have the

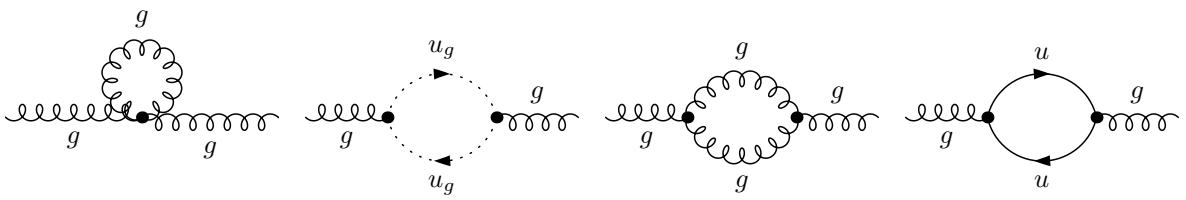

Figure 4.2: Generic Feynman diagrams contributing to the gluon self energy.

residue equal to unity. The propagator residues appear as $\mathcal{Z}$-factors in the Lehman-Symanzik-Zimmerman (LSZ) [57] reduction formula, which describes the transition from Green functions to the S-matrix. Requiring the residues to be unity, implies that no radiative corrections for external lines have to be taken into account.

4.1.2 Gluon self-energy

To calculate the gluon field renormalization constant, one should add the contributions originating from the gluon-loop together with the corresponding ghost-loop, and the massless-quark loop. Note that in dimensional regularization the diagrams involving a four-gluon vertex vanish. The corresponding Feynman diagrams are shown in Fig. 4.2. We know the Lorentz structure of these contributions due to the Slavnov-Taylor identity

$$\Pi^{ab}_{\mu\nu}(k) = \delta^{ab}(k_\mu k_\nu - k^2 g_{\mu\nu})\Pi(k^2), \tag{4.14}$$

$$\delta^{ab}\Pi(k^2) = -\frac{1}{(n-1)k^2} g^{\mu\nu}\Pi^{ab}_{\mu\nu}(k). \tag{4.15}$$

The renormalized gluon self-energy is obtained by summing the unrenormalized gluon self-energy with the corresponding gluon field renormalization constants

$$\Pi^{R}_{\mu\nu}(k) = \delta^{ab}(k_\mu k_\nu - k^2 g_{\mu\nu})\Pi(k^2) + \delta^{ab}(k_\mu k_\nu - k^2 g_{\mu\nu})\delta Z_3. \tag{4.16}$$

The renormalization condition for the gluon-self energy in the *On-shell* scheme is

$$Re\ \Pi(k^2)|_{k^2=0} = 0, \tag{4.17}$$

and it leads to

$$\delta Z_3^{OS} \;=\; -(\ \Pi_R^{g,gluon}(k^2=0) + \Pi_R^{g,ghost}(k^2=0) + n_{lf}\Pi_R^{g,q}(k^2=0, m=0)\ ), \tag{4.18}$$

where we consider $n_{lf} = 3$ light active flavours. The renormalization constants given above do not only contain the UV-divergences necessary to render the two-point functions UV-finite, but also the IR-divergences.

We shall calculate further only $\Pi(k^2)$. Note that we should treat the gluon and the ghost loop together since only their sum verifies the Slavnov-Taylor identity. We must also multiply the loop with two identical particles by 1/2! and (-1) due to the boson and the fermion statistics respectively:

$$\begin{aligned}
\Pi(k^2)^{g;gluon+ghost} &= -iC_A \frac{g_s^2 \mu^{2\epsilon}}{(n-1)k^2} \int \frac{d^n q}{2\pi^2} \frac{(3n-4)k\cdot q - k^2}{q^2(q+k)^2}, && (4.19)\\
\Pi(0)^{g;gluon+ghost} &= iC_A g_s^2 \frac{3n-4}{2(n-1)} B_0(0,0,0) \\
&= -C_A \left(\frac{g_s}{4\pi}\right)^2 \frac{5}{3} \left(\frac{1}{\hat{\epsilon}_{UV}} - \frac{1}{\hat{\epsilon}_{IR}}\right), && (4.20)
\end{aligned}$$

where the expression for $B_0(0,0,0)$ is given in Eq. (C.5). For massless quark loops, the calculation is very similar to that for gluon loops:

$$\begin{aligned}
\delta^{ab}\Pi(k^2)^{g;q} &= -4ig_s^2 \mu^{2\epsilon} Tr[T^a T^b] \int \frac{d^n q}{(2\pi)^n} \frac{Tr[\gamma_m u(\not{q} + m_q)\gamma^\mu (\not{q} + \not{k} + m_q)]}{(q^2 - m_q^2)((q+k)^2 - m_q^2)}, && (4.21)\\
\delta^{ab}\Pi(0)^{g;q} &= -\delta^{ab} g_s^2 \frac{2i}{(n-1)} B_0(0,0,0) \\
&= \delta^{ab} \left(\frac{g_s}{4\pi}\right)^2 \frac{2}{3} \left(\frac{1}{\hat{\epsilon}_{UV}} - \frac{1}{\hat{\epsilon}_{IR}}\right). && (4.22)
\end{aligned}$$

Adding all contributions and taking into account that there are n_{lf} light quark active flavours, we obtain the expression for the gluon self energy and implicitly the gluon field renormalization constant

$$\delta Z_3^{OS} = \left(\frac{g_s}{4\pi}\right)^2 \Big[-(2C_A - \beta_0) \left(\frac{1}{\hat{\epsilon}_{UV}} - \frac{1}{\hat{\epsilon}_{IR}}\right) \Big], \tag{4.23}$$

where we have introduced $\beta_0 = 11 - 2n_{lf}/3$.

4.1.3 Strong coupling constant renormalization

We have used the *modified Minimal Subtraction* ($\overline{\text{MS}}$) scheme to renormalize the strong coupling constant. In this scheme the renormalization constants contain divergences and some accompanying terms but no other process dependent finite terms.
Using the Slavnov-Taylor identity (4.2), we obtain further the renormalization constant of the strong coupling constant in the $\overline{\text{MS}}$ scheme

$$\delta Z_g = -\frac{1}{2} \left(\frac{g_s}{4\pi}\right)^2 \beta_0 \frac{1}{\hat{\epsilon}_{UV}}. \tag{4.24}$$

In the definition of the renormalized strong coupling constant, $g_s^0 = Z_g g_s$, we have to employ dimensional-regularization in order to make the equation mathematically meaningful. Then the bare and the renormalized coupling constant acquire mass dimensions. We can explicitly isolate these mass dimensions as

$$\begin{aligned} g_s^0 &= \widetilde{g_s^0}\ \mu_0^\epsilon, \\ g_s &= \widetilde{g_s}\ \mu^\epsilon, \end{aligned}$$

where $\widetilde{g_s^0}$ and $\widetilde{g_s}$ are dimensionless quantities and they do not depend on the scales. The mass scale μ_0 is seen as a fixed parameter, while the mass parameter μ is in fact identified with the renormalization scale in $\overline{\text{MS}}$ scheme. With the usual argument that the bare strong coupling does not depend on the renormalization scale,

$$\frac{\partial (g_s^0)^2}{\partial \ln \mu^2} = 0, \tag{4.25}$$

and the relation between bare and renormalized strong coupling constants,

$$(g_s^0)^2 = (1 + 2\delta Z_g) g_s^2 + \mathcal{O}(g_s^6), \tag{4.26}$$

we obtain the *renormalization group equation* (RGE) of the running strong coupling constant at LO

$$\begin{aligned} \frac{\partial g_s^2}{\partial \ln \mu^2} &= -2 \frac{\partial \delta Z_g}{\partial \ln \mu^2} + \mathcal{O}(g_s^6) \\ &= -\left(\frac{g_s}{4\pi}\right)^2 \beta_0 + \mathcal{O}(g_s^6) = -\frac{\beta_0}{4\pi} \alpha_s^2(\mu^2) + \mathcal{O}(\alpha_s^3). \end{aligned} \tag{4.27}$$

This relation ensures that in the running strong coupling, only the $n_{lf} = 3$ light flavours contribute .

When summing all orders of the perturbation theory, the result is independent of the artificially introduced renormalization scheme. In practice, one truncates the series expansion at an order k which leads to a dependence on the renormalization scale of order $k+1$. The remaining renormalization-scale dependence quantifies part of the theoretical uncertainties caused by the unknown HO corrections. Such a technique was used in Chapter 3, where an estimate of the theoretical errors was explicitly performed.

4.2 Virtual corrections to $\gamma\gamma \to c\bar{c}[\ ^3S_1^{[1]}\ ] + \gamma$

In Chapter 3, we studied for the direct channel two different LO processes: one contains a photon in the final state together with the $c\bar{c}$ pair, the other one contains a jet (gluon

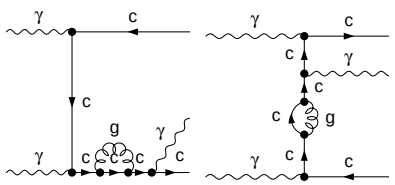

Figure 4.3: Self-energy type Feynman diagrams for virtual corrections to $\gamma\gamma \to c\bar{c} + \gamma$.

originating). In this section we study virtual corrections for each of these processes. In the next Chapter, real corrections are also analyzed in order to complete the NLO contributions. NRQCD provides a consistent framework in which to study these processes, but also requires an interplay between processes with different quantum numbers for the outgoing $c\bar{c}$ bound states. The virtual cross section can be calculated using the same expression for the phase space as for the born cross section, since there is no additional particle in the final state. Following the same method we used to obtain Eq. (3.16) we find

$$\begin{aligned} \frac{\hat{d\sigma}_v}{dt_1 du_1} &= \frac{\phi K_c}{8\pi s} \frac{K_s}{\Gamma(1-\epsilon)} \left(\frac{t\ u}{4\pi\mu^2 s} \right)^{\frac{n-4}{2}} \\ &\times \delta(s+t+u-4m_c^2) \sum_{col,pol} (\mathcal{M}_b \mathcal{M}_v^\star + \mathcal{M}_v \mathcal{M}_b^\star). \end{aligned} \tag{4.28}$$

Since at LO $\gamma\gamma \to J/\Psi + \gamma$ can produce only charmonium in the ${}^3S_1^{[1]}$ and ${}^1P_0^{[1]}$ states, we restrict our virtual corrections to the first case due to the fact that $\langle \mathcal{O}[{}^1P_0^{[1]}] \rangle$ is highly suppressed by velocity-scaling rules.

The corresponding Feynman diagrams for virtual corrections to the process $\gamma\gamma \to c\bar{c}[{}^3S_1^{[1]}] + \gamma$ can be collected into five classes as follows

- 12 diagrams which contain self-energy insertions in the internal quark propagators. Two examples from this class are shown in Fig. 4.3. Their interference with the born terms reveal UV-divergences, present in the two-point functions involved, and are IR-finite since the charm quark and anti-quark are considered massive. Note that for external legs we have introduced the quark wave function renormalization.

- 18 diagrams of the quark-photon vertex corrections type, shown in Fig. 4.4. They are UV-divergent and IR-finite .

- $8 + 4$ Abelian box diagrams. Two examples are shown in Fig. 4.5. They are UV- and IR- finite.

- 6 pentagon-like diagrams that contain only Abelian vertices, shown in Fig. 4.6. We call them Abelian pentagon diagrams, and the five-point functions required in their computation are called Abelian five-point functions. They are UV-finite and IR- and Coulomb-divergent. Their calculation requires up to five-point scalar and tensor integrals. Since the five-point integrals are not yet implemented in an automatic package we have discussed them in detail in App. C.1.

- $8n_{lf} + 4n_{lf}$ vertex-type and $6n_{lf}$ box-type diagrams containing light quark loops shown in Fig. 4.7. They do not give any contribution to the virtual corrections of the process $\gamma\gamma \to c\bar{c}[^3S_1^{[1]}] + \gamma$ due to their colour ($Tr[T^a] = 0$) and Dirac (Furry's theorem) structure .

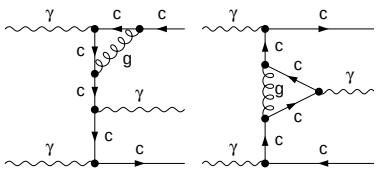

Figure 4.4: Feynman diagrams for virtual corrections to the quark-photon vertex in $\gamma\gamma \to c\bar{c} + \gamma$.

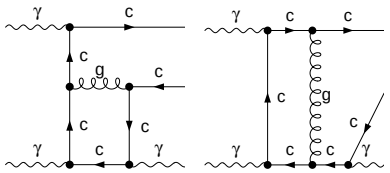

Figure 4.5: Box-type Feynman diagrams for the virtual corrections to $\gamma\gamma \to c\bar{c} + \gamma$.

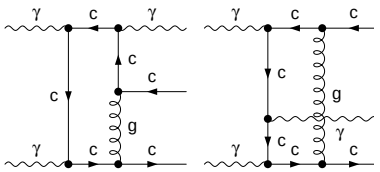

Figure 4.6: Pentagon Feynman diagrams present in the virtual corrections to $\gamma\gamma \to c\bar{c}+\gamma$.

4.2.1 Cancellation of UV-, IR-, and Coulomb-singularities

- Cancellation of UV-divergences
  As we have already discussed at the beginning of this Chapter, the UV-singularities are eliminated when adding the virtual contributions to the subsequent counterterms. For our renormalization scheme we have chosen the *On-shell* scheme for this

particular process. For an explicit check of the UV-finiteness, we should add to the virtual contributions the corresponding quark mass counterterm Z_m^{OS} given in Eq. (4.9) and quark-field counterterm Z_2^{OS} given in Eq. (4.10):

$$\begin{aligned} & 2Re\ (\ \mathcal{M}_{born}\mathcal{M}^{\star}_{self}\ )_{UV} + 2Re\ (\ \mathcal{M}_{born}\mathcal{M}^{\star}_{MassCT}\ )_{UV} \\ + \quad & 2Re\ (\ \mathcal{M}_{born}\mathcal{M}^{\star}_{vertex}\ )_{UV} + 2Re\ (\ \mathcal{M}_{born}\mathcal{M}^{\star}_{WfCT}\ )_{UV} \\ = \quad & (\ 4(Z_2^{OS}-1\ )_{UV} - 6(\ Z_2^{OS}-1\ )_{UV} + 2(\ Z_2^{OS}-1)_{UV}\ )\ |\ \mathcal{M}_{born}\ |^2 \\ = \quad & 0_{UV}, \end{aligned} \tag{4.29}$$

where the the sum $2Re\ (\ \mathcal{M}_{born}\mathcal{M}^{\star}_{self}\ )_{UV} + 2Re\ (\ \mathcal{M}_{born}\mathcal{M}^{\star}_{MassCT})_{UV}$ is replaced by $4(Z_2^{OS}-1\ )_{UV}$.

- Cancellation of IR-singularities
  In the virtual contributions only Abelian pentagon-like diagrams contain IR-singularities. These will be canceled against those present in the corresponding counterterms for the renormalization of the quark field. In a mathematical formulation this can be written as

$$\begin{aligned} & 2Re\ (\ \mathcal{M}_{born}\mathcal{M}^{\star}_{pent}\ )_{IR} + 2Re\ (\ \mathcal{M}_{born}\mathcal{M}^{\star}_{WfCT}\ )_{IR} \\ = \quad & (\ -2(\ Z_2^{OS}-1)_{IR} + 2(\ Z_2^{OS}-1)_{IR}\ )\ |\ \mathcal{M}_{born}\ |^2 \\ = \quad & 0_{IR}. \end{aligned} \tag{4.30}$$

- Cancellation of Coulomb singularities
  When a longitudinal gluon is exchanged between the external quark and anti-quark legs, the cross section is affected by Coulomb-singularities. This is the case for Abelian pentagon diagrams shown in Fig. 4.6. Their IR- and Coulomb- divergent structures are similar up to a prefactor. Explicitly, they are fully contained in the

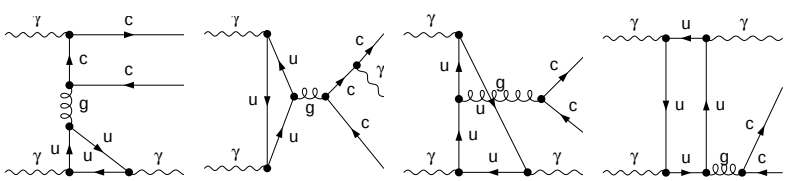

Figure 4.7: Triangle and box Feynman diagrams containing light-quark loops present in the virtual corrections for $\gamma\gamma \to c\bar{c} + \gamma$.

scalar three-point functions discussed in App. C.1. The interference of the pentagon with the born diagrams gives

$$2Re\ (\ \mathcal{M}_{born}\mathcal{M}^{\star}_{pent}\ )_{Coulomb} = C_F\frac{\alpha_s}{\pi}\frac{\pi^2}{2v}\mid \mathcal{M}_{born}\mid^2\langle\mathcal{O}_1[^3S_1]\rangle. \tag{4.31}$$

As we have discussed in Section 2.3, radiative corrections should also be considered for the operator matrix elements multiplying the hard scattering cross section, in order to have a consistent NLO analysis. For the process analyzed here, we have only a $\langle\mathcal{O}_1[^3S_1]\rangle$ operator. Its Coulomb correction is given in Eq. (2.42) with the subsequent coefficient expressed in Eq. (2.41):

$$\langle\mathcal{O}_1[^3S_1]\rangle = \langle\mathcal{O}_1[^3S_1]\rangle_{born}\left(1 + C_F\frac{\pi\alpha_s}{2v}\right). \tag{4.32}$$

Now, if we take the sum of the born and NLO cross sections in a consistent way, we get

$$\begin{aligned}
&[\ \mid \mathcal{M}_{born}\mid^2 + 2Re\ (\ \mathcal{M}_{born}\mathcal{M}^{\star}_{virt}\ )_{Coulomb}\ ]\ \langle\mathcal{O}_1[^3S_1]\rangle_{born}\\
=\ &\left(\ 1 + C_F\frac{\alpha_s}{\pi}\frac{\pi^2}{2v}\ \right)\ \mid \mathcal{M}_{born}\mid^2\langle\mathcal{O}_1[^3S_1]\rangle\left(1 - C_F\frac{\pi\alpha_s}{2v}\right)\\
=\ &\mid \mathcal{M}_{born}\mid^2\langle\mathcal{O}_1[^3S_1]\rangle + \mathcal{O}(v^2).
\end{aligned} \tag{4.33}$$

Note that radiative corrections to the OMEs bring also UV- and IR-singularities. The UV-divergences are eliminated by the renormalization of the operators. The IR-divergent part will be canceled by the IR-divergences arising in the real corrections [see next Chapter].

4.3 Virtual corrections to $\gamma\gamma \to c\bar{c}[^3S_1^{[1]}] + g$

Part of the Feynman diagrams contributing to this channel are similar (with respect to Dirac structure) with those containing a final photon instead of a final gluon. There are also diagrams containing non-Abelian vertices that cannot be present in the process $\gamma\gamma \to c\bar{c}[^3S_1^{[1]}] + \gamma$. We shall not show further diagrams that differ from those already presented in the last subsection only by the replacement of the final photon with a final gluon. We shall present instead new classes of diagrams containing triple gluon vertices. We can classify the complete set of Feynman diagrams as follows:

- 12 self-energy type diagrams, like those presented in Fig. 4.3 with the replacement $\gamma \to g$ for the final gluon. They are UV-divergent and IR-finite.

- 18 diagrams containing corrections to the Abelian quark-gluon vertex, similar to those in Fig. 4.4. They are also UR-divergent and IR-finite.

- 6 diagrams containing virtual corrections to the gluon-gluon couplings (non-Abelian triple gluon couplings only). They are shown in Fig. 4.8. They are UV- and IR-divergent. The IR-singularities show up as simple $1/\epsilon$ and double $1/\epsilon^2$ poles, and they cancel against real and counterterm contributions.

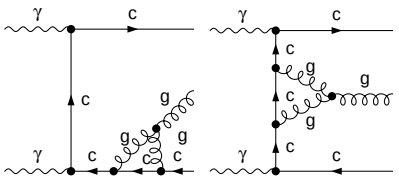

Figure 4.8: Feynman diagrams for virtual corrections to the gluon-gluon vertex at $\gamma\gamma \to c\bar{c} + g$.

- $8n_{lf}$ triangle diagrams containing light quark loops of the type shown in Fig. 4.7(a). Each of them cancel for this particular final state of $c\bar{c}$ pairs because of the Dirac structure of the heavy quark lines.

- $6n_{lf}$ diagrams containing light quarks inside the loop, like those presented in Fig. 4.9. They do not give any contribution to the virtual corrections: the sum of two diagrams differing only by the light quark flow inside the loop and containing an odd number of vector couplings cancel (Furry's theorem).

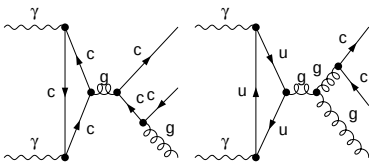

Figure 4.9: Triangle-type Feynman diagrams containing light-quark loop present in the virtual corrections for $\gamma\gamma \to c\bar{c} + g$.

- $8 + 4$ Abelian box diagrams similar to those plotted in Fig. 4.5. They are both IR- and UV-finite. They are treated in the same way as discussed in the last section for the subsequent diagrams.

- 4 box diagrams containing non-Abelian triple gluon couplings. An example is shown in Fig. 4.10. They are UV-finite but are plagued by IR-singularities. These appear again as simple and double poles.

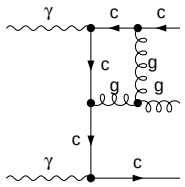

Figure 4.10: Box-type Feynman diagrams containing non-Abelian triple gluon vertex, arising in the process $\gamma\gamma \to c\bar{c} + g$.

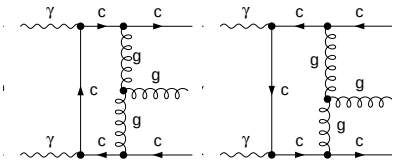

Figure 4.11: Pentagon Feynman diagrams, present in the virtual corrections for $\gamma\gamma \to c\bar{c} + g$, that contain a triple-gluon vertex.

- $6n_{lf}$ box diagrams containing light quark loops similar to those shown in Fig. 4.7. But they do not vanish neither individually in this channel due to their colour structure, as in the case of $\gamma\gamma \to c\bar{c}[^3S_1^{[1]}] + \gamma$, nor in the sum of them as in the case of triangle-type loops, because now there are two photons and two gluons coupled to the quark loop. Although individual diagrams contain IR divergences arising as simple and double poles and UV singularities, the sum of all diagrams of such type is free of IR- and UV divergences. Their computation requires two-, three- and four- point integrals with vanishing masses for the propagators. Their analytical expressions are given in App. B1.

- 6 pentagon diagrams containing only quark-gluon vertices. They are as before plagued by IR- and Coulomb-singularities. The cancellation of these singularities will be shown later.

- 2 pentagon diagrams containing three-gluon vertices. They are shown in Fig. 4.11. They suffer also from IR- and UV- divergences. In principle, to compute such pentagon diagrams one would need scalar and tensorial five-point integrals. Since they contain non-Abelian vertices, we are not allowed to assign a small mass to the gluon and use it as an IR regulator. Fortunately, the momenta flowing inside the loop propagators are linear dependent and we can simply decompose a five-point integral to a set of four four-point integrals. The four-point integrals are known (most of

them implemented in Mathematica and the Fortran package LoopTools) and their Passarino-Veltman reduction is already implemented in an automatic Mathematica package FeynCalc. More details about this type of five point functions can be found in App. C.

4.3.1 Cancellation of the divergences

As usual, UV- divergences are eliminated after we consider the renormalization of QCD parameters and fields. For the process $\gamma\gamma \to c\bar{c}(^3S_1^{[8]}) + g$ we have chosen the following renormalization framework:

- we have renormalized the heavy quark masses and fields and the gluon field *on-shell*. The analytical expressions for the mass Z_m^{OS} and wave-function Z_2^{OS} and gluon field Z_3^{OS} renormalization constants are given in equations Eq. (4.9), Eq. (4.10) and Eq. (4.23).

- we have renormalized the strong coupling constant in the $\overline{\rm MS}$ scheme. The subsequent analytical expression of the implied renormalization constant is given in equations Eq. (4.24).

Through this section we show the explicit cancellation of UV-, Coulomb- and part of the IR- singularities. The remaining IR-divergent terms will be canceled in the sum of virtual with real corrections. This cancellation will be discussed in detail in the next chapter.

- Cancellation of UV-divergences

$$
\begin{aligned}
& 2Re\,(\,\mathcal{M}_{born}\mathcal{M}^{\star}_{self}\,)_{UV} + 2Re\,(\,\mathcal{M}_{born}\mathcal{M}^{\star}_{massCT}\,)_{UV} \\
+ \;& 2Re\,(\,\mathcal{M}_{born}\mathcal{M}^{\star}_{vertex}\,)_{UV} + 2Re\,(\,\mathcal{M}_{born}\mathcal{M}^{\star}_{QwfCT}\,)_{UV} \\
+ \;& 2Re\,(\,\mathcal{M}_{born}\mathcal{M}^{\star}_{g_sCT}\,)_{UV} + 2Re\,(\,\mathcal{M}_{born}\mathcal{M}^{\star}_{gwfCT}\,)_{UV} \\
= \;& 4(Z_2^{OS}-1)_{UV}|\mathcal{M}_{born}|^2 - 6(Z_2^{OS}-1)_{UV}|\mathcal{M}_{born}|^2 \\
+ \;& 2C_A\left(\frac{g_s}{4\pi}\right)^2 B_0(0,0,0)_{UV}|\mathcal{M}_{born}|^2 + 2(Z_2^{OS}-1)_{UV}|\mathcal{M}_{born}|^2 \\
+ \;& 2\frac{1}{2}(Z_3^{OS}-1)_{UV}|\mathcal{M}_{born}|^2 + 2(Z_g-1)_{UV}|\mathcal{M}_{born}|^2 \\
= \;& 2C_A\left(\frac{g_s}{4\pi}\right)^2 \frac{1}{\hat{\epsilon}_{UV}}|\mathcal{M}_{born}|^2 - \left(\frac{g_s}{4\pi}\right)^2\left(\beta_0\frac{1}{\hat{\epsilon}_{UV}}\right) + \left(\frac{g_s}{4\pi}\right)^2\left[-(2C_A-\beta_0)\frac{1}{\hat{\epsilon}_{UV}}\right] \\
= \;& 0_{UV}, \qquad (4.34)
\end{aligned}
$$

where $B_0(0,0,0)$ functions arise from non-Abelian Feynman diagrams.

- Cancellation of IR-divergences
  The IR-singularities arise as simple and double poles of the form $1/\hat{\epsilon}_{IR}, 1/\hat{\epsilon}_{IR}\ln\frac{s_1}{m^2}$, and $1/\hat{\epsilon}^2_{IR}$. The cancellation of IR-singularities is guaranteed by the KLN theorem and it occurs when the virtual and real corrections are added. Since for the presently discussed process there are also real contributions, we shall probe this cancellation in the chapter designated to real corrections. We list below the IR-singularity structure of the virtual matrix elements:

  double poles like $1/\hat{\epsilon}^2_{IR}$

$$\begin{aligned} & 2Re\,(\,\mathcal{M}_{born}\mathcal{M}^{\star}_{vertex}\,)_{IR^2} + 2Re\,(\,\mathcal{M}_{born}\mathcal{M}^{\star}_{box}\,)_{IR^2} + 2Re\,(\,\mathcal{M}_{born}\mathcal{M}^{\star}_{pent}\,)_{IR^2} \\ = \;& -2C_A\left(\frac{g_s}{4\pi}\right)^2\frac{1}{\hat{\epsilon}^2_{IR}}|\mathcal{M}_{born}|^2, \end{aligned} \tag{4.35}$$

  simple poles like $1/\hat{\epsilon}_{IR}\ln\frac{s_1}{m^2}$

$$\begin{aligned} & 2Re\,(\,\mathcal{M}_{born}\mathcal{M}^{\star}_{vertex}\,)_{IR} + 2Re\,(\,\mathcal{M}_{born}\mathcal{M}^{\star}_{box}\,)_{IR} + 2Re\,(\,\mathcal{M}_{born}\mathcal{M}^{\star}_{pent}\,)_{IR} \\ = \;& -4C_A\left(\frac{g_s}{4\pi}\right)^2\left(\frac{1}{\hat{\epsilon}^2_{IR}}\ln\frac{s_1}{m^2}\right)|\mathcal{M}_{born}|^2, \end{aligned} \tag{4.36}$$

  simple poles like $1/\hat{\epsilon}_{IR}$

$$\begin{aligned} & 2Re\,(\,\mathcal{M}_{born}\mathcal{M}^{\star}_{vertex}\,)_{IR} + 2Re\,(\,\mathcal{M}_{born}\mathcal{M}^{\star}_{box}\,)_{IR} + 2Re\,(\,\mathcal{M}_{born}\mathcal{M}^{\star}_{pent}\,)_{IR} \\ + \;& 2Re\,(\,\mathcal{M}_{born}\mathcal{M}^{\star}_{QwfCT}\,)_{IR} + 2Re\,(\,\mathcal{M}_{born}\mathcal{M}^{\star}_{gwfCT}\,)_{IR} \\ = \;& -2C_A\left(\frac{g_s}{4\pi}\right)^2\frac{1}{\hat{\epsilon}_{IR}}|\mathcal{M}_{born}|^2 + 4\left(-\frac{1}{2N_c}\right)\left(\frac{g_s}{4\pi}\right)^2\frac{1}{\hat{\epsilon}_{IR}}|\mathcal{M}_{born}|^2 \\ + \;& 2(Z_2^{OS}-1)_{IR}|\mathcal{M}_{born}|^2 + 2\frac{1}{2}(Z_3^{OS}-1)_{IR}|\mathcal{M}_{born}|^2 \\ = \;& \left(\frac{g_s}{4\pi}\right)^2\left(-2C_A\frac{1}{\hat{\epsilon}_{IR}} - 2C_A\frac{1}{\hat{\epsilon}_{IR}} + (2C_A-\beta_0)\frac{1}{\hat{\epsilon}_{IR}}\right)|\mathcal{M}_{born}|^2 \\ = \;& \left(\frac{g_s}{4\pi}\right)^2\left(-2C_A - 11 + \frac{2}{3}n_{lf}\right)\frac{1}{\hat{\epsilon}_{IR}}|\mathcal{M}_{born}|^2. \end{aligned} \tag{4.37}$$

- Cancellation of Coulomb-singularities
  As in the case of the process $\gamma\gamma \to c\bar{c}[^3S_1^{[1]}] + \gamma$, the Coulomb singularities arising in the Abelian pentagon diagrams are exactly canceled by the Coulomb like radiative corrections to the operator matrix element $\langle\mathcal{O}[^3S_1^{[8]}]\rangle$. After the cancellation of divergences of this type, there is no finite term left. The singularity structure is similar to those discussed in the last section up to the colour factor. Replacing the

specific colour-singlet factor C_F with the appropriate colour-octet factor $-1/(2N_c)$, we get the new Coulomb singular term

$$2Re\ (\ \mathcal{M}_{born}\mathcal{M}^{\star}_{pent}\ )_{Coulomb} = 4\left(-\frac{1}{2N_c}\right)\left(\frac{g_s}{4\pi}\right)^2\frac{\pi^2}{2v}|\mathcal{M}_{born}|^2\langle\mathcal{O}[^3S_1^{[8]}]\rangle. \quad (4.38)$$

Considering also the NLO corrections to the NRQCD operator matrix element

$$\langle\mathcal{O}[^3S_1^{[8]}]\rangle = \left[1+\left(-\frac{1}{2N_c}\right)\frac{\pi\alpha_s}{2v}\right]\langle\mathcal{O}[^3S_1^{[8]}]\rangle_{born}, \quad (4.39)$$

and following the same steps as before, we obtain

$$\begin{aligned}
&\left(|\mathcal{M}_{born}|^2 + 2Re\ (\ \mathcal{M}_{born}\mathcal{M}^{\star}_{virt}\ )_{Coulomb}\right)\langle\mathcal{O}[^3S_1^{[8]}]\rangle_{born} \\
= &\left[1+2\left(-\frac{1}{2N_c}\right)\left(\frac{g_s}{4\pi}\right)^2\right]|\mathcal{M}_{born}|^2\langle\mathcal{O}[^3S_1^{[8]}]\rangle\left[1-\left(-\frac{1}{2N_c}\right)\frac{\pi\alpha_s}{2v}\right] \\
= &\ |\mathcal{M}_{born}|^2\langle\mathcal{O}[^3S_1^{[8]}]\rangle. \quad (4.40)
\end{aligned}$$

We should remember that there are also other types of NLO corrections to the NRQCD matrix element, but they are studied in detail in the next chapter, since the remaining IR-singularities are canceled against real corrections to the born process.

We can conclude that using the usual renormalization procedure for the hard scattering cross section and the NRQCD renormalization procedure for the operators we are able to consistently deal with UV- and Coulomb-singularities. The left over IR-singularities will be further studied in the context of real corrections where not only OMEs present in the born process play a roll but also OMEs at higher order relative to v^2 enter into the game. As we shall show, NRQCD provides us with a consistent framework to eliminate all singularities, in contrast with the CSM which was not able to deal with IR-singularities arising in NLO analyses.

Chapter 5

Real Corrections

In inclusive J/Ψ production only this outgoing particle is observed, and all information about the other final particles involved is lost, except for what we can learn from the conservation laws. For example, we do not have information about the number of final particles produced in the hard scattering process and about their four-momenta. If we restrict our studies to NLO corrections in α_s, then relative to the LO graphs only one additional particle (g, q, or $\bar{q}$) can be produced. Thus, we have to consider now the $2 \to 3$ processes which interfere with each other, but we have to add them incoherently to Born and virtual contributions. Mathematically, this can be expressed as:

$$|\mathcal{M}_{Born} + \mathcal{M}_{virt}|^2 + |\mathcal{M}_{real}|^2 = |\mathcal{M}_{Born}|^2 + 2Re\ (\ \mathcal{M}_{Born}\mathcal{M}^{\star}_{virt}\ ) + |\mathcal{M}_{real}|^2. \qquad (5.1)$$

In practical work the real contributions have to be integrated over the appropriate $2 \to 3$ *phase space*. In particular, the unknown four-momenta of the unobserved particles should be integrated out. For some kinematical regions these integrals become divergent. To regularize them we use as before *dimensional regularization* with $n = 4 - 2\epsilon$. They are of IR-type, soft or collinear, and they cancel in the sum with virtual contributions. This cancellation is guaranteed by the (KLN) [28] theorem and it will also be shown explicitly for the processes that we are studying.

We focus our analysis on two different channels:

$$\begin{aligned} \gamma\gamma &\to c\bar{c}[n] + \gamma + g, \\ \gamma\gamma &\to c\bar{c}[n] + g + g. \end{aligned} \qquad (5.2)$$

Although they scale with different powers of α_s, they can generate contributions with similar size, since we are dealing with a double expansion in α_s and v. Before we start the analysis of the individual processes, we discuss the parameterization of the accessible

$2 \to 3$ phase space and its decomposition into soft, collinear and hard parts. We consider a $2 \to 3$ process as a $2 \to 2$ process where the J/Ψ-particle and an intermediate-particle ξ are produced, followed by the decay of the intermediate-particle to the other two outgoing partons.

We choose the CMS for the incoming particles and parameterize the subsequent four-momenta as follows:

$$\begin{aligned}
k_1 &= \frac{\sqrt{s}}{2}(1, \cdots, \sin\chi, 0, \cos\chi), \\
k_2 &= \frac{\sqrt{s}}{2}(1, \cdots, -\sin\chi, 0, -\cos\chi), \\
P_{J/\Psi} &= (E_{J/\Psi}, \cdots, 0, 0, p_{J/\Psi}), \\
Q &\equiv k_1 + k_2 = (\sqrt{s}, \vec{0}), \\
k_3 &= (\omega_3, \cdots, \omega_3 \sin\theta_3 \sin\phi_3, \omega_3 \sin\theta_3 \cos\phi_3, \omega_3 \cos\theta_3), \\
k_4 &= (\omega_4, \cdots, \omega_4 \sin\theta_4 \sin\phi_4, \omega_4 \sin\theta_4 \cos\phi_4, \omega_4 \cos\theta_4).
\end{aligned} \tag{5.3}$$

We define the Mandelstam variables in a similar manner to that for LO processes:

$$\begin{aligned}
s &= (k_1 + k_2)^2, \\
t_1 &= -2k_1 \cdot P_{J/\Psi} = -\sqrt{s}(E_{J/\Psi} + p_{J/\Psi}\cos\chi), \\
u_1 &= -2k_2 \cdot P_{J/\Psi} = -\sqrt{s}(E_{J/\Psi} - p_{J/\Psi}\cos\chi).
\end{aligned} \tag{5.4}$$

The relations between the energy $E_{J/\Psi}$, angular orientation of the J/Ψ-particle, and the Mandelstam variables are

$$\begin{aligned}
E_{J/\Psi} &= -\frac{t_1 + u_1}{2\sqrt{s}}, \\
\cos\chi &= \frac{u_1 - t_1}{2\sqrt{s}\, p_{J/\Psi}}, \\
\left|\frac{\partial(E_{J/\Psi}, \cos\chi)}{\partial(t_1, u_1)}\right| &= \frac{1}{2s\, p_{J/\Psi}}.
\end{aligned} \tag{5.5}$$

We must now introduce the new invariants (specific for $2 \to 3$ scattering processes)

$$\begin{aligned}
s_3 &= (k_3 + k_4)^2, \\
s_4 &= (P_{J/\Psi} + k_4)^2 - 4m_c^2, \\
s_5 &= (P_{J/\Psi} + k_3)^2 - 4m_c^2, \\
t_6 &= (k_2 - k_3)^2, \\
u_6 &= (k_1 - k_3)^2,
\end{aligned}$$

$$
\begin{aligned}
t_8 &= (k_1 - k_4)^2, \\
u_8 &= (k_2 - k_4)^2,
\end{aligned}
\tag{5.6}
$$

in order to describe the real MEs. Due to kinematical constraints, only $3 \cdot 3 - 4 = 5$ invariants are independent, and the real MEs can be expressed in terms of these five independent Mandelstam variables.

The accessible phase-space for processes like $2 \to 3$ can be expressed as

$$
\begin{aligned}
\int dPS_{2\to 3} &= \mu^{2(4-n)} \int \frac{d^n P_{J/\Psi}}{(2\pi)^{n-1}}\, \delta(P_{J/\Psi}^2 - 4m_c^2)\, \frac{d^n k_3}{(2\pi)^{n-1}}\, \delta_+(k_3^2)\, \frac{d^n k_4}{(2\pi)^{n-1}}\, \delta_+(k_4^2) \\
&\times (2\pi)^n\, \delta^{(n)}(k_1 + k_2 - P_{J/\Psi} - k_3 - k_4) \\
&= \mu^{(4-n)} \int \frac{d^{n-1} P_{J/\Psi}}{(2\pi)^{n-1} 2E_{J/\Psi}}\, \frac{d^n \xi}{(2\pi)^{n-1}}\, (2\pi)^n\, \delta^{(n)}(k_1 + k_2 - P_{J/\Psi} - \xi) \\
&\times \mu^{(4-n)} \int \frac{d^{n-1} k_3}{(2\pi)^{n-1} 2\omega_3} \frac{d^{n-1} k_4}{2\omega_4}\, \delta^{(n)}(\xi - k_3 - k_4) \\
&\equiv \int dPS^{\star}_{2\to 2} \times \int dPS^{\star}_{1\to 2}.
\end{aligned}
\tag{5.7}
$$

We can easily integrate over the $dPS^{\star}_{2\to 2}$ as follows:

$$
\begin{aligned}
\int dPS^{\star}_{2\to 2} &= \mu^{4-n} \frac{1}{(2\pi)^{(n-2)}} \int \frac{|p_{J/\Psi}|^{n-2}}{2E_{J/\Psi}} dp_{J/\Psi} \sin^{n-3}\chi d\chi d\Omega_{n-2} \\
&= \mu^{4-n} \frac{1}{(2\pi)^{(n-2)}} \int \frac{|p_{J/\Psi}|^{n-2}}{2p_{J/\Psi}} dE_{J/\Psi} (1 - \cos^2\chi)^{\frac{n-4}{2}} d\cos\chi \frac{2\pi^{\frac{n-2}{2}}}{\Gamma(\frac{n-2}{2})} \\
&= \frac{1}{8\pi s} \left(\frac{t_1 u_1 - 4m_c^2 s}{4\pi\mu^2 s} \right)^{-\epsilon} \frac{1}{\Gamma(1-\epsilon)} \int dt_1 du_1.
\end{aligned}
\tag{5.8}
$$

To compute the $dPS^{\star}_{1\to 2}$ it is convenient to integrate it separately for different kinematical regions and use the appropriate parameterizations. For the process $\gamma\gamma \to c\bar{c}[n] + g + g$ there are two sources of IR-divergences, which occur in different regions of the phase space:

- If one of the two gluons is *soft*, $E_g^3 \leq E_g^{min}$ or $E_g^4 \leq E_g^{min}$, the real MEs contain soft singularities.
- If two *hard* gluons, where $E_g^{3,4} > E_g^{min}$, become parallel, *i.e.* $\sphericalangle(\vec{k_3}, \vec{k_4}) \leq \delta$, the MEs contain *collinear* singularities.
- If the two gluons are collinear and one of them is soft, then the MEs contain soft-collinear singularities.

In the dimensional regularization used in this work, the IR-singularities arise as simple and double poles in ϵ.

In order to make quantitative predictions, we introduce new parameters defined with respect to the CMS of the incoming particles as

$$\begin{aligned} x_g^{(3)} &= \frac{2\omega_3}{\sqrt{s}}, \\ x_g^{(4)} &= \frac{2\omega_4}{\sqrt{s}}, \\ \cos\theta_{34} &= 1 - \frac{(k_3\cdot k_4)Q^2}{(k_3\cdot Q)(k_4\cdot Q)}, \end{aligned} \tag{5.9}$$

where $x_g^{(i)}$ is the fraction of energy carried by particle $i = 3, 4$ with respect to the center-of-mass (CM) energy $\sqrt{s}$, and θ_{34} is the angle between the two outgoing gluons. One can define different kinematical regions by imposing some restrictions on these parameters. We chose an arbitrarily small *cut-off* parameter x_{cut} and ask for $x_g^{(3),(4)}$ or $\cos\theta_{34}$ to be smaller (larger) than this cut-off. Mathematically, we can decompose the phase space using some trivial properties of the step function:

$$\begin{aligned} 1^{(3)} &= \Theta(x_g^{(3)} - x_{cut}) + \Theta(x_{cut} - x_g^{(3)}), \\ 1^{(4)} &= \Theta(x_g^{(4)} - x_{cut}) + \Theta(x_{cut} - x_g^{(4)}), \\ 1^{(3,4)} &= \Theta(1 - \cos\theta_{34} - x_{cut}) + \Theta(x_{cut} - (1 - \cos\theta_{34})), \end{aligned} \tag{5.10}$$

where $1^{(a)}$ referes to the neutral element of various subspaces. The relevant regions of the phase space are defined starting from the following relation

$$\begin{aligned} & 1^{(3)} \otimes 1^{(4)} \otimes 1^{(3,4)} \\ = \;& \Theta(x_{cut} - x_g^{(3)})\,\Theta(x_g^{(4)} - x_{cut}) + \Theta(x_{cut} - x_g^{(4)})\Theta(x_g^{(3)} - x_{cut}) \\ + \;& \Theta(x_g^{(3)} - x_{cut})\,\Theta(x_g^{(4)} - x_{cut})\,\Theta(x_{cut} - (1 - \cos\theta_{34})) \\ + \;& \Theta(x_g^{(3)} - x_{cut})\,\Theta(x_g^{(4)} - x_{cut})\,\Theta(1 - \cos\theta_{34} - x_{cut}). \end{aligned} \tag{5.11}$$

The first two terms describe the *soft* and *soft + collinear* regions relative to k_3 and k_4, the third defines the *collinear* region and the last term specifies the hard part of the phase space. Obviously, the physical quantities do not depend on the cut-off parameter. We can now perform the remaining phase space integrations ,separately, for each of these regions.

For the process $\gamma\gamma \to c\bar{c}[n] + \gamma + g$, we consider only the decomposition of the phase space into *soft* and *hard* parts relative to the gluon. The corresponding parameterization is given by the relation

$$1^{(4)} = \Theta(x_g^{(4)} - x_{cut}) + \Theta(x_{cut} - x_g^{(4)}). \tag{5.12}$$

Since the charm quark and anti-quark are considered massive we do not have to deal with mass-singularities when the final gluons or photons are emitted parallel with them.

There are other possibilities for defining the different regions of the phase space, *i.e.* we can parameterize it in terms of Lorentz-invariant quantities. Below is given an example for such a parameterization:

$$\begin{aligned} s_3 &= (k_3+k_4)^2 \leq \Delta \text{ defines the IR region of the phase space,} \\ s_3 &= (k_3+k_4)^2 > \Delta \text{ defines the hard region of the phase space.} \end{aligned} \tag{5.13}$$

In our computations we used the first method outlined.

The hard region of the phase space

The last term of Eq. (5.11) specifies that both final particles are hard and do not become parallel. The leftover phase-space integrals can be written further as

$$\begin{aligned} \int dPS^{\star}_{1\to 2} &= \mu^{(4-n)} \int \frac{d^{n-1}k_3}{(2\pi)^{n-1}2\omega_3}\frac{d^{n-1}k_4}{2\omega_4}\,\delta^{(n)}(\xi-k_3-k_4) \\ &\times \Theta(x_g^{(3)}-x_{cut})\,\Theta(x_g^{(4)}-x_{cut})\,\Theta(1-\cos\theta_{34}-x_{cut}) \\ &= \mu^{(4-n)} \int \frac{d^{n-1}k_3}{(2\pi)^{n-1}2\omega_3}\,\frac{1}{2\omega_4}\,\delta(\xi^{(0)}-k_3^{(0)}-k_4^{(0)}) \\ &\times \Theta(x_g^{(3)}-x_{cut})\,\Theta(x_g^{(4)}-x_{cut})\,\Theta(1-\cos\theta_{34}-x_{cut}) \\ &= \frac{\mu^{(4-n)}}{(2\pi)^{n-1}} \int \frac{\omega_3^{n-2}}{4\omega_3\omega_4} d\omega_3 \sin^{n-3}\theta_3 d\theta_3 \sin^{n-4}\phi_3 d\phi_3 d\Omega_{n-3}\,\delta(\xi^{(0)}-k_3^{(0)}-k_4^{(0)}) \\ &\times \Theta(x_g^{(3)}-x_{cut})\,\Theta(x_g^{(4)}-x_{cut})\,\Theta(1-\cos\theta_{34}-x_{cut}). \end{aligned} \tag{5.14}$$

Since we are allowed to choose any CMS for the decay of the pseudo-particle ξ into k_3 and k_4, it is convenient for our calculations to select the CMS of the incoming particles defined in Eq. (5.3). The integrals over $dPS^{\star}_{1\to 2}$ become

$$\begin{aligned} \int dPS^{\star}_{1\to 2} &= \frac{\mu^{(4-n)}}{(2\pi)^{n-1}}\frac{\pi^{\frac{n-3}{2}}}{\Gamma(\frac{n-3}{2})}\frac{1}{4}\int \frac{\omega_3^{n-3}d\omega_3}{\omega_4}\,\delta(\xi^{(0)}-k_3^{(0)}-k_4^{(0)})\,\Theta(x_g^{(3)}-x_{cut}) \\ &\quad \int \sin^{n-3}\theta_3\,d\theta_3\,\Theta(1-\cos\theta_{34}-x_{cut})\,\sin^{n-4}\phi_3\,d\phi_3 \\ &= \frac{(4\pi\mu^2/m_c^2)^{\epsilon}}{(4\pi)^2(2\pi)}\,\frac{\Gamma(1-\epsilon)}{\Gamma(1-2\epsilon)}\,\left(\frac{\omega_3^2}{m_c^2}\right)^{-\epsilon}\frac{s+4m_c^2-2\sqrt{s}E_{J/\Psi}}{(\sqrt{s}-E_{J/\Psi})^2+p_{J/\Psi}^2-2p_{J/\Psi}(\sqrt{s}-E_{J/\Psi})\cos\theta_3} \\ &\quad \Theta(x_g^{(3)}-x_{cut})\int \sin^{n-3}\theta\,d\theta\,\Theta(1-\cos\theta_{34}-x_{cut})\,\sin^{n-4}\phi\,d\phi, \end{aligned} \tag{5.15}$$

and the differential phase space is obtained using in addition Eq. (5.7)

$$\begin{aligned} dPS_{2\to 3} &= \frac{1}{8\pi s}\left(\frac{t_1u_1-4m_c^2s}{4\pi\mu^2 s}\right)^{-\epsilon}\frac{(4\pi\mu^2/m_c^2)^\epsilon}{(4\pi)^2(2\pi)}\frac{1}{\Gamma(1-2\epsilon)}\left(\frac{\omega_3^2}{m_c^2}\right)^{-\epsilon} \\ &\quad \frac{s+4m_c^2-2\sqrt{s}E_{J/\Psi}}{(\sqrt{s}-E_{J/\Psi})^2+p_{J/\Psi}^2-2p_{J/\Psi}}\,\Theta(x_g^{(3)}-x_{cut}) \\ &\times\ dt_1\,du_1\,\sin^{n-3}\theta\,d\theta\,\Theta(1-\cos\theta_{34}-x_{cut})\,\sin^{n-4}\phi\,d\phi. \end{aligned} \tag{5.16}$$

The soft part of the phase space

Integrating over the $1\to 2$ phase space, $dPS^\star_{1\to 2}$, with the corresponding restrictions given in Eq.(5.10), we have

$$\begin{aligned} \int dPS^\star_{1\to 2} &= \mu^{(4-n)}\int\frac{d^{n-1}k_3}{(2\pi)^{n-1}2\omega_3}\frac{d^{n-1}k_4}{2\omega_4}\,\delta^{(n)}(\xi-k_3-k_4)\,\Theta(x_{cut}-x_g^{(3)})\,\Theta(x_g^{(4)}-x_{cut}) \\ &= \mu^{(4-n)}\int\frac{d^{n-1}k_3}{(2\pi)^{n-1}2\omega_3}\,\frac{1}{2\omega_4}\,\delta(\xi^{(0)}-k_3^{(0)}-k_4^{(0)})\,\Theta(x_{cut}-x_g^{(3)})\,\Theta(x_g^{(4)}-x_{cut}) \\ &= \frac{\mu^{(4-n)}}{(2\pi)^{n-1}}\int\frac{\omega_3^{n-2}}{2\omega_3}d\omega_3\,\sin^{n-3}\theta_3\,d\theta_3\,d\Omega_{n-2}\,\Theta(x_{cut}-x_g^{(3)}) \\ &\times\ \frac{1}{2\omega_4}\,\delta(\xi^{(0)}-k_3^{(0)}-k_4^{(0)})\,\Theta(x_g^{(4)}-x_{cut}). \end{aligned} \tag{5.17}$$

If we define

$$dPS^{soft}(3) = \frac{\mu^{(4-n)}}{(2\pi)^{n-1}}\frac{\omega_3^{n-2}}{2\omega_3}d\omega_3\,\sin^{n-3}\theta_3\,d\theta_3\,d\Omega_{n-2}\,\Theta(x_{cut}-x_g^{(3)}), \tag{5.18}$$

we see that the $2\to 3$ phase space in the soft limit factorizes like

$$\begin{aligned} \lim_{k_3\to 0} dPS_{2\to 3} &= \lim_{k_3\to 0} dPS^\star_{2\to 2}\times dPS^\star_{1\to 2} \\ &= \frac{1}{8\pi s}\left(\frac{t_1u_1-4m_c^2s}{4\pi\mu^2 s}\right)^{-\epsilon}\frac{1}{\Gamma(1-\epsilon)}\,dt_1du_1 \\ &\times\ \lim_{k_3\to 0}\,dPS_3^{soft}\frac{1}{2\omega_4}\,\delta(\xi^{(0)}-k_3^{(0)}-k_4^{(0)})\,\Theta(x_g^{(4)}-x_{cut}) \\ &= dPS_{2\to 2}\times dPS^{soft}(3). \end{aligned} \tag{5.19}$$

In the soft or collinear limit, the real MEs factorize either with eikonal factors or with the Altarelli-Parisi splitting functions and Born MEs [58]. In the soft limit, we only have to integrate the corresponding eikonal factors over $dPS^{soft}(3)$, since the Born MEs do not depend on the additional parameters.

The collinear region of the phase space

Since the collinear region is defined as the domain where the relative angle between the two light outgoing particles is smaller than a cutoff parameter and the MEs factorize with the Altarelli-Parisi splitting functions, which depend on the fraction of energy carried by the splitting products, it is natural to parameterize the collinear phase space in terms of the parameters

$$z = \frac{\omega_4}{\omega_3 + \omega_4} \quad , \quad 1 - z = \frac{\omega_3}{\omega_3 + \omega_4} \quad , \quad \cos\theta_{34}. \tag{5.20}$$

If we consider the same CMS as that defined in Eq. (5.3), we get the following restrictions arising from the conservation laws:

$$\begin{aligned} \omega_3 \ \sin\theta_3 - \omega_4 \ \sin\theta_4 &= 0, \\ \omega_3 \ \cos\theta_3 + \omega_4 \ \cos\theta_4 &= \sqrt{\omega_3^2 + \omega_4^2 + 2\omega_3 \ \omega_4 \ \cos\theta_{34}}. \end{aligned} \tag{5.21}$$

Using the last two equations and the collinear approximation, we obtain

$$\begin{aligned} \sin\theta_3 &\simeq z \ \sin\theta_{34}, \\ (\omega_3 + \omega_4) &\simeq p_{J/\Psi}, \\ \left|\frac{\partial(\omega_3, \cos\theta_3)}{\partial(z, \cos\theta_{34})}\right| &\simeq -z^2(\omega_3 + \omega_4), \\ z_{cut} &= x_{cut} \ \frac{s}{s_1}. \end{aligned} \tag{5.22}$$

In the collinear limit the real MEs factorize with the Altarelli-Parisi splitting functions of the partons and the Born MEs:

$$\lim_{k_3 \| k_4} |\mathcal{M}_{real}|^2 \sim g_s^2 \ \frac{1}{k_3 \cdot k_4} P_{i \to kj}(z) |\mathcal{M}_{Born}|^2. \tag{5.23}$$

Note that we include further the factor $1/(k_3 \cdot k_4)$ in the parameterization of the phase space. Using the above mentioned definitions and notations, we get

$$\begin{aligned} \int dPS^{\star}_{1\to 2} &= \mu^{(4-n)} \int \frac{d^{n-1}k_3}{(2\pi)^{n-1} 2\omega_3} \frac{d^{n-1}k_4}{2\omega_4} \ \delta^{(n)}(\xi - k_3 - k_4) \ \frac{1}{k_3 \cdot k_4} \\ &\times \ \Theta(x_g^{(3)} - x_{cut}) \ \Theta(x_g^{(4)} - x_{cut}) \ \Theta(x_{cut} - (1 - \cos\theta_{34})) \\ &= \mu^{(4-n)} \int \frac{d^{n-1}k_3}{(2\pi)^{n-1} 2\omega_3} \ \frac{1}{2\omega_4} \ \frac{1}{\omega_3 \omega_4 (1 - \cos\theta_{34})} \ \delta(\xi^{(0)} - k_3^{(0)} - k_4^{(0)}) \\ &\times \ \Theta(x_g^{(3)} - x_{cut}) \ \Theta(x_g^{(4)} - x_{cut}) \ \Theta(x_{cut} - (1 - \cos\theta_{34})) \\ &= \frac{\mu^{(4-n)}}{(2\pi)^{n-1}} \int \frac{\omega_3^{n-2}}{2\omega_3^2} \ d\omega_3 \ \frac{1}{2\omega_4^2} \ \frac{(1 - \cos\theta_3^2)^{\frac{n-4}{2}}}{(1 - \cos\theta_{34})} \ d\theta_3 \ d\Omega_{n-2} \ \delta(\xi^{(0)} - k_3^{(0)} - k_4^{(0)}) \\ &\times \ \Theta(x_g^{(3)} - x_{cut}) \ \Theta(x_g^{(4)} - x_{cut}) \ \Theta(x_{cut} - (1 - \cos\theta_{34})). \end{aligned} \tag{5.24}$$

If we make a change of variables $(\omega_3, \theta_3) \to (z, \theta_{34})$, we have

$$\begin{aligned}
\lim_{k_3 \| k_4} \frac{1}{k_3 \cdot k_4}\, dPS^{\star}_{1\to 2} &= \frac{\mu^{(4-n)}}{(2\pi)^{n-1}} \left[(1-z)z(\omega_3+\omega_4)\right]^{(n-4)}\, dz \frac{(1-y^2)^{\frac{n-4}{2}}}{(1-y)}\, dy\, d\Omega_{n-2} \\
&\times \Theta(1-z-z_{cut})\, \Theta(x_{cut}-(1-y)) \\
&\times \delta(s_1+t_1+u_1+8m_c^2)\, \Theta(x_g^{(4)}-x_{cut}) \\
&= dPS^{coll}(3,4) \times \delta(s_1+t_1+u_1+8m_c^2)\, \Theta(x_g^{(4)}-x_{cut}), \quad (5.25)
\end{aligned}$$

where we have used the notation $y = \cos\theta_{34}$, and the properties of the step function $\Theta(x_g^{(3)} - x_{cut}) = \Theta(1-z-z_{cut})$. We can also derive a factorization formula of the phase space for the collinear limit:

$$\begin{aligned}
\lim_{k_3 \| k_4} \frac{1}{k_3 \cdot k_4}\, dPS_{2\to 3} &= \lim_{k_3 \| k_4} dPS^{\star}_{2\to 2}\, \frac{1}{k_3 \cdot k_4}\, dPS^{\star}_{1\to 2} \\
&= dPS_{2\to 2} \times dPS^{coll}(3,4), \quad (5.26)
\end{aligned}$$

where $dPS^{coll}(3,4)$ was defined in Eq. (5.25) and $dPS_{2\to 2}$ in Eq. (5.8).

The evaluation of the real-emission MEs in n-dimensions is usually complex. Techniques exist to obtain the soft gluon limits of the amplitudes in non-Abelian gauges [59]. They are based on the eikonal factorization of the sub-amplitudes corresponding to the various colour structures encountered. In the framework of NRQCD we also need a technique to extract the behaviour of different $c\bar{c}$ states in the soft gluon-emission processes, and we chose the one described in Refs [1, 15].

5.1 Real corrections to $\gamma\gamma \to c\bar{c}[n] + \gamma$

At tree-level the possible processes are

$$\gamma\gamma \to c\bar{c}[^3S_1^{[1]}] + \gamma \text{ and}$$
$$\gamma\gamma \to c\bar{c}[^1P_1^{[1]}] + \gamma.$$

At NLO, in the process $\gamma\gamma \to c\bar{c}[n] + \gamma + g$ only colour-octet states can be produced, so that there are no real corrections from the point of view of CSM. Inside CSM the virtual corrections, computed in Section 4.2, are negative and rather large, and the sum of Born and virtual corrections can become negative in some kinematical regions [see Fig. 6.2]. This is, of course, a clear indication that there are inconsistencies inside the theoretical model.

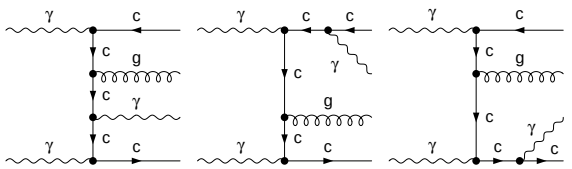

Figure 5.1: Generic Feynman diagrams for the process to $\gamma\gamma \to c\bar{c} + \gamma + g$.

In the NRQCD framework we have to consider all allowed contributions (according to charge, parity, and time-reversal conservation laws), that originate from both colour-singlet and colour-octet states, not only the state with the same quantum numbers as those of the observed meson. The specific processes, within this formalism, are:

$$\begin{aligned} &\gamma\gamma \to c\bar{c}[^1S_0^{[8]}] + \gamma + g, \\ &\gamma\gamma \to c\bar{c}[^3P_j^{[8]}] + \gamma + g \quad \text{with} \quad j = 0, 1, 2. \end{aligned} \tag{5.27}$$

As discussed in the previous Chapter, in the computation of the virtual corrections, Coulomb-singularities arise, which are canceled after considering radiative corrections to the NRQCD operator matrix element $\langle \mathcal{O}_1[^3S_1] \rangle$. In a coherent theory, we should take into account all types of radiative corrections to the NRQCD operator MEs that occur at the same order in α_s. The full NLO analysis of the NRQCD operator MEs have been studied in Chapter 2. It turned out that after renormalization of the $\langle \mathcal{O}_1[^3S_1] \rangle$, the operator still contains IR-divergences [see Eq. (B.34)]. The coefficients of the IR-singularities organize themselves as a sum over the $^3P_j^{[8]}$ operators. We shall show below that, indeed, the real MEs (computed within the NRQCD framework) for the process $\gamma\gamma \to c\bar{c}[^3P_j^{[8]}] + \gamma + g$ also contain IR-divergences. In the sum of these contributions with the Born and the virtual corrections, and considering also NLO corrections to the $\langle \mathcal{O}_1[^3S_1] \rangle$ operator, the IR singularities cancel. The consistent cancellation of all IR-divergences is one of the main improvements from theoretical point of view that NRQCD gives compared with the CSM.

The generic Feynman diagrams corresponding to the process $\gamma\gamma \to c\bar{c} + \gamma + g$ are shown in Fig. 5.1. If we consider a semi-inclusive measurement, where only the J/Ψ-particle is observed, we have to integrate out the degrees of freedom of γ and g. In this context, we refer to the process $\gamma\gamma \to c\bar{c} + \gamma + g$ as real corrections for $\gamma\gamma \to c\bar{c} + \gamma$. If we consider the exclusive measurement, where, additionally, the γ and the g are also observed, we should interpret this process as a LO one. In this Section we are analyzing only the inclusive aspects of the process, and an example of an exclusive analysis is given in Section 6.3. It can be shown *a priori* using Furry's theorem and charge, parity and time-reversal

conservation laws, that the only allowed final states for this process are ${}^1S_0^{[8]}$ and ${}^3P_j^{[8]}$, with $j = 0, 1, 2$. Within the NRQCD approach, the corresponding partonic cross section can be expressed as

$$d\sigma^{real}(\gamma\gamma \to c\bar{c}[n] + \gamma g) = \overline{\sum_{col,pol,[n]}} |\mathcal{M}_{real}\,[n]|^2 \, \frac{\langle \mathcal{O}_8(n) \rangle}{N_{col} N_{pol}} dPS_{2\to 3}, \tag{5.28}$$

where $n = {}^1S_0, {}^3P_j$, with $j = 0, 1, 2$. It turned out that the MEs for the processes producing $c\bar{c}[{}^1S_0^{[8]}]$ in the final states are finite over the full phase space, and they can be directly computed in $n = 4$ dimensions. In the limit of soft gluon emission, they vanish and we can extend the parameterization of the hard region over the whole space. Due to very large expressions obtained for the MEs, we have not computed analytically the entering angular integrals, but only numerically using the VEGAS routine for FORTRAN.

The real MEs of the processes $\gamma\gamma \to c\bar{c}[{}^3P_j^{[8]}] + \gamma + g$, with $j = 0, 1, 2$, contain soft-divergences. To extract the soft-singularities we have decomposed the phase space as discussed in Eq. (5.12) and the technique of soft gluon sub-amplitudes. We start by considering the emission of a soft gluon from the tree-level graphs. A soft-singularity appears only if the gluon is emitted from one of the external lines.

5.1.1 Soft gluon emission

Let us consider the amplitude for the emission of a soft gluon with momentum k_c, colour index c and polarization ϵ_c from a gluon line with momentum p, color index a and polarization ϵ of a generic Born amplitude $\mathcal{M}_a = \mathcal{M}_a^\mu \epsilon_\mu$. In the small k_c limit we get

$$\mathcal{M}_{ac}^\nu = i g_s f_{acb} \, \frac{p^\nu}{p \cdot k_c} \, \mathcal{M}_b + \text{non-singular terms}, \tag{5.29}$$

where we have considered only pure QCD amplitudes. In reality they are multiplied with the corresponding long-distance operators.
Similarly, if we consider emission of a soft gluon from an external quark or anti-quark line with momentum p and colour index i from a generic amplitude $\mathcal{M}_i = \bar{u}(p)\hat{\mathcal{M}}_i$, we obtain

$$\begin{aligned} \mathcal{M}_{ic}^\nu &= g_s \, \frac{p^\nu}{p \cdot k_c} \, T_{ij}^c \, \mathcal{M}_j + \text{non-singular terms}, \\ \mathcal{M}_{ic}^\nu &= -g_s \, \frac{p^\nu}{p \cdot k_c} \, \mathcal{M}_j \, T_{ji}^c + \text{non-singular terms}, \end{aligned} \tag{5.30}$$

where the first equation encounters emission from quark lines and the second one from anti-quark lines. Applying these approximations to the appropriate Feynman diagrams for the processes $\gamma\gamma \to c\bar{c}[{}^3P_j^{[8]}] + \gamma + g$, we have

$$\mathcal{M}^{NLO}_{soft} = T^c_{ij}\; g_s \left(\frac{Q\cdot\epsilon_c}{Q\cdot k_c} - \frac{\bar{Q}\cdot\epsilon_c}{\bar{Q}\cdot k_c} \right) \mathcal{M}_{Born}, \tag{5.31}$$

where $Q = P/2 + q$ and $\bar{Q} = P/2 - q$ denote the momenta of the quark and anti-quark. Projecting onto the colour-singlet subspace of states, we obtain

$$\mathcal{M}^{NLO}_{soft}[1] = \frac{\delta_{ji}}{\sqrt{N_c}} \cdot \mathcal{M}^{NLO}_{soft} = 0, \tag{5.32}$$

and similarly for the colour-octet subspace of states:

$$\begin{aligned} \mathcal{M}^{NLO}_{soft}[8] &= \sqrt{2}\, T^a_{ji} \cdot \mathcal{M}^{NLO}_{soft} \\ &= \sqrt{2}\, T^a_{ji}\, T^c_{ij}\; g_s \left(\frac{Q\cdot\epsilon_c}{Q\cdot k_c} - \frac{\bar{Q}\cdot\epsilon_c}{\bar{Q}\cdot k_c} \right) \mathcal{M}_{Born}, \end{aligned} \tag{5.33}$$

where [1] and [8] refer to a generic colour-singlet and colour-octet state, respectively.

For the S-wave final states we have to constrain $q = 0$, which is equivalent to $Q = \bar{Q} = P/2$ and implies vanishing amplitudes

$$\mathcal{M}^{NLO}_{soft}[{}^1S^{[8]}_0] = 0. \tag{5.34}$$

For the P-wave final states we have to take the derivative with respect to q, the relative momentum between the heavy quark and anti-quark, of the soft limit of amplitudes:

$$\begin{aligned} \left(\frac{d\, \mathcal{M}^{NLO}_{soft}[8]}{d\, q^\beta} \right)_{q=0} &= \sqrt{2}\, T^a_{ji}\, T^c_{ij}\; g_s \left(2\, \frac{\epsilon^\beta_c}{P\cdot k_c} - 2\, \frac{P\cdot\epsilon_c}{(P\cdot k_c)^2}\, k^\beta_c \right) \mathcal{M}_{Born}\Big|_{q=0} \\ &+ \sqrt{2}\, T^a_{ji}\, T^c_{ij}\; g_s \left(\frac{P\cdot\epsilon_c}{P\cdot k_c} - \frac{P\cdot\epsilon_c}{P\cdot k_c} \right) \left(\frac{d\, \mathcal{M}_{Born}}{d\, q^\beta} \right)\Big|_{q=0}. \end{aligned} \tag{5.35}$$

If we consider a transverse gauge so that $P\cdot\epsilon_c = 0$, we have further

$$\left(\frac{d\, \mathcal{M}^{NLO}_{soft}[8]}{d\, q^\beta} \right)_{q=0} = \sqrt{2}\, T^a_{ji}\, T^c_{ij}\; g_s\; 2\; \left(\frac{\epsilon^\beta_c}{P\cdot k_c} \right) \mathcal{M}_{Born}\Big|_{q=0}. \tag{5.36}$$

The soft amplitudes for the production of ${}^3P^{[8]}_j$ states are then simply obtained as

$$\begin{aligned} \mathcal{M}_{S=1,L=1} &= \varepsilon_{\alpha\,\beta}\, \frac{\mathrm{d}}{\mathrm{d}\, q^\beta} \mathrm{Tr}[C[8]\, \Pi^\alpha_1\, \mathcal{M}] \,\Big|_{q=0}, \\ \mathcal{M}_{soft}\,[\,{}^3P^{[8]}_j\,] &= 2\sqrt{2}\, T^a_{ji}\, T^c_{ij}\; g_s\; \left(\frac{\epsilon^{eff}_\alpha}{P\cdot k_c} \right) \frac{\delta_{ij}}{\sqrt{N_c}}\, \mathrm{Tr}[C[1]\Pi^\alpha_1\, \mathcal{M}_{Born}] \,\Big|_{q=0} \\ &= 2\sqrt{2}\, T^a_{ji}\, T^c_{ij}\; g_s\; \frac{1}{(P\cdot k_c)}\; \frac{\delta_{ij}}{\sqrt{N_c}}\; \mathcal{M}_{Born}\,[\,{}^3S^{[1]}_1(\epsilon_{eff})\,], \end{aligned} \tag{5.37}$$

where we have introduced the effective polarization $\epsilon^J_{eff,\alpha} \equiv \varepsilon^J_{\alpha\,\beta}\,\epsilon^\beta_c$. This is given in terms of the polarization of the soft gluon and of the quarkonium state, and it contains the dependence of the soft gluon emission on the relative direction between the gluon and $c\bar{c}$ pair.

The meaningful physical quantity is the squared amplitude summed over the final states and averaged over the initial ones. We want to express the soft P-wave amplitudes in terms of S-wave amplitudes with the help of the equation given above. But the number of degrees of freedom for S- and P-wave states are different, and we should average over the $n-1$ spatial direction of the soft gluon associated with the P-waves. After some mathematical transformations we get

$$\begin{aligned} & \int \frac{d\Omega_{n-1}}{\Omega_{n-1}} \overline{\sum_{col,pol}} |\mathcal{M}^{NLO}_{soft}\,[\,{}^3P_j^{[8]}\,]|^2 \\ = \;& N_j \frac{n-2}{n-1}\, 4C_F\, \frac{4g_s^2}{(P\cdot k_c)^2}\, \frac{1}{N_{col}N_{pol}} \overline{\sum_{col,pol}} |\mathcal{M}_{Born}\,[\,{}^3S_1^{[1]}\,]|^2. \end{aligned} \tag{5.38}$$

5.1.2 Complete NLO corrections to $\gamma\gamma \to c\bar{c}[{}^3S_1^{[1]}] + \gamma$

To obtain the real corrections we have separately integrated the corresponding MEs over the various regions of the phase space, and we have used the suitable approximations for each of them. For the ${}^3P_j^{[8]}$ channel, one can express the differential cross section as

$$\begin{aligned} d\sigma^{real}[\,{}^3P_j^{[8]}\,] \;=\; & \overline{\sum_{col,pol,j}} |\mathcal{M}^{NLO}_{soft}\,[\,{}^3P_j^{[8]}\,]|^2\, \frac{\langle \mathcal{O}_8[{}^3P_j]\rangle}{N_{col}N_{pol}} dPS_{2\to 2} \times dPS_{soft}(k_g) \\ + \; & \overline{\sum_{col,pol,j}} |\mathcal{M}^{NLO}_{hard}\,[\,{}^3P_j^{[8]}\,]|^2\, \frac{\langle \mathcal{O}_8[{}^3P_j]\rangle}{N_{col}N_{pol}} dPS^\star_{2\to 2} \times dPS^\star_{1\to 2}, \end{aligned} \tag{5.39}$$

where the notations $soft$ and $hard$ stand for an explicit multiplication of the real MEs with subsequent step functions, the expressions for the $dPS_{k\to j}$ have been discussed at the begining of the Chapter, and k_g stands for the soft-gluon momentum. The first term integrated over the soft-gluon degrees of freedom [60] gives

$$\begin{aligned} d\sigma^{soft}[\,{}^3P_j^{[8]}\,] = \frac{1}{N_{col}N_{pol}} \overline{\sum_{col,pol}} |\mathcal{M}_{Born}\,[\,{}^3S_1^{[1]}\,]|^2 \sum_j \langle \mathcal{O}_8[{}^3P_j]\rangle dPS_{2\to 2} \\ \times \frac{2\alpha_s}{3\pi m_c^2} \left(\frac{4\pi\mu^2}{m^2}\right)^\epsilon \frac{\Gamma(1-\epsilon)}{\Gamma(1-2\epsilon)} \frac{(1-\epsilon)}{(3-2\epsilon)(1-2\epsilon)} \left(-\frac{1}{\epsilon_{IR}} + \ln 4x_{cut}^2 + \frac{8m_c^2}{s_1}\ln\frac{4m_c^2}{s}\right). \end{aligned} \tag{5.40}$$

Since we have considered here only the soft contributions, they depend on the cutoff parameter. The dependence on this unphysical parameter is eliminated when soft and

hard contributions are added. We have checked this cancellation only numerically [see Fig. 6.1], because the technique used to compute the hard contribution does not allow for an analytical comparison.

Let us consider now the LO hard-scattering contribution $\gamma\gamma \to c\bar{c}[^3S_1^{[1]}] + \gamma$, for which we have implemented the radiative corrections to the operator $\langle \mathcal{O}_1[^3S_1]\rangle$. Using Eq. (2.51) we obtain

$$d\sigma^{Born}[\ ^3S_1^{[1]}\ ] = \frac{1}{N_{col}N_{pol}} \overline{\sum_{col,pol}} |\mathcal{M}_{Born}\ [\ ^3S_1^{[1]}\ ]|^2 \times \Big[\mu_\Lambda^{-2\epsilon}\langle \mathcal{O}_1[^3S_1]\rangle^{(\mu_\Lambda)} + \left(\frac{1}{\epsilon_{IR}} + \ln 4\pi - \gamma_E\right)\left(\frac{\mu}{\mu_\Lambda}\right)^{2\epsilon} \frac{2\alpha_s}{3\pi m_c^2 N_c} \sum_j \langle \mathcal{O}_8[^3P_J]\rangle\Big] dPS_{2\to 2}, \tag{5.41}$$

where μ_Λ is the NRQCD renormalization scale introduced in Section 2.3, and μ is the regularization scale. As can be easily seen, the IR-divergences cancel in the sum of soft and NRQCD corrected Born contributions:

$$\begin{aligned} d\sigma^{soft}[\ ^3P_j^{[8]}\ ] + d\sigma^{Born}[\ ^3S_1^{[1]}\ ] &= \overline{\sum_{col,pol}} |\mathcal{M}_{Born}\ [\ ^3S_1^{[1]}\ ]|^2 \frac{\mu_\Lambda^{-2\epsilon}\langle \mathcal{O}_1[^3S_1]\rangle^{(\mu_\Lambda)}}{N_{col}N_{pol}}\, dPS_{2\to 2} \\ &+ \frac{1}{N_{col}N_{pol}} \overline{\sum_{col,pol}} |\mathcal{M}_{Born}\ [\ ^3S_1^{[1]}\ ]|^2 \sum_{j=0}^{2} \langle \mathcal{O}_8(^3P_j)\rangle dPS_{2\to 2} \\ &\times \frac{2\alpha_s}{9\pi m_c^2}\left(\ln x_{cut}^2 + \frac{8m_c^2}{s_1}\ln\frac{4m_c^2}{s} - \frac{5}{3} - \ln\frac{\mu_\Lambda^2}{4m_c^2}\right). \end{aligned} \tag{5.42}$$

The complete expression for the differential NLO cross section can be written as

$$\begin{aligned} d\sigma^{NLO}(\gamma\gamma \to c\bar{c} + \gamma) &= d\sigma^{Born}[\ ^3S_1^{[1]}\ ] + \sum_{j=0}^{2} d\sigma^{soft}[\ ^3P_j^{[8]}\ ] \\ &+ d\sigma^{virt}[\ ^3S_1^{[1]}\ ] + \sum_{j=0}^{2} d\sigma^{hard}[\ ^3P_j^{[8]}\ ] + d\sigma^{real}[\ ^1S_0^{[8]}\ ], \end{aligned} \tag{5.43}$$

We have shown in this Section the exact cancellation, within the NRQCD formalism, of all types of divergences that arise at the NLO for the process $\gamma\gamma \to c\bar{c} + \gamma$. This is ,of course, a strong check for the consistency of the theory. The phenomenological consequences of the NRQCD predictions will be discussed in the next Chapter.

5.2 Real corrections to $\gamma\gamma \to c\bar{c}[n] + g$

The LO processes are:

$$\gamma\gamma \to c\bar{c}[^3S_1^{[8]}] + g,$$
$$\gamma\gamma \to c\bar{c}[^1P_0^{[8]}] + g,$$

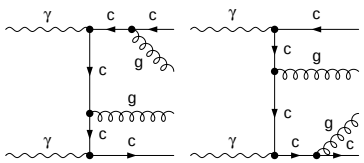

Figure 5.2: Generic Feynman diagrams for the process to $\gamma\gamma \to c\bar{c} + g + g$.

and at this level, only colour-octet final states can be produced, as has been discussed. In the processes with an additional gluon, both colour-singlet and colour-octet states can be produced, namely:

$$\begin{aligned}
&\gamma\gamma \to c\bar{c}[^1S_0^{[1,8]}] + g\ g, \\
&\gamma\gamma \to c\bar{c}[^3P_j^{[1,8]}] + g\ g \ \text{ with } \ j = 0, 1, 2, \qquad (5.44) \\
&\gamma\gamma \to c\bar{c}[^1P_1^{[8]}] + g\ g(q\bar{q}), \\
&\gamma\gamma \to c\bar{c}[^3S_1^{[8]}] + g\ g(q\bar{q}). \qquad (5.45)
\end{aligned}$$

The specific Feynman diagrams which contribute to the processes defined in Eq. (5.44) are shown in Fig. 5.2. They are very similar to the diagrams contributing to the processes $\gamma\gamma \to c\bar{c}[n] + \gamma + g$. The replacement of the final photon with a gluon translates only into a change of couplings and colour factors. Therefore, for these processes we use a similar technique as that described in the last subsection.

For the second set of processes, defined in Eq. (5.45), the generic Feynman diagrams are shown in Fig. 5.3. They contain the splitting of a gluon into either two gluons or into a light-quark and anti-quark pair. Due to our choice for the sum over the gluon polarization we should also introduce Fadeev-Popov ghosts. We study separately the two sets of processes because they require different techniques for the integration over the unknown degrees of freedom.

Note that the colour-singlet $^3S_1$ state cannot be produced in these processes. The Feynman diagrams shown in Fig. 5.2 do not contribute due to their Dirac structure (the sum of all of them vanishes) and those shown in Fig. 5.3 do not contribute due to their colour structure. We conclude that the processes $\gamma\gamma \to c\bar{c}[n] + g$ are colour suppressed, but enhanced by the ratio α_s/α relative to the process $\gamma\gamma \to c\bar{c}[n] + \gamma$.

The channel containing $c\bar{c}[^1P_0^{[8]}]$ in the final state is not studied here due to our expectation, on the basis of the velocity-scaling rules, that they do not produce measurable effects.

The partonic cross section for the process $\gamma\gamma \to c\bar{c}[n] + gg(q\bar{q})$ can be written as

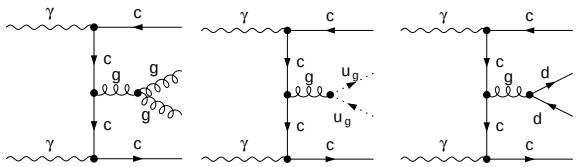

Figure 5.3: Generic Feynman diagrams for the process to $\gamma\gamma \to c\bar{c}[^3S_1^{[8]}] + g + g$.

$$
\begin{aligned}
& d\sigma^{real}(\gamma\gamma \to c\bar{c}[n] + gg(q\bar{q})) \\
= \;& \frac{1}{2!}\overline{\sum}_{col,pol,m_j} |\mathcal{M}^{gg}_{real}\,[^3P_j^{[8]}]|^2\, \frac{\langle \mathcal{O}_8[^3P_j]\rangle}{N_{col}N_{pol}} dPS_{2\to 3} \\
+ \;& \frac{1}{2!}\overline{\sum}_{col,pol,m_j} |\mathcal{M}^{gg}_{real}\,[^3P_j^{[1]}]|^2\, \frac{\langle \mathcal{O}_1[^3P_j]\rangle}{N_{col}N_{pol}} dPS_{2\to 3} \\
+ \;& \frac{1}{2!}\overline{\sum}_{col,pol} |\mathcal{M}^{gg}_{real}\,[^1S_0^{[8]}]|^2\, \frac{\langle \mathcal{O}_8[^1S_0]\rangle}{N_{col}N_{pol}} dPS_{2\to 3} \\
+ \;& \frac{1}{2!}\overline{\sum}_{col,pol} |\mathcal{M}^{gg}_{real}\,[^1S_0^{[1]}]|^2\, \frac{\langle \mathcal{O}_1[^1S_0]\rangle}{N_{col}N_{pol}} dPS_{2\to 3} \\
+ \;& \frac{1}{2!}\overline{\sum}_{col,pol} |\mathcal{M}^{gg}_{real}\,[^3S_1^{[8]}]|^2\, \frac{\langle \mathcal{O}_8[^3S_1]\rangle}{N_{col}N_{pol}} dPS_{2\to 3} \\
+ \;& n_{lf}\overline{\sum}_{col,pol} |\mathcal{M}^{q\bar{q}}_{real}\,[^3S_1^{[8]}]|^2\, \frac{\langle \mathcal{O}_8[^3S_1]\rangle}{N_{col}N_{pol}} dPS_{2\to 3}, \qquad (5.46)
\end{aligned}
$$

where $n_{lf} = 3$ is the number of the light-quark active flavours and the factor 1/2! is introduced for processes with two identical particles [*i.e.* two gluons] in the final states. Note that the contributions from colour-singlet $^1S_0$ and ^3P_j do not vanish, but the long-distance OMEs corresponding to the J/Ψ-meson are very small [they are suppressed by v^8 according to the velocity-scaling rules], and we neglet them in our numerical analysis. Although, we study their IR-limit in order to demonstrate the cancellation of all divergences.

If one of the two gluons becomes soft, then the MEs are plagued by the IR-divergences of soft origin. If the two gluons or light quark and anti-quark are emitted collinearly, then mass- or collinear-singularities occur. If one gluon is soft and is emitted collinear to the other, then soft-collinear singularities arise. To extract the IR-divergences from the real MEs we use the parameterization of the phase space given in the first Section. The individual limits are discussed in the next Section and, in Section 5.2.3, we present the complete NLO corrections to $\gamma\gamma \to c\bar{c}[n] + g$.

5.2.1 Soft-collinear limit of $\gamma\gamma \to c\bar{c}[^3S_1^{[1,8]}] + gg$

For the soft gluon emission we used the same technique as in Section 5.1.1 and we chose the same CMS as that described in Eq. (5.3). The soft MEs factorize with an eikonal factor and Born MEs as expected:

$$\lim_{k_3\to 0} \mathcal{M}^{gg}_{NLO}\,[^3S_1^{[8]}] = -ig_s\,\frac{f_{abc}\sqrt{2}}{4}\left(\frac{P\cdot\epsilon_c}{P\cdot k_3} - \frac{k_4\cdot\epsilon_c}{k_4\cdot k_3}\right)\mathcal{M}^{g}_{Born}\,[^3S_1^{[8]}], \tag{5.47}$$

where ϵ_c is the polarization vector of the soft gluon. For the squared matrix elements we get

$$\begin{aligned}\lim_{k_3\to 0} |\mathcal{M}^{gg}_{NLO}\,[^3S_1^{[8]}]|^2 &= g_s^2\,\frac{f_{abc}^2}{8}\left(\frac{2\;P\cdot k_4}{(P\cdot k_3)(k_4\cdot k_3)} - \frac{4m_c^2}{(P\cdot k_3)^2}\right)|\mathcal{M}^{g}_{Born}\,[^3S_1^{[8]}]|^2 \\ &= 4\;C_A\;g_s^2\left(\frac{s_4}{s_3\;s_5} - \frac{4m_c^2}{s_5^2}\right)|\mathcal{M}^{g}_{Born}\,[^3S_1^{[8]}]|^2. \end{aligned}\tag{5.48}$$

Similarly for the limit $k_4 \to 0$ we have

$$\lim_{k_4\to 0} |\mathcal{M}^{gg}_{NLO}\,[^3S_1^{[8]}]|^2 = 4\;C_A\;g_s^2\left(\frac{s_5}{s_3\;s_4} - \frac{4m_c^2}{s_4^2}\right)|\mathcal{M}^{g}_{Born}\,[^3S_1^{[8]}]|^2. \tag{5.49}$$

To obtain the collinear limit (defined as $\theta_{34} \to 0$) of the MEs we work in the same CMS as for the soft limit. The MEs contain terms that factorize either with $1/s_3$ or $1/s_3^2$. In the parameterization of the collinear PS a factor $2/s_3 = 1/(k_3\cdot k_4)$ was already included. The integration over θ_{34} of terms like θ_{34}^k/s_3 only gives contributions of the order $\mathcal{O}(x_{cut})$ that vanish in the limit $x_{cut} \to 0$. Accordingly, all invariants in the expressions multiplying the $1/s_3$ propagator can be replaced with their values at $\theta_{34} = 0$.
The expressions multiplying $1/s_3^2$ have to be expanded up to order $\mathcal{O}(\theta_{34}^2)$. The resulting contributions after the power expansion behave as follows:

- terms like $1/s_3^2$ cancel, as expected from gauge invariance.
- terms like $\sin\theta_{34}/s_3^2$ are always multiplied with $\cos\phi$ and they vanish after azimuthal integration.
- terms like θ_{34}^2/s_3^2 finally contribute to the collinear MEs.

After explicit calculation we obtain:

$$\begin{aligned}&\lim_{k_3\parallel k_4}\int d\phi\,\frac{1}{2}\,|\mathcal{M}^{gg}_{NLO}\,[^3S_1^{[8]}]|^2 \\ &= B\left(\frac{1}{2};\frac{n-3}{2}\right)\,\frac{1}{s_3}\,g_s^2\,2C_A\,\frac{1}{6}P_{gg}(z)\,|\mathcal{M}^{g}_{Born}\,[^3S_1^{[8]}]|^2 + \mathcal{O}(\theta_{34}),\end{aligned}\tag{5.50}$$

where $B(a,b)$ is the Beta-function, given in App. D, and P_{gg} is the Altarelli-Parisi gluon splitting function into two gluons [58], given by:

$$P_{gg}(z) = 2C_A \left[\frac{z}{1-z} + \frac{1-z}{z} + z(1-z) \right], \tag{5.51}$$

where z has been defined in Eq. (5.20). We can also express the gluon splitting functions in terms of Lorentz invariants. Such a parameterization is not unique, but we should choose the (only) parameterization that in the soft-collinear region (*i.e.* $z \to 0$, $\theta_{34} \to 0$) reproduces the eikonal factors

$$P_{gg}(z) = 2C_A \left[\frac{s_4}{s_3\ s_5} + \frac{s_5}{s_3\ s_4} + \frac{s_4 s_5}{s_3(s_4+s_5)^2} \right]. \tag{5.52}$$

Now, we can construct an eikonal factor valid for the whole IR-region, and which reproduces the specific soft and collinear behaviours in the subsequent limits

$$\mathcal{F}_{gg} = 4C_A\ g_s^2 \left[\frac{s_4}{s_3\ s_5} + \frac{s_5}{s_3\ s_4} + \frac{s_4 s_5}{s_3(s_4+s_5)^2} - \frac{4m_c^2}{s_4^2} - \frac{4m_c^2}{s_5^2} \right]. \tag{5.53}$$

It is easy to check that the term $\frac{s_4 s_5}{(s_4+s_5)^2}$ does not contribute in the soft limit and terms like $\frac{4m_c^2}{s_4^2}$ do not contribute in the collinear limit. This Lorentz-invariant expression for the soft-collinear limit of the real MEs has the advantage that the integration over the degrees of freedom of the final unobserved particles can be performed in any suitable CMS. We have chosen the CMS given in Eq. (5.3), with the discussed parameterization of the phase space. For the differential partonic cross section in the soft-limit, we obtain

$$\begin{aligned} d\sigma^{gg}_{soft}[^3S_1^{[8]}]] &= \overline{\sum}_{col,pol} |\mathcal{M}^g_{Born}\ [^3S_1^{[8]}]|^2\ dPS_{2\to 2} \times \frac{1}{2}\int \mathcal{F}_{gg}(dPS_{soft}(3) + dPS_{soft}(4)) \\ &\equiv I^{gg}_{soft}\ d\sigma_{Born}[^3S_1^{[8]}], \end{aligned} \tag{5.54}$$

where the expression for I^{gg}_{soft} is given by:

$$\begin{aligned} I^{gg}_{soft} \equiv \frac{1}{2}\int\ \mathcal{F}_{gg} \Bigg(& \frac{\mu^{(4-n)}}{(2\pi)^{n-1}} \frac{\omega_3^{n-2}}{2\omega_3} d\omega_3\ \sin^{n-3}\theta_3\ d\theta_3\ d\Omega_{n-2}\ \Theta(x_{cut} - x_g^{(3)}) \\ & + \frac{\mu^{(4-n)}}{(2\pi)^{n-1}} \frac{\omega_4^{n-2}}{2\omega_4} d\omega_4\ \sin^{n-3}\theta_4\ d\theta_4\ d\Omega_{n-2}\ \Theta(x_{cut} - x_g^{(4)}) \Bigg). \end{aligned} \tag{5.55}$$

The explicit form of the result after this integration [60] is

$$\begin{aligned} I^{gg}_{soft} &= \left(\frac{4\pi\mu^2}{m_c^2}\right)^{\epsilon} \frac{g_s^2}{(4\pi)^2}\ 2C_A \left[\frac{1}{\epsilon^2} + \frac{1}{\epsilon} \left(1 + \ln\frac{4m_c^4}{s^2 x_{cut}^2} \right) + \frac{1}{2}\ln^2\frac{x_{cut}^2 s}{m_c^2} + \left(1 + \ln\frac{4m_c^2}{s} \right) \right. \\ & \left. \ln\frac{m_c^2}{x_{cut}^2 s} + \frac{1}{2}\ln^2\frac{4m_c^2}{s} + 2\ \mathrm{Li}_2\left(-\frac{s_1}{4m_c^2}\right) - \frac{\pi^2}{3} - \frac{s+4m_c^2}{s-4m_c^2}\ \ln\frac{4m_c^2}{s} \right]. \end{aligned} \tag{5.56}$$

For the collinear contribution we define similarly the partonic differential cross section

$$\begin{aligned} d\sigma^{gg}_{coll}[^3S_1^{[8]}]] &= \overline{\sum}_{col,pol} |\mathcal{M}^g_{Born}\ [^3S_1^{[8]}]|^2\ dPS_{2\to 2} \times \frac{1}{2}\int \mathcal{F}_{gg} dPS_{coll}(3,4) \\ &\equiv I^{gg}_{coll}\ d\sigma_{Born}[^3S_1^{[8]}], \end{aligned} \tag{5.57}$$

where I^{gg}_{coll} is defined as

$$\begin{aligned} I^{gg}_{coll} &\equiv \frac{1}{2}\int\ \mathcal{F}_{gg}\frac{\mu^{(4-n)}}{(2\pi)^{n-1}}\ [(1-z)z(\omega_3+\omega_4)]^{(n-4)}\ dz\frac{(1-y^2)^{\frac{n-4}{2}}}{(1-y)}\ dy\ d\Omega_{n-2} \\ &\times\ \Theta(1-z-z_{cut})\ \Theta(x_{cut}-(1-y)). \end{aligned} \tag{5.58}$$

In the collinear limit, the energy sum of the two emitted gluons is given by

$$\omega_3+\omega_4 = s_1/(2\sqrt{s}) + \mathcal{O}(\theta_{34}), \tag{5.59}$$

and the mathematical expression for the above integral becomes

$$\begin{aligned} I^{gg}_{coll} &= \left(\frac{4\pi\mu^2}{m_c^2}\right)^{\epsilon}\ \frac{g_s^2}{(4\pi)^2}\ 2C_A \\ &\left[\frac{1}{\epsilon}\left(\frac{11}{6}+2\ln\frac{x_{cut}s}{s1}\right) - 2\ln\frac{x_{cut}s}{s1}\ \ln\frac{x_{cut}^2 s_1}{2m_c^2} - \frac{11}{6}\ln\frac{x_{cut}s_1^2}{2m_c^2\ s} - \frac{2\pi^2}{3} + \frac{67}{9}\right]. \end{aligned} \tag{5.60}$$

The complete contribution of the IR-region is defined as the sum of the soft and collinear terms

$$\begin{aligned} d\sigma^{gg}_{IR}[^3S_1^{[8]}]] &= d\sigma^{gg}_{soft}[^3S_1^{[8]}]] + d\sigma^{gg}_{coll}[^3S_1^{[8]}]] \\ &= (I^{gg}_{soft} + I^{gg}_{coll})\ \times\ d\sigma_{Born}[^3S_1^{[8]}]. \end{aligned} \tag{5.61}$$

The IR-divergent pieces of the $d\sigma^{gg}_{IR}$ are contained only in the $(I^{gg}_{soft}+I^{gg}_{coll})$ factor since the Born MEs are finite:

$$\begin{aligned} d\sigma^{gg}_{IR-div}[^3S_1^{[8]}]] &= \left(\frac{4\pi\mu^2}{m_c^2}\right)^{\epsilon}\ \frac{g_s^2}{(4\pi)^2}\ 2C_A\ \left[\ \frac{1}{\epsilon^2}+\frac{1}{\epsilon}\ \left(\ 1+\frac{11}{6}-2\ \ln\frac{s_1}{2m_c^2}\ \right)\ \right] \\ &\times\ d\sigma_{Born}[^3S_1^{[8]}]. \end{aligned} \tag{5.62}$$

In the study of the virtual corrections [see Eqs (4.35), (4.36), (4.37)], it turned out that there remained uncanceled IR-singularities. These are exactly canceled by the singularities contained in the above formula, up to the term proportional to n_{lf}, which is studied in the next subsection. The expression in Eq. (5.61) contains an explicit dependence on the cut-off parameter x_{cut}. This dependence cancels out when the soft and the collinear contributions are added to the hard contributions. We have not analytically integrated the hard MEs, because they have very large expressions. The angular integration was done numerically and the dependence on the cut-off parameter explicitly extracted [see Fig. 6.6].

5.2.2 Infra-red limit of the process $\gamma\gamma \to c\bar{c}[^3S_1^{[8]}] + q\bar{q}$

Our detailed analysis has shown that the MEs for this process contain only collinear-divergences. Accordingly, we expect only single poles to arise after the integration over the collinear phase space. Using a similar method as for the subprocess with two gluons in the final state, we obtain for the collinear limit of the MEs:

$$\begin{aligned} & \lim_{k_3 \| k_4} \int d\phi \, |\mathcal{M}^{q\bar{q}}_{NLO} \, [^3S_1^{[8]}]|^2 \\ = \;& B\left(\frac{1}{2}; \frac{n-3}{2}\right) \, \frac{1}{s_3} \, g_s^2 \, 2 \, P_{qg}(z) \, |\mathcal{M}^{g}_{Born} \, [^3S_1^{[8]}]|^2 + \mathcal{O}(\theta_{34}), \end{aligned} \tag{5.63}$$

where $P_{qg}(z)$ is the Altarelli-Parisi gluon splitting function into quark and anti-quark pair [58], and it is given by

$$P_{qg}(z) = T_F \, \frac{1}{1-\epsilon} \, \left[\, z^2 + (1-z)^2 - \epsilon \, \right], \tag{5.64}$$

where z is the fraction of energy carried by the splitting products. We can parameterize this splitting function also in terms of Lorentz-invariant quantities as

$$P_{qg}(z) = T_F \, \frac{1}{1-\epsilon} \, \left[\, \left(\frac{s_4}{s_1}\right)^2 + \left(\frac{s_5}{s_1}\right)^2 - \epsilon \, \right]. \tag{5.65}$$

The advantage of such a formulation is that it is CMS independent .

For this process the corresponding eikonal factor $\mathcal{F}_{qg}$ is identical to the Altarelli-Parisi splitting function P_{qg}, and we can use the parameterization given in Eq. (5.65) over the complete IR-region. The integration over the light-partons degrees of freedom can be done easily in the same CMS as before.

We define similarly the partonic differential cross section for the IR-region as

$$\begin{aligned} d\sigma^{q\bar{q}}_{coll}[^3S_1^{[8]}]] \;&=\; n_{lf} \, \overline{\sum}_{col,pol} \, |\mathcal{M}^{g}_{Born} \, [^3S_1^{[8]}]|^2 \, dPS_{2\to 2} \times 2 \int \mathcal{F}_{gg} dPS_{coll}(3,4) \\ &\equiv\; I^{q\bar{q}}_{coll} \, d\sigma_{Born}[^3S_1^{[8]}], \end{aligned} \tag{5.66}$$

where $I^{q\bar{q}}_{coll}$ is given by

$$\begin{aligned} I^{q\bar{q}}_{coll} \;&\equiv\; \int \mathcal{F}_{q\bar{q}} \frac{\mu^{(4-n)}}{(2\pi)^{n-1}} \, [(1-z)z(\omega_3+\omega_4)]^{(n-4)} \, dz \frac{(1-y^2)^{\frac{n-4}{2}}}{(1-y)} \, dy \, d\Omega_{n-2} \\ &\times\; \Theta(1-z-z_{cut}) \, \Theta(x_{cut} - (1-y)). \end{aligned} \tag{5.67}$$

Its explicit analytical form is

$$I^{q\bar{q}}_{coll} = \left(\frac{4\pi\mu^2}{m_c^2}\right)^{\epsilon} \, \frac{g_s^2}{(4\pi)^2} \, \left[\, -\frac{2}{3}\frac{1}{\epsilon} - \frac{23}{9} + \frac{2}{3} \, \ln\frac{x_{cut} s_1}{4m_c^2} + \frac{2}{3} \, \ln\frac{2s_1}{s} \, \right]. \tag{5.68}$$

It is easy to extract now the IR-divergent part contained in $d\sigma^{q\bar{q}}_{coll}[^3S_1^{[8]}]$:

$$d\sigma^{q\bar{q}}_{IR-div}[^3S_1^{[8]}] = \left(\frac{4\pi\mu^2}{m_c^2}\right)^{\epsilon} \frac{g_s^2}{(4\pi)^2} n_{lf} \left(-\frac{2}{3}\frac{1}{\epsilon_{IR}}\right). \tag{5.69}$$

This term is proportional with $n_{lf} = 3$ (the number of active flavours in our calculations), and it will exactly cancel the divergent piece from the virtual contributions in Eq. (4.37) that is dependent on the n_{lf}.

5.2.3 Complete NLO corrections to $\gamma\gamma \to c\bar{c}[^3S_1^{[8]}] + g$

If we consider now the full NLO analysis of the process $\gamma\gamma \to c\bar{c}[^3S_1^{[8]}] + g$ and ignore for the moment the radiative corrections at the same order in α_s to the NRQCD operators, we can probe the missing IR-singularity cancellation and obtain the NLO partonic differential cross section as a finite quantity

$$d\sigma^{NLO}[^3S_1^{[8]}] = d\sigma^{Born}[^3S_1^{[8]}] + d\sigma^{virt}[^3S_1^{[8]}] + d\sigma^{IR}[^3S_1^{[8]}] + d\sigma^{hard}[^3S_1^{[8]}]. \tag{5.70}$$

The meaningful physical quantity for the NLO cross section should also contain order α_s corrections to the operator $\langle \mathcal{O}[^3S_1^{[8]}]\rangle$. As discussed in Chapter 2, the NLO operator suffers from IR-divergences. They will be canceled when we add also contributions produced in the first set of processes defined in Eq. (5.44). The analysis of these processes is very similar with that already done for the process $\gamma\gamma \to c\bar{c}[n] + \gamma g$. In the process with two gluons in the final states we can produce both colour-singlet and colour-octet $^1S_0$ and ^3P_j states, with $j = 0, 1, 2$. Again, the real MEs for the processes $\gamma\gamma \to c\bar{c}[^1S_0^{[1,8]}] + gg$ are finite over the complete phase space, and they vanish in the IR-limit. The MEs for the processes $\gamma\gamma \to c\bar{c}[^3Pj^{[1,8]}] + gg$ suffer from soft and collinear divergences. Following the same steps as in Section 5.1.2, we can extract the IR-divergent pieces from the soft differential cross section for the colour-octet P-wave states as

$$\begin{aligned} d\sigma^{soft}_{IR-div}[\ ^3P_j^{[8]}\ ] = \frac{1}{N_{col}N_{pol}} \overline{\sum_{col,pol}} |\mathcal{M}_{Born}\ [\ ^3S_1^{[1]}\ ]|^2 \sum_{j=0}^{2} B_F \langle \mathcal{O}_8[^3P_j]\rangle dPS_{2\to 2} \\ \times \frac{4\alpha_s}{\pi m_c^2} \left(\frac{4\pi\mu^2}{m^2}\right)^{\epsilon} \frac{\Gamma(1-\epsilon)}{\Gamma(1-2\epsilon)} \frac{(1-\epsilon)}{(3-2\epsilon)(1-2\epsilon)} \left(-\frac{1}{\epsilon_{IR}}\right), \end{aligned} \tag{5.71}$$

and for the colour-singlet states

$$\begin{aligned} d\sigma^{soft}_{IR-div}[\ ^3P_j^{[1]}\ ] = \frac{1}{N_{col}N_{pol}} \overline{\sum_{col,pol}} |\mathcal{M}_{Born}\ [\ ^3S_1^{[1]}\ ]|^2 \sum_{j=0}^{2} C_F \langle \mathcal{O}_8[^3P_j]\rangle dPS_{2\to 2} \\ \times \frac{4\alpha_s}{\pi m_c^2} \left(\frac{4\pi\mu^2}{m^2}\right)^{\epsilon} \frac{\Gamma(1-\epsilon)}{\Gamma(1-2\epsilon)} \frac{(1-\epsilon)}{(3-2\epsilon)(1-2\epsilon)} \left(-\frac{1}{\epsilon_{IR}}\right), \end{aligned} \tag{5.72}$$

where the colour coefficients B_F and C_F are given in App. A.
If we recall Eq. (2.50) where the NLO corrections for $\langle \mathcal{O}_8[^3S_1]\rangle$ are given, one can write the NRQCD corrected Born contribution as follows:

$$\begin{aligned} d\sigma^{Born}[\ ^3S_1^{[8]}\ ] &= \frac{1}{N_{col}N_{pol}}\overline{\sum_{col,pol}}|\mathcal{M}_{Born}\ [\ ^3S_1^{[1]}\ ]|^2 \\ &\times\Big[\mu_\Lambda^{-2\epsilon}\langle\mathcal{O}_8[^3S_1]\rangle^{(\mu_\Lambda)} + \left(\frac{1}{\epsilon_{IR}} + \ln 4\pi - \gamma_E\right)\left(\frac{\mu}{\mu_\Lambda}\right)^{2\epsilon} \\ &\times\frac{4\alpha_s}{3\pi M^2}\Big[CF\sum_j\langle\mathcal{O}_1[^3P_J]\rangle + BF\sum_j\langle\mathcal{O}_8[^3P_J]\rangle\Big]\Big]dPS_{2\to2}. \quad (5.73) \end{aligned}$$

If we add the last three equations we can easily see the cancellation of the IR-divergences, and that there is a finite reminder, which depends on the NRQCD renormalization scale μ_Λ

$$\begin{aligned} & d\sigma^{soft}_{IR-div}[\ ^3P_j^{[8]}\ ] + \sigma^{soft}_{IR-div}[\ ^3P_j^{[1]}\ ] + d\sigma^{Born}[\ ^3S_1^{[1]}\ ] \\ = & \overline{\sum_{col,pol}}|\mathcal{M}_{Born}\ [\ ^3S_1^{[8]}\ ]|^2\frac{\mu_\Lambda^{-2\epsilon}\langle\mathcal{O}_1[^3S_1]\rangle^{(\mu_\Lambda)}}{N_{col}N_{pol}}\ dPS_{2\to2} \\ + & \frac{1}{N_{col}N_{pol}}\overline{\sum_{col,pol}}|\mathcal{M}_{Born}\ [\ ^3S_1^{[8]}\ ]|^2\ \sum_{j=0}^{2}\Big(B_F\langle\mathcal{O}_8[^3P_j]\rangle + C_F\langle 6\mathcal{O}_1[^3P_j]\rangle\Big)\ dPS_{2\to2} \\ \times & \frac{4\alpha_s}{3\pi m_c^2}\left(-\frac{5}{3} - \ln\frac{\mu_\Lambda^2}{4m_c^2}\right). \quad (5.74) \end{aligned}$$

The full NLO differential cross section for the process $\gamma\gamma \to c\bar{c}[^3S_1^{[8]}] + g$ is then given by

$$\begin{aligned} d\sigma^{NLO}(\gamma\gamma\to c\bar{c}+g) &= d\sigma^{NLO}[\ ^3S_1^{[8]}\ ] \\ &+ \sum_{j=0}^{2}d\sigma^{real}[\ ^3P_j^{[8]}\ ] + \sum_{j=0}^{2}d\sigma^{real}[\ ^3P_j^{[1]}\ ] \\ &+ d\sigma^{real}[\ ^1S_0^{[8]}\ ] + d\sigma^{real}[\ ^1S_0^{[1]}\ ], \quad (5.75) \end{aligned}$$

where $d\sigma^{NLO}[\ ^3S_1^{[8]}\ ]$ has been defined in Eq. (5.70), and it is a finite quantity. We conclude that NRQCD provides a consistent theory to systematically include all allowed LO and NLO processes. Within this framework, we have proven the complete cancellation of all types of divergences. The leftover finite contributions are NRQCD renormalization scale dependent, and in our numerical analysis we have fixed the NRQCD renormalization scale to $\mu_\Lambda = M_{J/\Psi} = 2m_c$. In the next Chapter we will use the results obtained in this Section in order to perform a numerical analysis of the processes $\gamma\gamma \to c\bar{c}[n] + \gamma$ and $\gamma\gamma \to c\bar{c}[n] + g$.

Chapter 6

Numerical analysis

We are now in a position to explore the phenomenological implications of our theoretical results. We wish to analyze in detail the NLO corrections to the hadronic cross section of the process $e^+e^- \to e^+e^- J/\psi + X$, where $X = g, \gamma$, considering only the direct channel and using the theoretical prescriptions given the last two chapters. For exclusive measurements of J/Ψ-particles with two jets, we impose additional cuts as required by the experimental procedure.

For both types of analysis we have chosen the same input parameters as in Chapter 3, *i.e.* $m_c = 1.5$ GeV, $\alpha = 1/137.036$, and α_s from the LO formula taking $n_{lf} = 3$ active light-quark flavours and the renormalization scale $\mu = \xi_\mu m_T$ with the default value $\xi_\mu = 1$. For the default operator matrix elements $\langle \mathcal{O}^H \rangle$, we have adopted the set determined in Ref. [13] by fitting the Tevatron data Ref. [6], using the LO proton PDFs from Martin-Roberts-Stirling-Throne (MRST98LO). We have employed $\Lambda^{(3)}_{QCD} = 204$ MeV, which corresponds to $\Lambda^{(4)}_{QCD} = 174$ MeV, to conform with the fit in Ref. [13].

6.1 NLO analysis of the process $\gamma\gamma \to J/\Psi + \gamma$

As we discussed in the previous Chapter, we have used the *phase space slicing method* to integrate out the degrees of freedom of the two light outgoing particles. After the decomposition of the phase space into soft, collinear and hard parts, the individual partonic cross sections are cut-off dependent, and only their sum should be independent of this unphysical parameter. In the process $\gamma\gamma \to c\bar{c}[n] + \gamma + g$, the $c\bar{c}$ pair can be produced only in the ${}^3P_j^{[8]}$ and ${}^1S_0^{[8]}$ states.

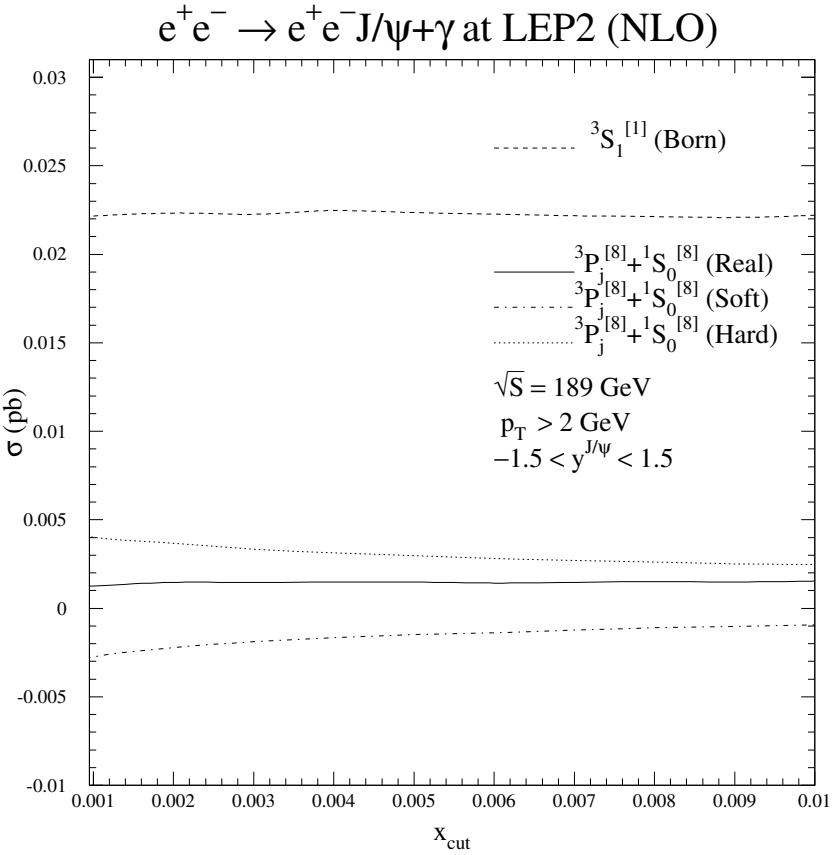

Figure 6.1: The cut-off independence of the total cross section for the process $\gamma\gamma \to c\bar{c}[n] + \gamma$ via bremsstrahlung at LEP2.

In Fig. 6.1 we show the cut-off independence of the total cross section, considered as a real correction, for a cut-off variation from 10^{-3} to 10^{-2}. To obtain the total cross section we have integrated over the J/Ψ-rapidity from -1.5 to 1.5 and over transverse momenta above 2 GeV. As can be seen from the figure, the real corrections are almost an order of magnitude smaller than the Born contributions. This is caused by the colour suppression of the octet states relative to singlet one. We have investigated a wider range for the cut-off parameter and it turned out that at smaller values $10^{-6} - 10^{-4}$ the numerical instabilities are rather large, while at larger values $10^{-2} - 10^{-1}$ the eikonal approximation is no longer valid and the total cross section depends on the cut-off. We have chosen for our analysis a cut-off parameter in the range $10^{-3} - 10^{-2}$ where the total cross section is independent of this arbitrary parameter.

In Fig. 6.2 we show the transverse momentum distribution of the hadronic cross sec-

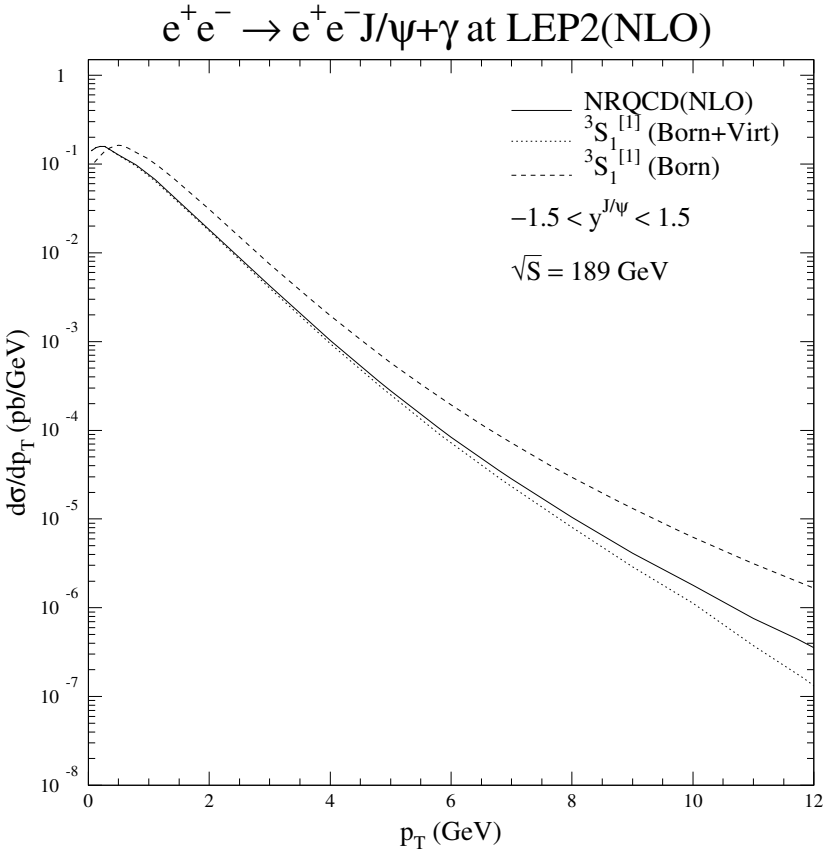

Figure 6.2: The transverse momentum distribution $d\sigma/dp_T$ of $\gamma\gamma \to c\bar{c}[n] + \gamma$ via bremsstrahlung at LEP2.

tion. The dashed lines represent the Born contribution, the dotted lines correspond to Born+virtual corrections, and the full lines to the NLO NRQCD predictions, where also real corrections from ${}^3P_j^{[8]}$ and ${}^1S_0^{[8]}$ states have been included. We can conclude from this figure that the virtual corrections are large ($\sim 30\%$) and negative. The sum Born+virtual is a pure CSM computation. It is finite and for large values of the transverse momenta p_T it can become negative, which is a signal of theoretical inconsistencies. The real corrections become important at large transverse momenta and the slope of their curve is flatter than the Born+virtual contribution.

In Fig. 6.3 we investigate the rapidity distributions $d\sigma/dy_{J/\Psi}$ for $\gamma\gamma \to c\bar{c}[{}^3S_1^{[1]}] + \gamma$. The dotted lines correspond to Born+virtual corrections and the dashed lines to Born contributions. The solid lines refer to the sum of Born and NLO corrections allowed in NRQCD. The y distributions displayed in Fig. 6.3 are all symmetric about $y = 0$ with

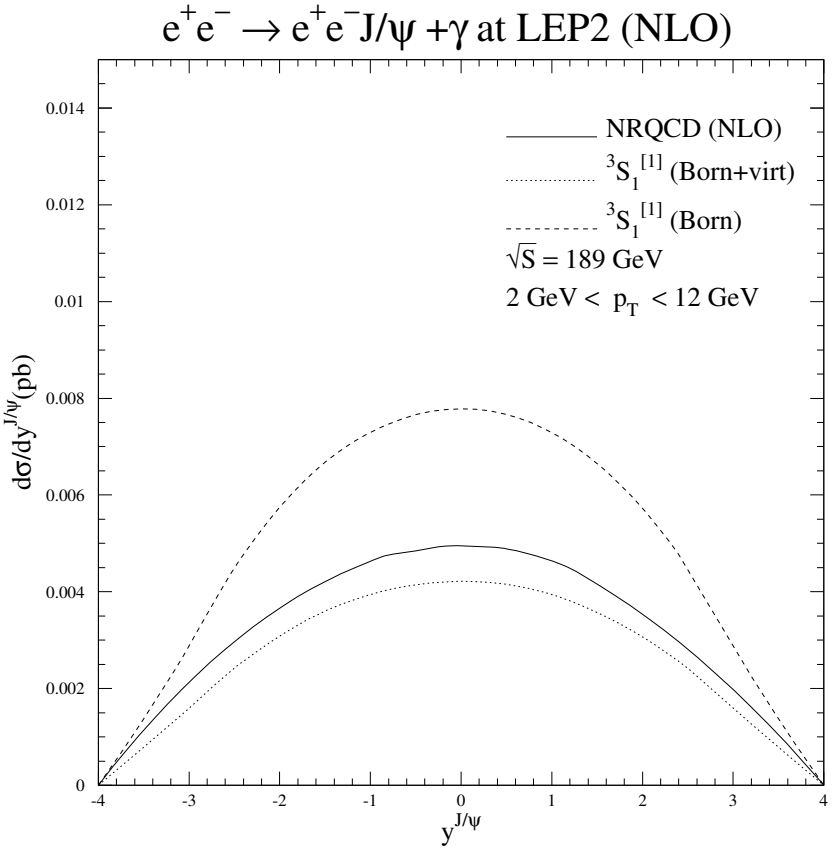

Figure 6.3: Rapidity distribution $d\sigma/dy_{J/\Psi}$ of $\gamma\gamma \to c\bar{c}[n] + g$ via bremsstrahlung at LEP2, considering LO and NLO contributions.

a maximum at this rapidity value. We can explain this by our assumption that electron and positron beams have similar set-up. LO and NLO have similar dependence on the rapidity, which can be explained by the fact that the Feynman graphs have equivalent topologies.

In Fig 6.4 we compare the scale dependence of the LO and NLO differential cross sections $d\sigma/dp_T$ for $p_T = 2$ GeV. The LO contribution is a QED process and therefore independent of the renormalization scale (dashed lines). At NLO an additional gluon is present in the Feynman graphs and a scale dependence is introduced. Since in our computation we have used for this process the *on-shell* scheme to renormalize the heavy-quark mass, the scale dependence is only introduced with the strong coupling constant. The μ-independence of the quantity $1/\alpha_s d\sigma_{virt}$ was checked explicitly. For the real contributions, the scale dependence is introduced again by the running α_s. The different contributions

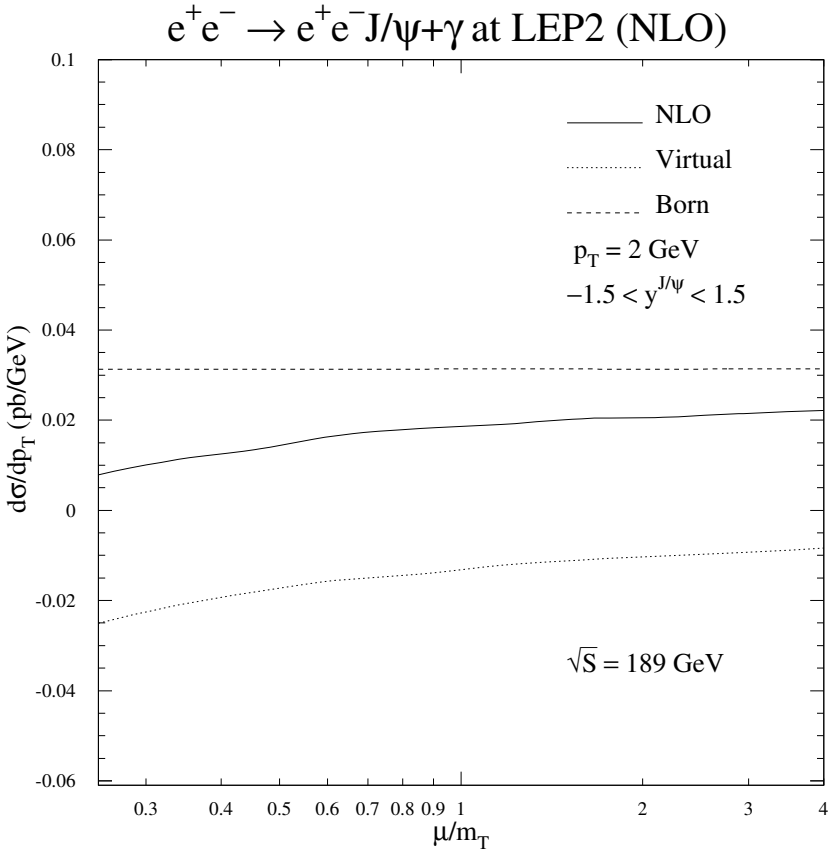

Figure 6.4: The scale dependence of the total cross section of $\gamma\gamma \to c\bar{c}[n] + \gamma$ via bremsstrahlung at LEP2.

are plotted with the same types of lines as before, except the dotted lines which encounter now only the virtual contributions. We can conclude that at small energy scales, perturbation theory breaks down due to the large increase of α_s. In contrast, at large scales the results have a smooth dependence on the scale.

In Fig. 6.5 we show the dependence of the total cross section σ on the center-of-mass e^+e^- energy. It can be seen that there is an increase by a factor of two from LEP2 to TESLA2 energies both at LO and NLO.

The conclusions of the NLO analysis of the process $\gamma\gamma \to c\bar{c}[n] + \gamma$ are that the overall normalization is decreased by almost 30% and that the slope of the dependence of $d\sigma/dp_T$ on the transverse momenta p_T is increased at NLO order.

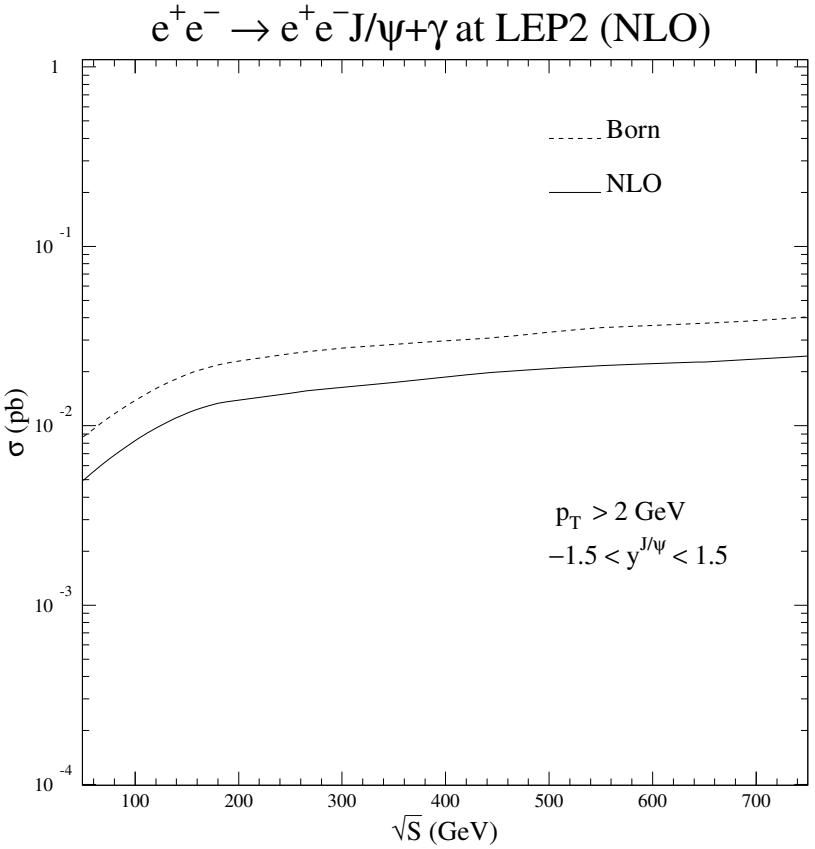

Figure 6.5: The center-of-mass energy distribution of the total cross section for $\gamma\gamma \to c\bar{c}[n] + \gamma$ via bremsstrahlung at LEP2.

6.2 NLO analysis of the process $\gamma\gamma \to J/\Psi + g$

We now consider the NLO analysis of the process $\gamma\gamma \to c\bar{c}[n] + g$. We start with a discussion about the phase space slicing method applied to the individual channels. Namely, we have separately analyzed the ${}^3S_1^{[8]}$ and ${}^3P_j^{[8]} + {}^1S_0^{[8]}$ channels because they get contributions from different types of Feynman diagrams and they have different IR-divergent behaviour, as explained in Section 5.2.

Let us start with the analysis of $\gamma\gamma \to c\bar{c}[{}^3S_1^{[8]}] + g$. We show in Fig. 6.6 the independence of the total cross section on the unphysical cut-off parameter x_{cut}. We have plotted the Born contribution with dashed lines, the *hard* contribution with dotted lines, the *soft* contribution with dot-dashed lines, and the sum *hard+soft*, arising in the real contribution, with solid lines. As we can see in the figure the real cross section does not

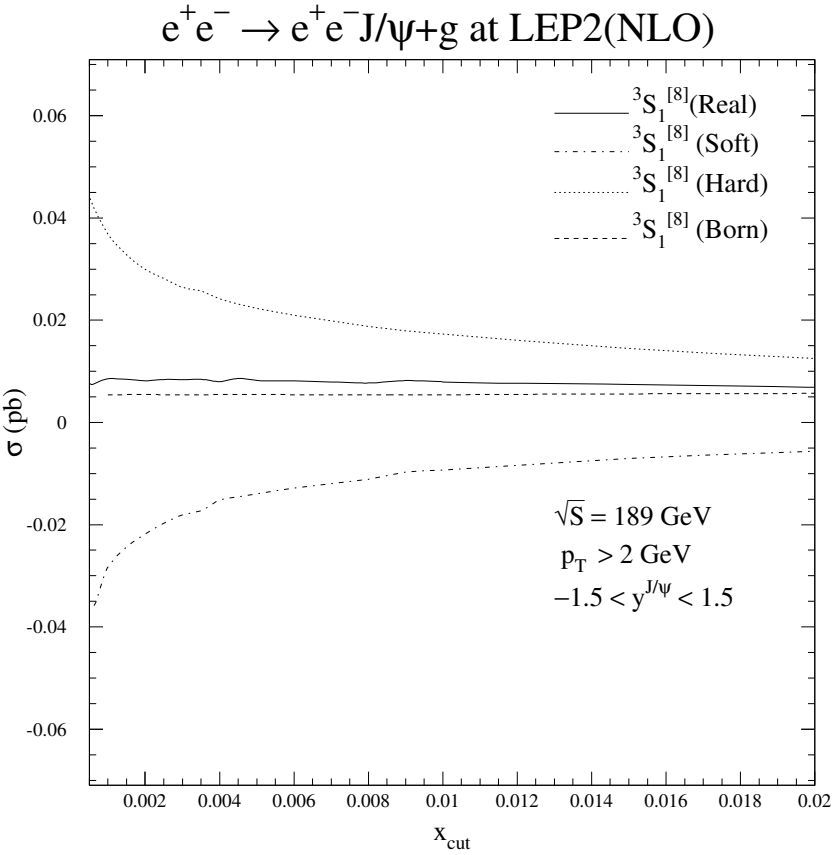

Figure 6.6: The cut-off independence of the total cross section for the process $\gamma\gamma \to c\bar{c}[^3S_1^{[8]}] + g$ at LEP2.

depend on the cut-off parameter when this parameter varies from $2 \cdot 10^{-3}$ to $2 \cdot 10^{-2}$. We have also explored higher and lower sectors for this parameter but it turned out that the appropriate range for the numerical stability and cut-off independence is the one shown in this figure. Therefore we have chosen for our predictions a cut-off value in this range.

In Fig. 6.7 we have shown the same cut-off independence of the real cross section, but now considering the ${}^3P_j^{[8]} + {}^1S_0^{[8]}$ channel with the same convention for the line-types. We conclude also for that process that the numerical analysis does not depend the unphysical parameter x_{cut}, if this is chosen in the range $10^{-3} - 10^{-2}$.

In Fig. 6.8 we show the transverse momentum distribution of the LO and NLO cross sections $d\sigma/dp_T$ for the process $\gamma\gamma \to c\bar{c}[^3S_1^{[8]}] + g$. The dashed curve shows the p_T-dependence of the Born contribution, the dotted curve corresponds to the NLO contribution from the $^3S_1^{[8]}$ channel and the full curve represents the NLO results considering all

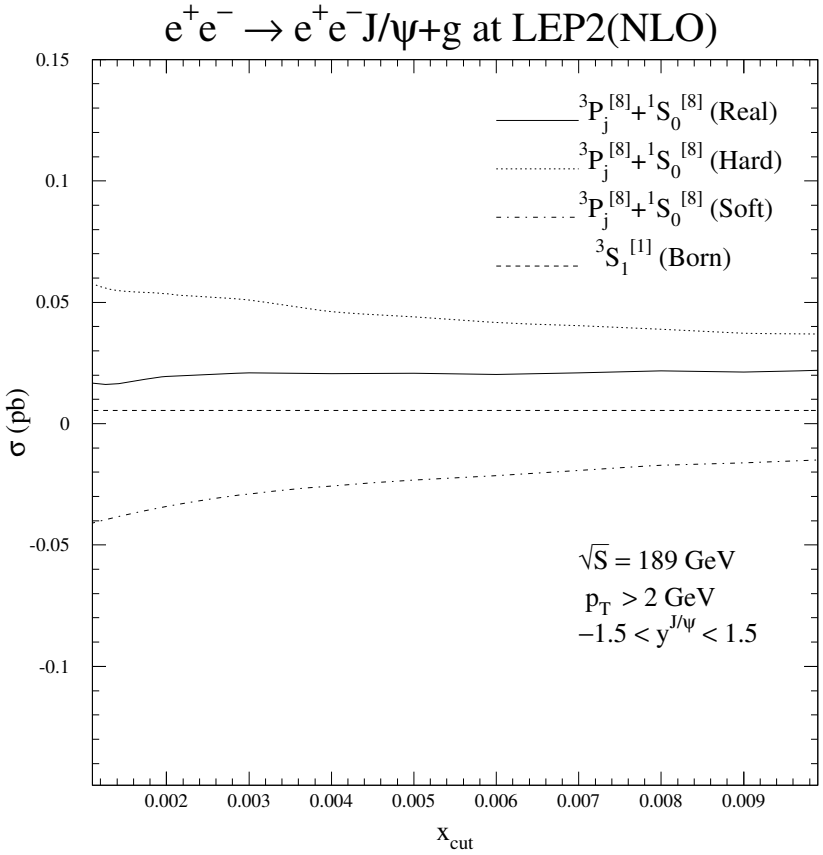

Figure 6.7: The cut-off independence of the total hadronic cross section for the process $\gamma\gamma \to c\bar{c}[n] + g$, where $[n] =^3 P_J^{[8]},^1 S_0^{[8]}$ at LEP2.

NRQCD allowed channels. We conclude from the figure that the NRQCD NLO corrections are almost an order of magnitude larger than the Born ones, a behaviour already predicted [42]. We notice also that the NLO contributions have a milder dependence on p_T than the Born contributions, which arises in higher cross section at large transverse momenta.

In Fig. 6.9 we investigate the rapidity distributions $d\sigma/dy^{J/\Psi}$ for $\gamma\gamma \to c\bar{c}[n] + g$. As before, we show separately the Born (dashed lines), the ${}^3S_1^{[8]}$ channel at NLO (doted lines) and the full NLO contribution (solid lines). The y distributions displayed in Fig. 6.9 are all symmetric about $y = 0$ with a maximum at this rapidity value, which can be explained in the same manner as for Fig. 6.3. LO and NLO curves have similar dependence on the rapidity which can be explained by the fact that the subsequent Feynman graphs are only of the *direct* type, which does not break the axial symmetry around the collision direction

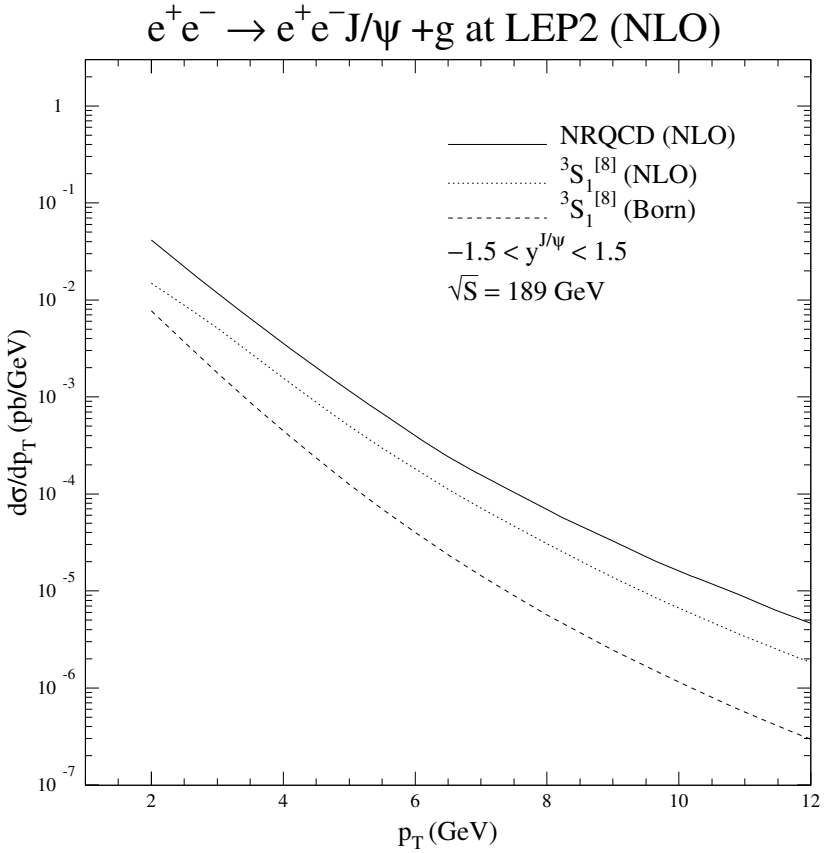

Figure 6.8: The transverse momentum distribution $d\sigma/dp_T$ of $\gamma\gamma \rightarrow c\bar{c}[n] + g$ via bremsstrahlung at LEP2.

.

In Fig. 6.10 we show the scale dependence of the theoretical predictions for LO and NLO $d\sigma/dp_T$ at $p_T = 2$ Gev of $\gamma\gamma \rightarrow c\bar{c}[^3S_1^{[8]}] + g$ using a logarithmic scale on the abscissa. We have chosen only these channels because there are Born, virtual and real contributions and all of them depend on the running strong coupling constant α_s. We have varied the renormalization scale around the value $\mu = m_T$ from 0.25 to 4. There is no dependence on the factorization scale because we are analyzing only the direct process. Our results show that the scale dependence of the NLO contributions at large values for this parameter is flatter than that of the LO ones. We can also conclude from the figure that at small energy scales this dependence is very strong and that perturbation theory is not valid anymore.

In Fig. 6.11 we show the variation of the integrated cross section (over the same

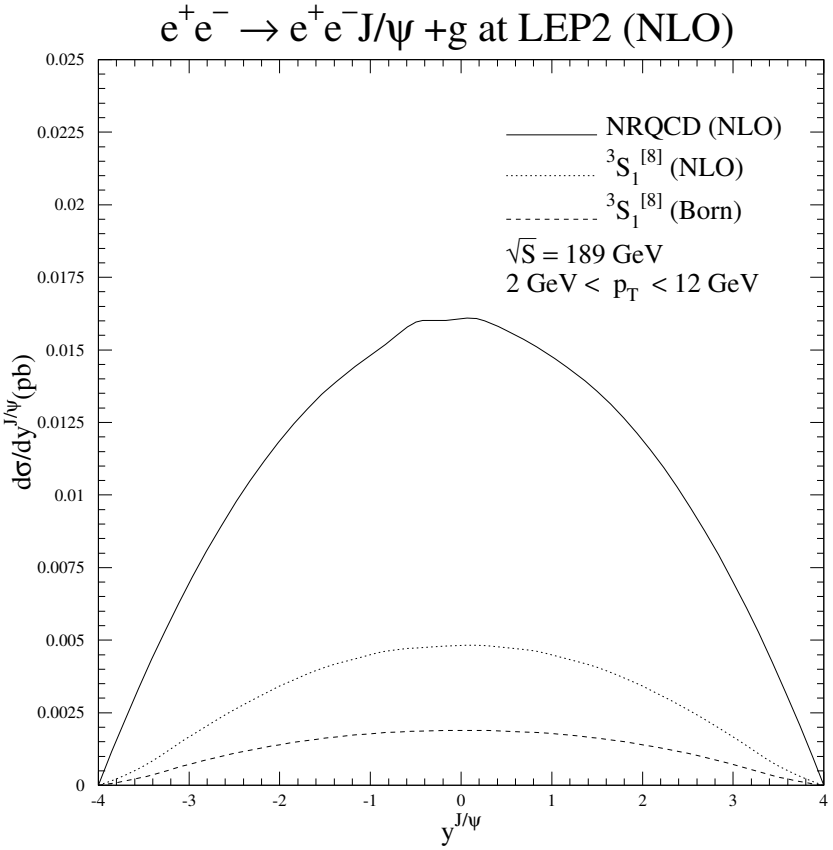

Figure 6.9: Rapidity distribution $d\sigma/dy_{J/\Psi}$ for $\gamma\gamma \rightarrow c\bar{c}[n] + g$ via bremsstrahlung at LEP2, considering LO and NLO contributions.

range as before) with the center-of-mass e^+e^- energy $\sqrt{S}$. It turns out that the factor $K = \sigma_{NLO}/\sigma_{LO}$ is almost independent of the hadronic energy and has an average value of $K = 6$. As expected the total cross section increases at higher energies.

It turned out from our analysis that at large transverse-momentum for J/Ψ-meson, the NLO corrections are of about an order of magnitude larger than LO contributions. According to this, we expect that at CM energies proposed for TESLA, the direct-processes to become dominant, overcoming the single-resolved ones .

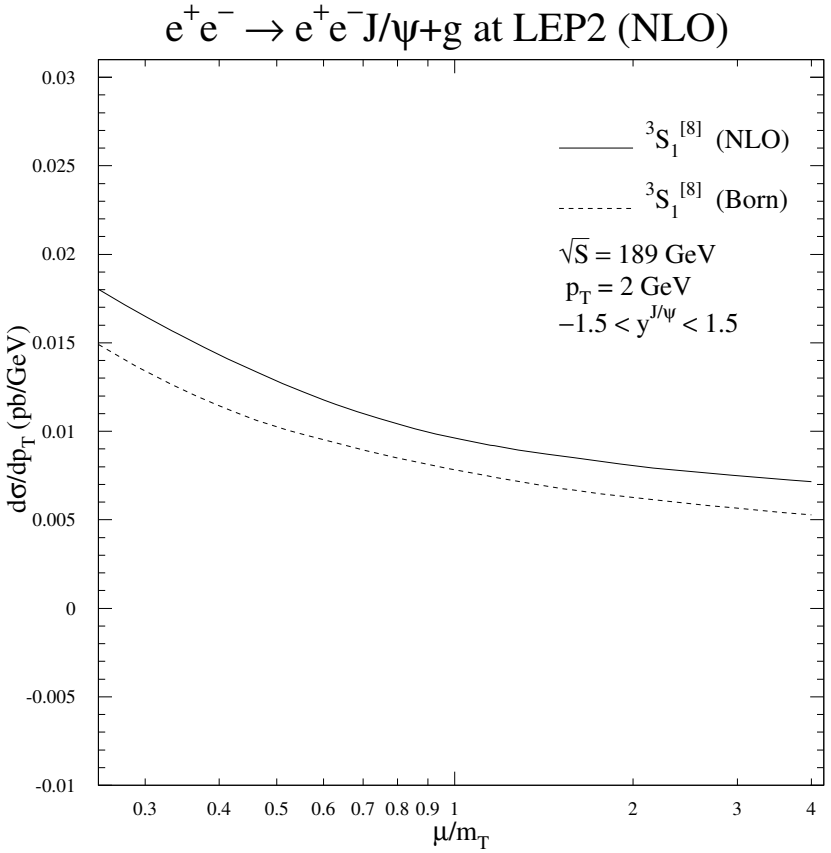

Figure 6.10: The scale dependence of the total cross section for $\gamma\gamma \to c\bar{c}[n] + g$ via bremsstrahlung at LEP2.

6.3 LO analysis of the process $\gamma\gamma \to J/\Psi + 2$ jets

We now turn to the case where the J/Ψ-particle is produced together with two hadronic jets. The corresponding Feynman diagrams are shown in Fig. 5.2 and in Fig. 5.3. In addition we have included the contribution from diagrams shown in Fig. 6.12. The MEs for the last contribution exhibit collinear singularities (one of the light quarks or anti-quarks becomes parallel with the photon). These singularities are absorbed at NLO into the renormalized parton densities of the photon encountered in the single-resolved process. A complete NLO analysis including direct-, single-, and double-resolved processes is beyond the scope of this work. We therefore take into account only the hard part of the allowed phase space and impose additional cuts on the rapidities and transverse momenta of the two observed jets.

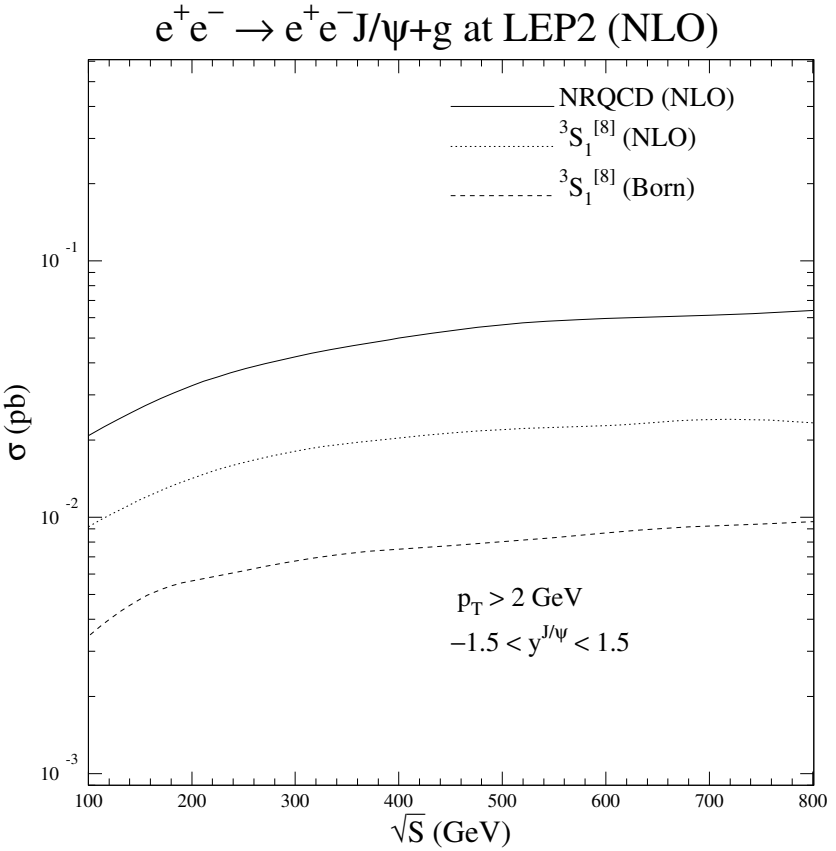

Figure 6.11: The energy distribution of the total cross section for $\gamma\gamma \to c\bar{c}[n] + g$ via bremsstrahlung at LEP2.

Working in the same CMS of Eq. (3.24) and calling the azimuthal angles, transverse momenta, and rapidities of the additional particles ϕ_i, p_{Ti}, and y_i, respectively, with $i = 1, 2$, we have [at the partonic level]

$$\begin{aligned} \frac{d^6\sigma(e^+e^- \to e^+e^- J/\psi + 2j)}{dp_T^2 dy d\phi_1 dp_{T1}^2 dy_1 dy_2} &= \frac{1}{512\pi^4 s^2} x_+ f_{\gamma/e}(x_+) x_- f_{\gamma/e}(x_-) \\ &\times \sum_n \sum_{ab=gg,q\bar{q}} \overline{|\mathcal{M}^2|}(\gamma\gamma \to c\bar{c}[n]ab), \end{aligned} \tag{6.1}$$

where

$$x_\pm = \frac{[m_T \exp(\pm y) + p_{T1} \exp(\pm y_1) + p_{T2} \exp(\pm y_2)]}{\sqrt{S}}, \tag{6.2}$$

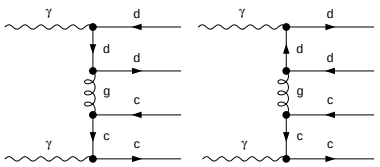

Figure 6.12: Additional Feynman diagrams contributing to $\gamma\gamma \to c\bar{c}[^3S_1^{[8]}] + 2$ jets.

with

$$p_{T2} = \sqrt{p_T^2 + p_{T1}^2 + 2p_T p_{T1}\cos\phi_1}. \tag{6.3}$$

The accessible phase space is defined by

$$\begin{aligned}
&0 \le p_T \le \frac{S - M^2}{2\sqrt{S}},\\
&|y| \le \mathrm{Arcosh}\frac{S + M^2}{2\sqrt{S}m_T},\\
&0 \le \phi_1 \le 2\pi,\\
&0 \le p_{T1} \le \frac{S + M^2 - 2\sqrt{S}m_T\cosh y}{2\left(\sqrt{S + m_T^2 - 2\sqrt{S}m_T\cosh y} + p_T\cos\phi_1\right)},\\
&\left|y_1 - \frac{1}{2}\ln\frac{\sqrt{S} - m_T\exp(y)}{\sqrt{S} - m_T\exp(-y)}\right| \le \mathrm{Arcosh}\ \frac{S + M^2 - 2\sqrt{S}m_T\cosh y - 2p_T p_{T1}\cos\phi_1}{2p_{T1}\sqrt{S + m_T^2 - 2\sqrt{S}m_T\cosh y}},\\
&-\ln\frac{\sqrt{S} - m_T\exp(-y) - p_{T1}\exp(-y_1)}{p_{T2}} \le y_2 \le \ln\frac{\sqrt{S} - m_T\exp(y) - p_{T1}\exp(y_1)}{p_{T2}}.
\end{aligned} \tag{6.4}$$

The analytic expressions for the various spin-averaged, squared matrix elements $\overline{|\mathcal{M}^2|}(\gamma\gamma \to c\bar{c}[n] + ab)$ are too lengthy to be listed here.

In Figs. 6.13 and 6.14, we study the p_T and y distributions for $\gamma\gamma \to J/\psi + jj$, respectively, again imposing the cuts $p_T \ge 2$GeV and $-1.5 \le y \le 1.5$. In addition, following Ref. [61], we require the two jets to have transverse momenta $p_{Ti} > 5$ GeV and rapidities $|y_i| < 2$ $(i = 1, 2)$ and to be separated by $\Delta R = \sqrt{(y_1 - y_2)^2 + (\phi_1 - \phi_2)^2} > 1$ according to the k_T-clustering algorithm [62]. While no actual clustering is performed, the separation of the two jets is necessary to avoid collinear singularities in the final state.

In Fig. 6.13, we analyze the relative importance of the various colour-octet channels. We observe that $^1S_0^{[8]}$ is the most important channel. As is familiar from inclusive J/ψ-meson hadroproduction at the Tevatron [5], the $^1S_0^{[8]}$ and $^3P_J^{[8]}$ channels have very similar p_T-dependences for $p_T \approx 5$ GeV. By the same token, this implies that the theoretical uncertainty related to the lack of information on how M_r breaks into $\left\langle \mathcal{O}_8^{J/\psi}\,[^1S_0]\right\rangle$ and

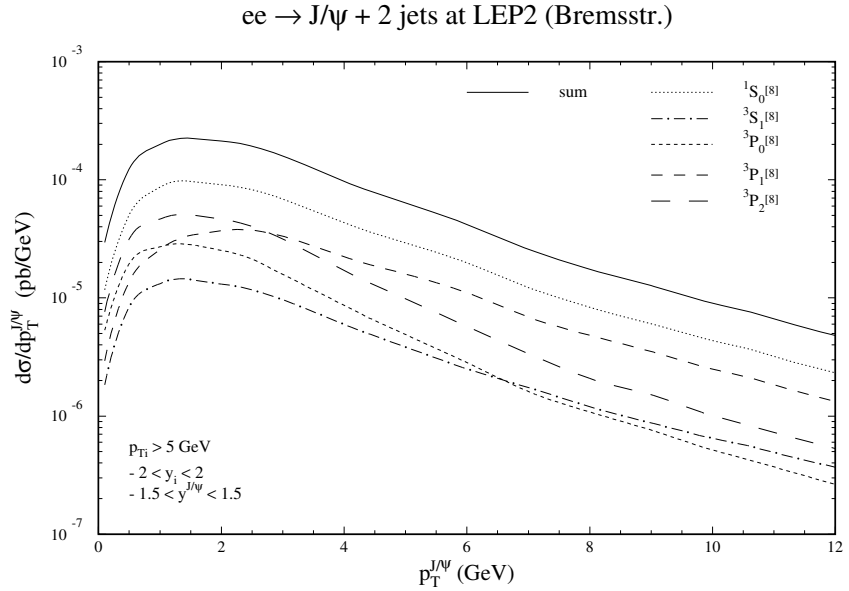

Figure 6.13: Transverse-momentum distribution $d\sigma/dp_T$ of $\gamma\gamma \to J/\psi + jj$ via bremsstrahlung at LEP2. The contributions due to the various colour-octet channels are also shown separately.

$\left\langle \mathcal{O}_8^{J/\psi}\left[^3P_0\right]\right\rangle$ is modest. On the other hand, the $^3S_1^{[8]}$-channel contribution falls off less rapidly as p_T increases. The suppression of the $^3S_1^{[8]}$ contribution relative to the combination of $^1S_0^{[8]}$ and $^3P_J^{[8]}$ may be traced to the fact that M_r is almost a factor of 20 larger than $\left\langle \mathcal{O}_8^{J/\psi}\left[^3S_1\right]\right\rangle$.

The total y distribution shown in Fig. 6.14 (solid line) exhibits a marked minimum at $y = 0$. Its decomposition into the contributions where the dijets are of gg (dotted line) and $q\bar{q}$ (dashed line) origin clarifies that this minimum stems from the latter contribution. This may be understood by observing that the q and $\bar{q}$ quarks may be created from the splitting of the incident photons, in which case they are dominantly collinear to the mother photons. On the other hand, the final-state gluons are either both directly radiated off the heavy-quark line or emerge through the $1 \to 2$ splitting of a virtual gluon that is radiated off the heavy-quark line, so that the resulting y distribution is expected to have a shape similar to the one of $\gamma\gamma \to J/\psi + j$ studied in Fig. 3.5, which has a maximum at $y = 0$.

We now turn to $\gamma\gamma$ collisions at TESLA. In the e^+e^- mode, the photons originate from bremsstrahlung and beamstrahlung, while in the $\gamma\gamma$ mode they arise from the back-

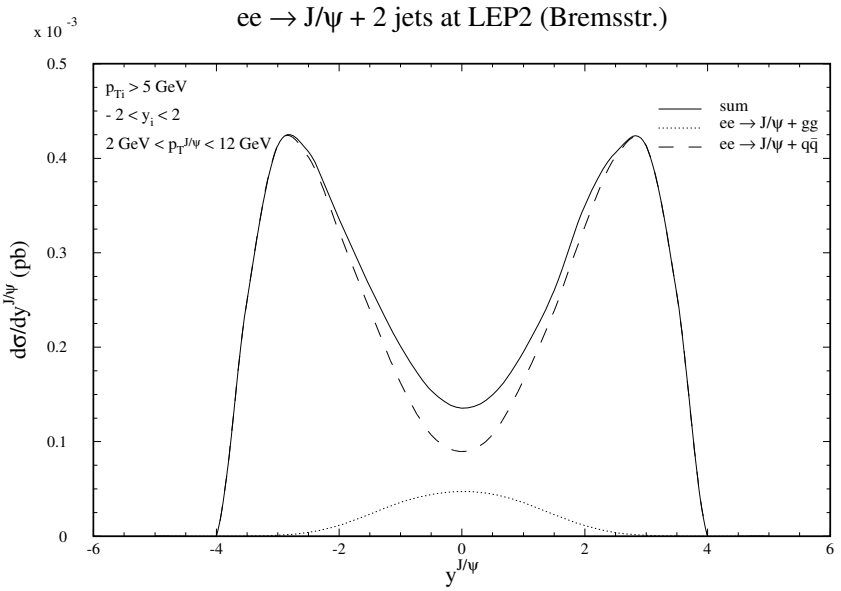

Figure 6.14: Rapidity distribution $d\sigma/dy$ of $\gamma\gamma \to J/\psi + jj$ via bremsstrahlung at LEP2. The contributions due to quark and gluon dijets are also shown separately.

scattering of laser light on the incident electron and positron beams.

In Figs. 6.15–6.18, the contributions due to bremsstrahlung (dashed lines), beamstrahlung (dot-dashed lines), their coherent superposition (solid lines), and Compton scattering (dotted lines) are shown separately. We apply the same cuts on p_T, y, p_{Ti}, and y_i $(i = 1, 2)$ as in the LEP2 case. The p_T and y distributions of $\gamma\gamma \to J/\psi + jj$, with all the leading colour-octet channels included, are shown in Figs. 6.17 and 6.18, respectively. Comparing Fig. 6.17 with Fig. 6.15, we observe that now the Compton contribution starts to exceed the one due to bremsstrahlung and beamstrahlung already at $p_T \approx 9$ GeV. This may be understood by observing that it is now possible for x to take large values at small values of p_T if the dijet invariant mass is sufficiently large. As in Fig. 6.14, the y distributions are symmetric about $y = 0$ and exhibit a local minimum there. This feature is particularly pronounced for the Compton contribution. As in Fig. 6.16, the beamstrahlung contribution exceeds the bremsstrahlung one in the central y region and only extends out to $|y| \approx 3$, while the bremsstrahlung one dominates for $|y| \approx 2.2$.

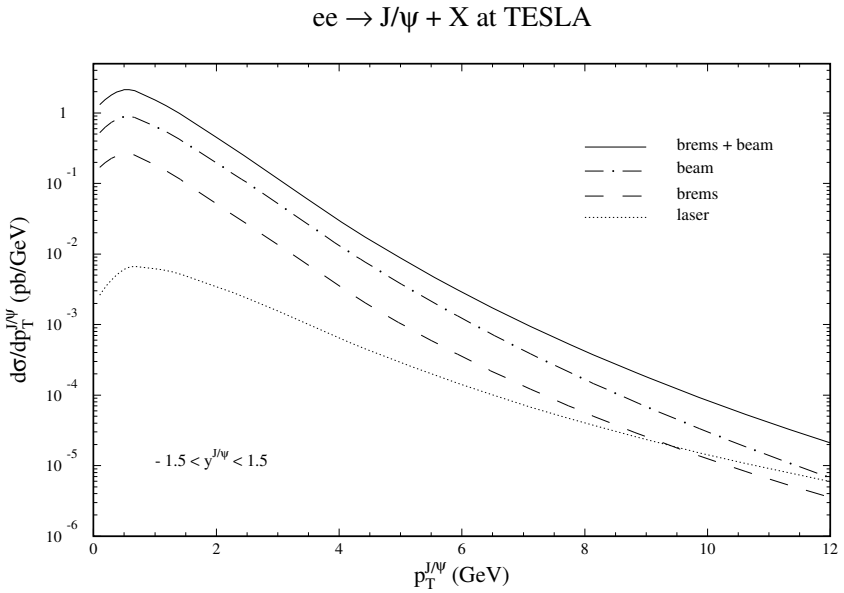

Figure 6.15: Transverse-momentum distribution $d\sigma/dp_T$, integrated over rapidity interval $|y| < 1.5$, of $\gamma\gamma \to J/\psi + X$, where X represents a gluon jet or a prompt photon, via bremsstrahlung, beamstrahlung, their coherent superposition, and laser back-scattering at TESLA.

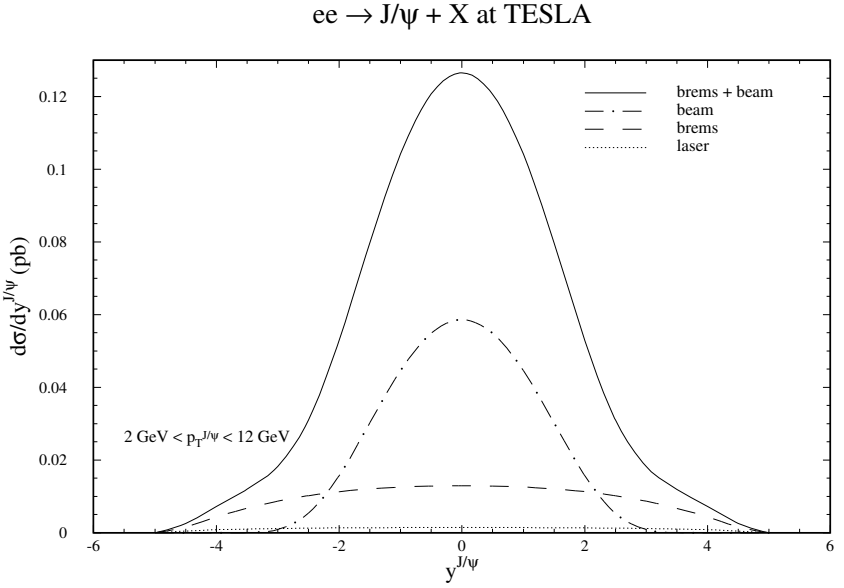

Figure 6.16: Rapidity distribution $d\sigma/dy$, integrated over transverse-momentum interval $2 < p_T < 12$ GeV, of $\gamma\gamma \to J/\psi + X$, where X represents a gluon jet or a prompt photon, via bremsstrahlung, beamstrahlung, their coherent superposition, and laser back-scattering at TESLA.

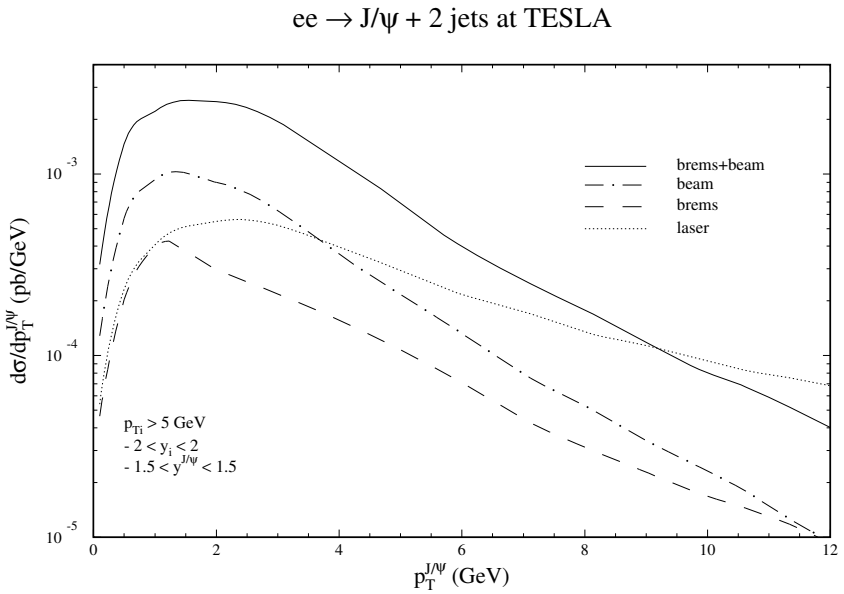

Figure 6.17: Transverse-momentum distribution $d\sigma/dp_T$ of $\gamma\gamma \to J/\psi + jj$ via bremsstrahlung, beamstrahlung, their coherent superposition, and laser back-scattering at TESLA.

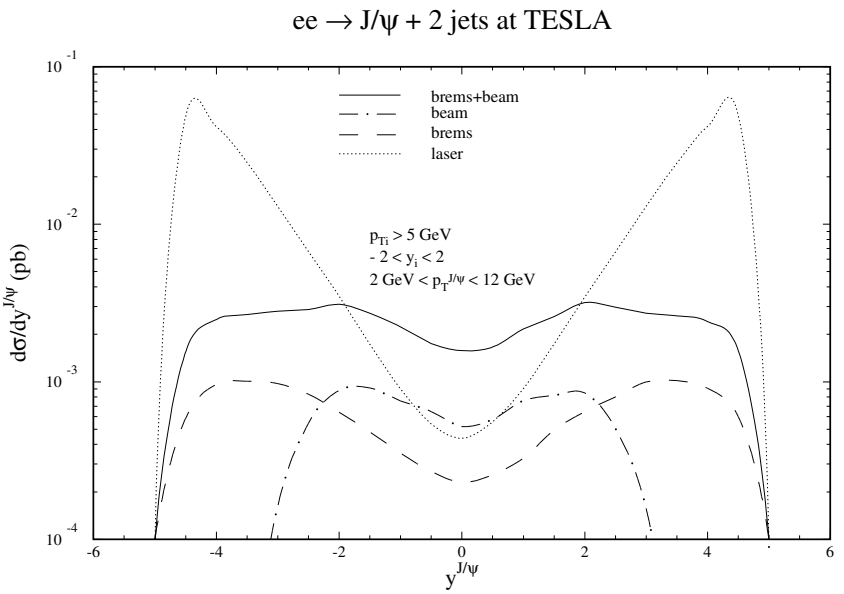

Figure 6.18: Rapidity distribution $d\sigma/dy$ of $\gamma\gamma \to J/\psi + jj$ via bremsstrahlung, beamstrahlung, their coherent superposition, and laser back-scattering at TESLA.

Chapter 7

Conclusions

The NRQCD factorization approach is a systematic framework for inclusive quarkonium production and provides an elegant explanation for the large direct J/Ψ cross section measured in $p\bar{p}$ collisions at Fermilab Tevatron. The absence of transversely polarized J/Ψ at large transverse momentum, if confirmed with higher statistics, could imply that the conventional NRQCD velocity-scaling rules have to be replaced by alternative schemes, or that higher-order QCD effects are essential to describe the spin-dependence of the charm cross section.

On the other hand, the experimental data on charmonium photoproduction are adequately described by the colour-singlet channel, including next-to-leading order corrections in α_s. But there is a considerable amount of uncertainty in the normalization of the theoretical prediction, and no constraints on the size of colour-octet processes can be deduced from the photoproduction analysis at present.

A global analysis of different production processes is needed to verify the universality of long-distance matrix elements in NRQCD. One of the most accurate place to test the NRQCD validity is the J/Ψ production in the direct two-photon collisions. In contrast to hadro and photoproduction, the two-photon process is not plugged by the initial-state transverse-momentum effects, and by the uncertainties in the determination of the parton densities. In this context, the photon-photon production can be chosen as a discriminator between the NRQCD mechanism and the CSM. Accordingly, reduced theoretical uncertainties are required, and that can be achieved by a complete next-to-leading-order analysis of the hard-scattering processes within QCD. Higher precision for the theoretical predictions can be achieved, if one considers corrections in v^2 to the operator matrix elements.

With this paper we make a first step towards a complete next-to-leading-order analysis

of the J/Ψ-meson production in the photon-photon collisions. In this sense, we have analytically computed the squared matrix elements for all leading-order processes and checked our results against those already present in the literature. For the next-to-leading-order corrections we focused on the processes $\gamma\gamma \to c\bar{c} + \gamma$ and $\gamma\gamma \to c\bar{c} + g$. For their analysis, the NRQCD formalism provides a consistent theory for including both colour-singlet and colour-octet states and a systematic cancellation of all types of singularities in contrast with the CSM.

We have presented complete leading-order numerical results for the process $\gamma\gamma \to J/\Psi + X$, considering the NRQCD formalism and including the contributions from both direct and resolved photons. The comparison of the transverse-momentum distribution of J/ψ-mesons promptly produced in $\gamma\gamma$ collisions with the new data taken by the DELPHI Collaboration at LEP2 confirm NRQCD predictions, while they disfavour those obtained within the traditional CSM.

The contributions due to single-resolved and double-resolved photon-photon production are expected to be suppressed, if the J/ψ-meson transverse momentum and/or the dijet invariant mass are large compared to the J/ψ-meson mass. In the CSM, only $\gamma\gamma \to J/\psi + \gamma$ can happen in direct photon-photon production. Experimental observation of $\gamma\gamma \to J/\psi + j$ or $\gamma\gamma \to J/\psi + jj$ with the predicted cross sections would provide evidence for the existence of colour-octet processes in nature.

Our next-to-leading-order numerical analysis established that the pure CSM predictions for $\gamma\gamma \to J/\psi + \gamma$ are reduced by about (30%) and the transverse momentum distribution falls off more rapidly than the Born one, becoming even negative for some kinematical regions. The consideration of both colour-singlet and colur-octet states solves this theoretical inconsistency due to the fact that colour-octet channels have a flatter transverse momentum distribution. The next-to-leading-order numerical analysis of the process $\gamma\gamma \to J/\psi + j$ has shown an increase of the total cross section of about an order of magnitude. This implies that the total cross sections for the two processes become comparable.

We calculated the cross section of $\gamma\gamma \to J/\psi + jj$ in direct two-photon production at leading-order in the NRQCD factorization formalism and provided theoretical predictions for the J/ψ-meson transverse momentum and rapidity distributions in $\gamma\gamma$ collisions via initial-state bremsstrahlung at LEP2 and via bremsstrahlung and beamstrahlung or laser back-scattering at TESLA.

The theoretical issues to be addressed in the future include a critical evaluation of the power counting rules of NRQCD and the calculation of the higher-order QCD corrections for single- and double-resolved processes.

Appendix A

Colour algebra

The $SU(3)$ generators $T^a (a = 1, \cdots, N_c^2 - 1)$, where $N_c = 3$, are hermitian, traceless matrices which generate the closed $SU(3)$ algebra,

$$\left[T^a, T^b\right] = if^{abc}T^c, \tag{A.1}$$

with f^{abc} the structure functions.

The fundamental representation is 3-dimensional where the T^a satisfy an additional relation,

$$\left\{T^a, T^b\right\} = d^{abc}T^c + \frac{\delta^{ab}}{N_c}, \tag{A.2}$$

which is consistent with the normalization

$$\mathrm{Tr}\left[T^a T^b\right] = T_F\delta^{ab}, \qquad T_F = \frac{1}{2}. \tag{A.3}$$

Here d^{abc} is totally symmetric in a,b and c and is given by

$$d^{abc} = 2\mathrm{Tr}[T^a, T^b T^c]. \tag{A.4}$$

Using Eq. (A.1) and Eq. (A.2) we obtain the following useful relations:

$$\sum_a \left(T^a T^a\right)_{ij} = C_F\delta_{ij}, \qquad C_F = \frac{N_c^2 - 1}{2N_c} = \frac{4}{3}, \tag{A.5}$$

$$\sum_{bc} f^{abc}f^{ebc} = C_A\delta^{ae}, \qquad C_A = N_C = 3, \tag{A.6}$$

$$\sum_{bc} d^{abc}d^{ebc} = 4B_F\delta^{ae}, \qquad B_F = \frac{N_c^2 - 4}{4N_c} = \frac{5}{12}, \tag{A.7}$$

$$D_F = \sum_i \delta_{ii} = N_c = 3, \tag{A.8}$$

$$D_A = \sum_a \delta^{aa} = N_c^2 - 1 = 8. \tag{A.9}$$

The traces of products of three generators in the fundamental representation are

$$Tr(T^a T^b T^c) = \frac{1}{4}(d^{abc} + if^{abc}). \tag{A.10}$$

The symmetric traceless component of a tensor can be written as

$$T^{ij} = \left(\frac{T^{ij} + T^{ji}}{2}\right) - \frac{T^{kk}\delta^{ij}}{3}. \tag{A.11}$$

Using Fierz's decomposition relations for the colour subspace

$$\delta_{i'i}\delta_{j'j} = \frac{1}{N_c}\delta_{ji}\delta_{i'j'} + 2T^a_{ij}T^a_{i'j'} \tag{A.12}$$

and for the spin subspace

$$\begin{aligned} \delta_{i'i}\delta_{j'j} &= \frac{1}{2}\left(\delta_{ji}\delta_{i'j'} + \sigma_{ji}\sigma_{i'j'}\right) \\ &\{\sigma^a, \sigma^b\} = 2\delta^{ab} \end{aligned} \tag{A.13}$$

we can expand the product of four-fermion spinors as

$$\begin{aligned} \Psi^\dagger\Psi\chi^\dagger\chi &= \frac{1}{2N_c}\left(\Psi^\dagger\chi\cdot\chi^\dagger\Psi + \Psi^\dagger\sigma^i\chi\cdot\chi^\dagger\sigma^j\Psi\right) \\ &+ \left(\Psi^\dagger T^a\chi\cdot\chi^\dagger T^a\Psi + \Psi^\dagger T^a\sigma^i\chi\cdot\chi^\dagger T^a\sigma^j\Psi\right). \end{aligned} \tag{A.14}$$

Starting from this relation we introduce in the next Section the NRQCD operators.

Using Eq. (A.1) and Eq. (A.2) we obtain

$$\sum T^a_{ij}T^b_{jk} = C_F\delta_{ik}, \tag{A.15}$$

$$\sum_a T^a_{ij}T^a_{kl} = \frac{1}{2}\left(\delta_{il}\delta_{jk} - \frac{1}{N_c}\delta_{ij}\delta_{kl}\right). \tag{A.16}$$

Other useful relations for order α_s corrections to the OMEs are:

$$\begin{aligned} T^aT^b\otimes T^bT^a &= \frac{N_c^2-1}{4N_c^2}1\otimes 1 + \frac{N_c^2-2}{2N_c}T^a\otimes T^a = \frac{C_F}{2N_c}1\otimes 1 + \frac{N_c^2-2}{2N_c}T^a\otimes T^a, \\ T^aT^b\otimes T^aT^b &= \frac{N_c^2-1}{4N_c^2}1\otimes 1 - \frac{1}{N_c}T^a\otimes T^a = \frac{C_F}{2N_c}1\otimes 1 - \frac{2}{2N_c}T^a\otimes T^a, \end{aligned} \tag{A.17}$$

$$
\begin{aligned}
&\left(T^aT^b\otimes T^bT^a + T^aT^b\otimes T^bT^a\right)(1\otimes 1)\\
&\qquad = \left(\frac{C_F}{2N_c}1\otimes 1 + 2B_F T^a\otimes T^a\right)(1\otimes 1)\\
&\qquad = 2\Big[C_F\left(\frac{1}{\sqrt{N_c}}\otimes\frac{1}{\sqrt{N_c}}\right)\left(\frac{1}{\sqrt{2}}\otimes\frac{1}{\sqrt{2}}\right)\\
&\qquad\quad + B_F\left(\sqrt{2}T^a\otimes\sqrt{2}T^a\right)\left(\frac{1}{\sqrt{2}}\otimes\frac{1}{\sqrt{2}}\right)\Big]\\
&\qquad = 2\left[C_F\,\mathcal{O}_1(n) + B_F\,\mathcal{O}_8(n)\right], \qquad \text{(A.18)}\\
T^a\otimes T^bT^aT^b &= -\frac{1}{2N_c}T^a\otimes T^a = \left(C_F - \frac{C_A}{2}\right)T^a\otimes T^a,\\
1\otimes T^b 1\otimes T^b &= 1\otimes 1\sum T^b_{ij}T^b_{kl}\delta_{jk} = C_F 1\otimes 1, \qquad \text{(A.19)}\\
T^bT^bT^a\otimes T^a &= C_F T^a\otimes T^a,\\
T^bT^b 1\otimes 1 &= C_F 1\otimes 1, \qquad \text{(A.20)}
\end{aligned}
$$

where $\otimes$ stands for the multiplication of the colour- or spin-subspace of the heavy-quark with that of the heavy anti-quark. This decomposition is used in the definition of the NRQCD operators, given in the Chapter 2.

Appendix B

NRQCD operators

Starting from the NRQCD corrections to the Lagrangian

$$\delta\mathcal{L}_{6-dim} \sim \Psi^\dagger\chi\chi^\dagger\Psi \qquad \delta\mathcal{L}_{8-dim} \sim \Psi^\dagger\left(-i\frac{\mathbf{D}}{2}\right)\chi\chi^\dagger\left(-i\frac{\mathbf{D}}{2}\right)\Psi, \tag{B.1}$$

and using Eq. (A.14) we define:

- S-wave annihilation operators

$$\mathcal{O}_1[^1S_0] = \Psi^\dagger\frac{1}{\sqrt{2}}\frac{1}{\sqrt{N_c}}\chi\cdot\chi^\dagger\frac{1}{\sqrt{2}}\frac{1}{\sqrt{N_c}}\Psi, \tag{B.2}$$

$$\mathcal{O}_1[^3S_1] = \Psi^\dagger\frac{\boldsymbol{\sigma}}{\sqrt{2}}\frac{1}{\sqrt{N_c}}\chi\cdot\chi^\dagger\frac{\boldsymbol{\sigma}}{\sqrt{2}}\frac{1}{\sqrt{N_c}}\Psi, \tag{B.3}$$

$$\mathcal{O}_8[^1S_0] = \Psi^\dagger\frac{1}{\sqrt{2}}\sqrt{2}T^a\chi\cdot\chi^\dagger\frac{1}{\sqrt{2}}\sqrt{2}T^a\Psi, \tag{B.4}$$

$$\mathcal{O}_8[^3S_1[= \Psi^\dagger\frac{\sigma}{\sqrt{2}}\sqrt{2}T^a\chi\cdot\chi^\dagger\frac{\sigma}{\sqrt{2}}\sqrt{2}T^a\Psi. \tag{B.5}$$

- Relativistic corrections to the S-wave operators

$$\mathcal{R}_1[^1S_0] = \frac{1}{2}\left[\Psi^\dagger\frac{1}{\sqrt{2}}\frac{1}{\sqrt{N_c}}\chi\cdot\chi^\dagger\left(-i\overleftrightarrow{\mathbf{D}}\right)^2\frac{1}{\sqrt{2}}\frac{1}{\sqrt{N_c}}\Psi + H.c.\right], \tag{B.6}$$

$$\mathcal{R}_1[^3S_1] = \frac{1}{2}\left[\Psi^\dagger\frac{\boldsymbol{\sigma}}{\sqrt{2}}\frac{1}{\sqrt{N_c}}\chi\cdot\chi^\dagger\left(-i\overleftrightarrow{\mathbf{D}}\right)^2\frac{\boldsymbol{\sigma}}{\sqrt{2}}\frac{1}{\sqrt{N_c}}\Psi + H.c.\right], \tag{B.7}$$

$$\mathcal{R}_8[^1S_0] = \frac{1}{2}\left[\Psi^\dagger\frac{1}{\sqrt{2}}\sqrt{2}T^a\chi\cdot\chi^\dagger\left(-i\overleftrightarrow{\mathbf{D}}\right)^2\frac{1}{\sqrt{2}}\sqrt{2}T^a\Psi + H.c.\right], \tag{B.8}$$

$$\mathcal{R}_8[^3S_1[= \frac{1}{2}\left[\Psi^\dagger\frac{\sigma}{\sqrt{2}}\sqrt{2}T^a\chi\cdot\chi^\dagger\left(-i\overleftrightarrow{\mathbf{D}}\right)^2\frac{\sigma}{\sqrt{2}}\sqrt{2}T^a\Psi + H.c.\right], \tag{B.9}$$

where $H.c$ stands for the Hermitian conjugate operator, and
$\chi^\dagger \overleftrightarrow{\mathbf{D}} \Psi = \chi^\dagger(\mathbf{D}\Psi) - (\mathbf{D}\chi)\Psi)$.

- P-wave annihilation operators

$$\mathcal{O}_1[^1P_1] = \Psi^\dagger\left(-i\frac{\overleftrightarrow{\mathbf{D}}}{2}\right)\frac{1}{\sqrt{2}}\frac{1}{\sqrt{N_c}}\chi\cdot\chi^\dagger\left(-i\frac{\overleftrightarrow{\mathbf{D}}}{2}\right)\frac{1}{\sqrt{2}}\frac{1}{\sqrt{N_c}}\Psi, \tag{B.10}$$

$$\mathcal{O}_1[^3P_0] = \Psi^\dagger\left(-i\frac{\overleftrightarrow{\mathbf{D}}}{2}\cdot\frac{\boldsymbol{\sigma}}{\sqrt{2}}\right)\frac{1}{\sqrt{N_c}}\chi\cdot\chi^\dagger\left(-i\frac{\overleftrightarrow{\mathbf{D}}}{2}\cdot\frac{\boldsymbol{\sigma}}{\sqrt{2}}\right)\frac{1}{\sqrt{N_c}}\Psi, \tag{B.11}$$

$$\mathcal{O}_1[^3P_1] = \Psi^\dagger\left(-i\frac{\overleftrightarrow{\mathbf{D}}}{2}\otimes\frac{\boldsymbol{\sigma}}{\sqrt{2}}\right)\frac{1}{\sqrt{N_c}}\chi\cdot\chi^\dagger\left(-i\frac{\overleftrightarrow{\mathbf{D}}}{2}\otimes\frac{\boldsymbol{\sigma}}{\sqrt{2}}\right)\frac{1}{\sqrt{N_c}}\Psi, \tag{B.12}$$

$$\mathcal{O}_1[^3P_2] = \Psi^\dagger\left(-i\frac{\overleftrightarrow{D^i}}{2}\frac{\sigma^j}{\sqrt{2}}\right)\frac{1}{\sqrt{N_c}}\chi\cdot\chi^\dagger\left(-i\frac{\overleftrightarrow{D^i}}{2}\frac{\sigma^j}{\sqrt{2}}\right)\frac{1}{\sqrt{N_c}}\Psi, \tag{B.13}$$

$$\mathcal{O}_8[^1P_1] = \Psi^\dagger\left(-i\frac{\overleftrightarrow{\mathbf{D}}}{2}\right)\frac{1}{\sqrt{2}}\sqrt{2}T^a\chi\cdot\chi^\dagger\left(-i\frac{\overleftrightarrow{\mathbf{D}}}{2}\right)\frac{1}{\sqrt{2}}\sqrt{2}T^a\Psi, \tag{B.14}$$

$$\mathcal{O}_8[^3P_0] = \Psi^\dagger\left(-i\frac{\overleftrightarrow{\mathbf{D}}}{2}\cdot\frac{\boldsymbol{\sigma}}{\sqrt{2}}\right)\sqrt{2}T^a\chi\cdot\chi^\dagger\left(-i\frac{\overleftrightarrow{\mathbf{D}}}{2}\cdot\frac{\boldsymbol{\sigma}}{\sqrt{2}}\right)\sqrt{2}T^a\Psi, \tag{B.15}$$

$$\mathcal{O}_8[^3P_1] = \Psi^\dagger\left(-i\frac{\overleftrightarrow{\mathbf{D}}}{2}\otimes\frac{\boldsymbol{\sigma}}{\sqrt{2}}\right)\sqrt{2}T^a\chi\cdot\chi^\dagger\left(-i\frac{\overleftrightarrow{\mathbf{D}}}{2}\otimes\frac{\boldsymbol{\sigma}}{\sqrt{2}}\right)\sqrt{2}T^a\Psi, \tag{B.16}$$

$$\mathcal{O}_8[^3P_2] = \Psi^\dagger\left(-i\frac{\overleftrightarrow{D^i}}{2}\frac{\sigma^j}{\sqrt{2}}\right)\sqrt{2}T^a\chi\cdot\chi^\dagger\left(-i\frac{\overleftrightarrow{D^i}}{2}\frac{\sigma^j}{\sqrt{2}}\right)\sqrt{2}T^a\Psi. \tag{B.17}$$

$$\tag{B.18}$$

- S- and P-wave production operators
  Rewriting the 4-fermionic annihilation operators as a product of two bilinear operators

$$\mathcal{O}[n] = \mathcal{O}^\dagger_{bilin}[n]\mathcal{O}_{bilin}[n],$$

the production operators can be written using the projector onto subspace of states that contains H as

$$\langle\mathcal{O}^H_{[1,8]}[n]\rangle = \langle 0|\mathcal{O}_{bilin}[n]|HX\rangle\langle HX|\mathcal{O}^\dagger_{bilin}[n]|0\rangle = \langle 0|\mathcal{O}_{bilin}[n]\mathcal{P}\mathcal{O}^\dagger_{bilin}[n]|0\rangle. \tag{B.19}$$

B.1 Order α_s corrections to NRQCD operators

Using the definition of the operators $\mathcal{O}$ and $\mathcal{R}$ given above, the colour algebra relations given in the App. A and the integrals discussed in Chapter 2, we can now compute order α_s corrections $\mathcal{M}$ to the lowest order (relative to v^2) operators ($\mathcal{O}$).

- Corrections to $\mathcal{O}_1[^1S_0]$

$$\mathcal{O}_1[^1S_0] = \left(\frac{1}{\sqrt{N_c}} \otimes \frac{1}{\sqrt{N_c}}\right)\left(\frac{1}{\sqrt{2}} \otimes \frac{1}{\sqrt{2}}\right). \tag{B.20}$$

We distinguish three types of contributions

1. self-energy type corrections (Fig. 2.2 a,b)

$$\begin{aligned}\mathcal{M}_{self} &= 4\left(-\frac{2\alpha_s}{3\pi}\right) v^2 C_F \frac{1}{4}\left(\frac{1}{\epsilon_{UV}} - \frac{1}{\epsilon_{IR}}\right)\left(\frac{1}{\sqrt{N_c}} \otimes \frac{1}{\sqrt{N_c}}\right)\left(\frac{1}{\sqrt{2}} \otimes \frac{1}{\sqrt{2}}\right) \\ &= C_F\left(-\frac{2\alpha_s}{3\pi}\right)\left(\frac{1}{\epsilon_{UV}} - \frac{1}{\epsilon_{IR}}\right)\frac{\mathcal{R}_1[^1S_0]}{M^2}.\end{aligned} \tag{B.21}$$

2. Coulomb-like diagrams (Fig. 2.2 b,c)

$$\begin{aligned}\mathcal{M}_{coul} &= 2\left(-\frac{2\alpha_s}{3\pi}\right) v^2 C_F \frac{1}{2}\left(\frac{1}{\epsilon_{UV}} - \frac{1}{\epsilon_{IR}}\right)\left(\frac{1}{\sqrt{N_c}} \otimes \frac{1}{\sqrt{N_c}}\right)\left(\frac{1}{\sqrt{2}} \otimes \frac{1}{\sqrt{2}}\right) \\ &= C_F\left(-\frac{2\alpha_s}{3\pi}\right)\left(\frac{1}{\epsilon_{UV}} - \frac{1}{\epsilon_{IR}}\right)\frac{\mathcal{R}_1[^1S_0]}{M^2}.\end{aligned} \tag{B.22}$$

3. corrections from diagrams (Fig. 2.2. d-g)

$$\begin{aligned}\mathcal{M}_{trans} &= 4\left(\frac{2\alpha_s}{3\pi}\right)\vec{v}\cdot\vec{v'}\frac{1}{4N_c}\left(\frac{1}{\epsilon_{UV}} - \frac{1}{\epsilon_{IR}}\right)\left(\sqrt{2}T^a \otimes \sqrt{2}T^a\right)\left(\frac{1}{\sqrt{2}} \otimes \frac{1}{\sqrt{2}}\right) \\ &= \left(\frac{2\alpha_s}{3\pi N_c}\right)\left(\frac{1}{\epsilon_{UV}} - \frac{1}{\epsilon_{IR}}\right)\frac{\mathcal{O}_8[^1P_1]}{M^2}.\end{aligned} \tag{B.23}$$

The sum of the last three equations gives

$$\mathcal{O}_1^{(1)}[^1S_0] = \left(\frac{2\alpha_s}{3\pi M^2}\right)\left(\frac{1}{\epsilon_{UV}} - \frac{1}{\epsilon_{IR}}\right)\left(\frac{1}{N_c}\mathcal{O}_8[^1P_1] - 2C_F\mathcal{R}_1[^1S_0]\right). \tag{B.24}$$

- corrections to $\mathcal{O}_8[^1S_0]$

$$\mathcal{O}_8[^1S_0] = \left(\sqrt{2}T^a\sqrt{2}T^a\right)\left(\frac{1}{\sqrt{2}} \otimes \frac{1}{\sqrt{2}}\right). \tag{B.25}$$

Considering the same classifications for order α_s corrections to the operator $\mathcal{O}_8[^1S_0]$ as before, we have

1. self-energy type corrections (Fig. 2.2 a,b)

$$\begin{aligned}\mathcal{M}_{self} &= 4\left(-\frac{2\alpha_s}{3\pi}\right)v^2 C_F\frac{1}{4}\left(\frac{1}{\epsilon_{UV}}-\frac{1}{\epsilon_{IR}}\right)\left(\sqrt{2}T^a\otimes\sqrt{2}\right)\left(\frac{1}{\sqrt{2}}\otimes\frac{1}{\sqrt{2}}\right)\\ &= C_F\left(-\frac{2\alpha_s}{3\pi}\right)\left(\frac{1}{\epsilon_{UV}}-\frac{1}{\epsilon_{IR}}\right)\frac{\mathcal{R}_8[^1S_0]}{M^2}.\end{aligned} \tag{B.26}$$

2. Coulomb-like diagrams (Fig. 2.3 b,c)

$$\begin{aligned}\mathcal{M}_{coul} &= 2\left(-\frac{2\alpha_s}{3\pi}\right)v^2\left(-\frac{1}{2N_c}\right)\frac{1}{2}\left(\frac{1}{\epsilon_{UV}}-\frac{1}{\epsilon_{IR}}\right)\left(\sqrt{2}T^a\otimes\sqrt{2}T^a\right)\left(\frac{1}{\sqrt{2}}\otimes\frac{1}{\sqrt{2}}\right)\\ &= \left(-\frac{1}{2N_c}\right)\left(-\frac{2\alpha_s}{3\pi}\right)\left(\frac{1}{\epsilon_{UV}}-\frac{1}{\epsilon_{IR}}\right)\frac{\mathcal{R}_8[^1S_0]}{M^2}.\end{aligned} \tag{B.27}$$

3.corrections from diagrams (Fig. 2.3 d-g)

$$\begin{aligned}\mathcal{M}_{trans} &= 2\left(\frac{2\alpha_s}{3\pi M^2}\right)\left(\frac{1}{\epsilon_{UV}}-\frac{1}{\epsilon_{IR}}\right)\\ &\quad \vec{v}\cdot\vec{v'}\left(C_F\left(\frac{1}{\sqrt{N_c}}\otimes\frac{1}{\sqrt{N_c}}\right)+\frac{N_c^2-4}{4N_c}\left(\sqrt{2}T^a\otimes\sqrt{2}T^a\right)\right)\left(\frac{1}{\sqrt{2}}\otimes\frac{1}{\sqrt{2}}\right)\\ &= \left(\frac{4\alpha_s}{3\pi M^2}\right)\left(\frac{1}{\epsilon_{UV}}-\frac{1}{\epsilon_{IR}}\right)\left(C_F\mathcal{O}_1[^1P_1]+B_F\mathcal{O}_8[^1P_1]\right).\end{aligned} \tag{B.28}$$

Adding these three contributions we get

$$\begin{aligned}\mathcal{O}_8^{(1)}[^1S_0] &= \frac{4\alpha_s}{3\pi M^2}\left(\frac{1}{\epsilon_{UV}}-\frac{1}{\epsilon_{IR}}\right)\\ &\times \left(C_F\mathcal{O}_1[^1P_1]+B_F\mathcal{O}_8[^1P_1]-\frac{N_c^2-2}{4N_c}\mathcal{R}_8[^1S_0]\right).\end{aligned} \tag{B.29}$$

- Corrections to $\mathcal{O}_1[^3S_1]$

$$\mathcal{O}_1[^3S_1]=\left(\frac{1}{\sqrt{N_c}}\otimes\frac{1}{\sqrt{N_c}}\right)\left(\frac{\boldsymbol{\sigma}}{\sqrt{2}}\otimes\frac{\boldsymbol{\sigma}}{\sqrt{2}}\right). \tag{B.30}$$

We again have contributions like

1. self-energy type corrections (Fig. 2.1 a,b)

$$\begin{aligned}\mathcal{M}_{self} &= 4\left(-\frac{2\alpha_s}{3\pi}\right)v^2 C_F\frac{1}{4}\left(\frac{1}{\epsilon_{UV}}-\frac{1}{\epsilon_{IR}}\right)\left(\frac{1}{\sqrt{N_c}}\otimes\frac{1}{\sqrt{N_c}}\right)\left(\frac{\boldsymbol{\sigma}}{\sqrt{2}}\otimes\frac{\boldsymbol{\sigma}}{\sqrt{2}}\right)\\ &= C_F\left(-\frac{2\alpha_s}{3\pi}\right)\left(\frac{1}{\epsilon_{UV}}-\frac{1}{\epsilon_{IR}}\right)\frac{\mathcal{R}_1[^3S_1]}{M^2}.\end{aligned} \tag{B.31}$$

2. Coulomb-like diagrams (Fig. 2.3 b,c)

$$\begin{aligned}\mathcal{M}_{coul} &= 2\left(-\frac{2\alpha_s}{3\pi}\right)v^2 C_F\frac{1}{2}\left(\frac{1}{\epsilon_{UV}}-\frac{1}{\epsilon_{IR}}\right)\left(\frac{1}{\sqrt{N_c}}\otimes\frac{1}{\sqrt{N_c}}\right)\left(\frac{\boldsymbol{\sigma}}{\sqrt{2}}\otimes\frac{\boldsymbol{\sigma}}{\sqrt{2}}\right)\\ &= C_F\left(-\frac{2\alpha_s}{3\pi}\right)\left(\frac{1}{\epsilon_{UV}}-\frac{1}{\epsilon_{IR}}\right)\frac{\mathcal{R}_1[^3S_1]}{M^2}. \qquad \text{(B.32)}\end{aligned}$$

3. diagrams (Fig. 2.3 d-g)

$$\begin{aligned}\mathcal{M}_{trans} &= 4\left(\frac{2\alpha_s}{3\pi}\right)\vec{v}\cdot\vec{v'}\frac{1}{4N_c}\left(\frac{1}{\epsilon_{UV}}-\frac{1}{\epsilon_{IR}}\right)\left(\sqrt{2}T^a\otimes\sqrt{2}T^a\right)\left(\frac{\boldsymbol{\sigma}}{\sqrt{2}}\otimes\frac{\boldsymbol{\sigma}}{\sqrt{2}}\right)\\ &= \left(\frac{2\alpha_s}{3\pi N_c}\right)\left(\frac{1}{\epsilon_{UV}}-\frac{1}{\epsilon_{IR}}\right)\frac{\sum_j\mathcal{O}_8[^3P_j]}{M^2}. \qquad \text{(B.33)}\end{aligned}$$

The sum of the latter gives

$$\mathcal{O}_1^{(1)}[^3S_1]=\left(\frac{2\alpha_s}{3\pi M^2}\right)\left(\frac{1}{\epsilon_{UV}}-\frac{1}{\epsilon_{IR}}\right)\left(\frac{1}{N_c}\sum_j\mathcal{O}_8[^3P_j]-2C_F\mathcal{R}_1[^3S_1]\right). \qquad \text{(B.34)}$$

- corrections to $\mathcal{O}_8[^3S_1]$:

$$\mathcal{O}_8[^3S_1]=\left(\sqrt{2}T^a\sqrt{2}T^a\right)\left(\frac{\boldsymbol{\sigma}}{\sqrt{2}}\otimes\frac{\boldsymbol{\sigma}}{\sqrt{2}}\right). \qquad \text{(B.35)}$$

The three types of contributions are

1. self-energy type corrections (Fig. 2.2 a,b)

$$\begin{aligned}\mathcal{M}_{self} &= 4\left(-\frac{2\alpha_s}{3\pi}\right)v^2C_F\frac{1}{4}\left(\frac{1}{\epsilon_{UV}}-\frac{1}{\epsilon_{IR}}\right)\left(\sqrt{2}T^a\otimes\sqrt{2}\right)\left(\frac{\boldsymbol{\sigma}}{\sqrt{2}}\otimes\frac{\boldsymbol{\sigma}}{\sqrt{2}}\right)\\ &= C_F\left(-\frac{2\alpha_s}{3\pi}\right)\left(\frac{1}{\epsilon_{UV}}-\frac{1}{\epsilon_{IR}}\right)\frac{\mathcal{R}_8[^3S_1]}{M^2}. \qquad \text{(B.36)}\end{aligned}$$

2. Coulomb-like diagrams (Fig. 2.2 b,c)

$$\begin{aligned}\mathcal{M}_{coul} &= 2\left(-\frac{2\alpha_s}{3\pi}\right)v^2\left(-\frac{1}{2N_c}\right)\frac{1}{2}\left(\frac{1}{\epsilon_{UV}}-\frac{1}{\epsilon_{IR}}\right)\left(\sqrt{2}T^a\otimes\sqrt{2}T^a\right)\left(\frac{\boldsymbol{\sigma}}{\sqrt{2}}\otimes\frac{\boldsymbol{\sigma}}{\sqrt{2}}\right)\\ &= \left(-\frac{1}{2N_c}\right)\left(-\frac{2\alpha_s}{3\pi}\right)\left(\frac{1}{\epsilon_{UV}}-\frac{1}{\epsilon_{IR}}\right)\frac{\mathcal{R}_8[^3S_1]}{M^2}. \qquad \text{(B.37)}\end{aligned}$$

3. diagrams (Fig. 2.2 d-g)

$$\begin{aligned}\mathcal{M}_{trans} &= 2\left(\frac{2\alpha_s}{3\pi M^2}\right)\left(\frac{1}{\epsilon_{UV}}-\frac{1}{\epsilon_{IR}}\right)\\ &\quad \vec{v}\cdot\vec{v'}\left(C_F\left(\frac{1}{\sqrt{N_c}}\otimes\frac{1}{\sqrt{N_c}}\right)+\frac{N_c^2-4}{4N_c}\left(\sqrt{2}T^a\otimes\sqrt{2}T^a\right)\right)\left(\frac{\boldsymbol{\sigma}}{\sqrt{2}}\otimes\frac{\boldsymbol{\sigma}}{\sqrt{2}}\right)\\ &= \left(\frac{4\alpha_s}{3\pi M^2}\right)\left(\frac{1}{\epsilon_{UV}}-\frac{1}{\epsilon_{IR}}\right)\left(C_F\sum_j\mathcal{O}_1[^3P_j]+B_F\sum_j\mathcal{O}_8[^3P_j]\right). \qquad \text{(B.38)}\end{aligned}$$

The order α_s corrections to the operator $\mathcal{O}_8^{(1)}[^3S_1]$ are

$$\mathcal{O}_8^{(1)}[^3S_1] = \frac{4\alpha_s}{3\pi M^2}\left(\frac{1}{\epsilon_{UV}}-\frac{1}{\epsilon_{IR}}\right) \left(C_F\sum_j \mathcal{O}_1[^3P_j] + B_F\sum_j \mathcal{O}_8[^1P_1] - \frac{N_c^2-2}{4N_c}\mathcal{R}_8[^3S_1]\right). \quad \text{(B.39)}$$

Appendix C

Scalar integrals

(i) The scalar one-point function is given by

$$A_0(m) = \mu^{4-n} \int \frac{d^n q}{(2\pi)^n} \frac{1}{[q^2 - m^2]} = iC_\varepsilon m^2 \left[\frac{1}{\varepsilon} + 1\right], \tag{C.1}$$

where

$$C_\varepsilon = \frac{1}{16\pi^2} \exp(-\varepsilon(\gamma_E - \ln 4\pi)) \left(\frac{\mu^2}{m^2}\right)^\varepsilon. \tag{C.2}$$

(ii) The scalar two-point function is defined as

$$B_0(p^2, m_1, m_2) = \mu^{4-n} \int \frac{d^n q}{(2\pi)^n} \frac{1}{[q^2 - m_1^2][(q+p)^2 - m_2^2]}. \tag{C.3}$$

The two-point functions required in the computations of the virtual corrections are given by

$$\begin{aligned}
B_0(t, 0, 0) &= iC_\varepsilon \left[\frac{1}{\varepsilon} - \ln\left(-\frac{t}{m^2}\right) + 2\right], \\
B_0(m^2, 0, m) &= B_0(4m^2, m, m) = iC_\varepsilon \left[\frac{1}{\varepsilon} + 2\right], \\
B_0(m^2 + \frac{t_1}{2}, 0, m) &= iC_\varepsilon \left[\frac{1}{\varepsilon} + 2 - \frac{t_1}{t_1 + 2m^2} \ln\left(-\frac{t_1}{2m^2}\right)\right], \\
B_0(s, m, m) &= iC_\varepsilon \left[\frac{1}{\varepsilon} + 2 + \beta \ln\left(\frac{1-\beta}{1+\beta}\right)\right],
\end{aligned} \tag{C.4}$$

where $\beta \equiv \beta(s) = \sqrt{1 - 4m^2/s}$,

$$\begin{aligned}
B_0(0, 0, 0) &= iC_\varepsilon \left(\frac{1}{\varepsilon_{UV}} - \frac{1}{\varepsilon_{IR}}\right) \\
&= \frac{1}{16\pi^2} \left[\left(\frac{1}{\varepsilon_{UV}} - \gamma_E + \ln(4\pi)\right) - \left(\frac{1}{\varepsilon_{IR}} - \gamma_E + \ln(4\pi)\right)\right].
\end{aligned} \tag{C.5}$$

It can be shown that the last integral can be consistently set to zero [63], but it means that the UV- and IR-poles are identified. In order to make separate checks of UV- and IR-finiteness possible we should distinguish between them.

(iii) The scalar three-point function is defined as

$$C_0(p_1^2,(p_2-p_1)^2,p_2^2,m_1,m_2,m_3) = \mu^{4-n}\int \frac{d^nq}{(2\pi)^n}\frac{1}{[q^2-m_1^2][(q+p_1)^2-m_2^2][(q+p_2)^2-m_3^2]}. \tag{C.6}$$

The useful types for our calculations are

$$\begin{aligned}
C_0(0,t,0,0,0,0) &= iC_\varepsilon\frac{1}{t}\left[\frac{1}{\varepsilon^2}-\frac{1}{\varepsilon}\ln\left(-\frac{t}{m^2}\right)+\frac{1}{2}\ln^2\left(-\frac{t}{m^2}\right)-\frac{1}{2}\zeta(2)\right],\\
C_0(0,m^2+\frac{s_1}{2},m^2+\frac{t_1}{2},0,0,0) &= iC_\varepsilon\frac{2}{s_1-t_1}\left[\frac{1}{\varepsilon}\ln\left(\frac{s_1+2m^2}{t_1+2m^2}\right)-\frac{1}{2}\ln^2\left(\frac{s_1+2m^2}{t_1+2m^2}\right)\right],\\
C_0(0,m^2,m^2+\frac{s_1}{2},0,0,m) &= iC_\varepsilon\frac{1}{s_1}\left[\frac{1}{\varepsilon^2}-\frac{2}{\varepsilon}\ln\left(-\frac{s_1}{2m^2}\right)\right.\\
&\quad \left.+2\ln^2\left(-\frac{s_1}{2m^2}\right)+2Li_2\left(\frac{s_1+2m^2}{2m^2}\right)+\frac{1}{2}\zeta(2)\right],\\
C_0(t,m^2+\frac{t_1}{2},m^2,0,0,m) &= iC_\varepsilon\frac{1}{t_1}\left[\frac{1}{2}\ln^2\left(-\frac{t}{2m^2}\right)+Li_2\left(1-\frac{2m^2}{t}\right)\right.\\
&\quad \left.+Li_2\left(\frac{t}{4m^2}\right)-Li_2\left(-\frac{2(2m^2-t)}{t}\right)+\frac{5}{2}\zeta(2)\right],\\
C_0(0,m^2+\frac{t_1}{2},m^2+\frac{u_1}{2},0,0,m) &= iC_\varepsilon\frac{2}{u_1-t_1}\left[\frac{1}{\varepsilon}\ln\left(\frac{t_1}{u_1}\right)+\frac{1}{2}\ln^2\left(\frac{-u_1}{2m^2}\right)-\frac{1}{2}\ln^2\left(\frac{-t_1}{2m^2}\right)\right.\\
&\quad \left.+Li_2\left(1+\frac{2m^2}{t_1}\right)-Li_2\left(1+\frac{2m^2}{u_1}\right)\right],\\
C_0(0,0,s,m,m,m) &= -iC_\varepsilon\frac{1}{s}\left[Li_2\left(\frac{2}{1+\beta}\right)+Li_2\left(\frac{2}{1-\beta}\right)\right],
\end{aligned} \tag{C.7}$$

where $\zeta(2)=\pi^2/6$.

(iv) The scalar four-point function is defined as

$$\begin{aligned}
&D_0(p_1^2,(p_2-p_1)^2,(p_3-p_2)^2,p_3^2,p_2^2,(p_3-p_1)^2,m_1,m_2,m_3,m_4) =\\
&\mu^{4-n}\int\frac{d^nq}{(2\pi)^n}\frac{1}{[q^2-m_1^2][(q+p_1)^2-m_2^2][(q+p_2)^2-m_3^2][(q+p_3)^2-m_4^2]}.
\end{aligned} \tag{C.8}$$

We have used different types of four-point functions and those containing divergences are

$$
\begin{aligned}
&D_0(0,0,4m^2,0,s,u,0,0,0,0)\\
&= iC_\varepsilon \frac{1}{su}\Big\{\frac{2}{\varepsilon^2} - \frac{2}{\varepsilon}\Big[\ln\left(\frac{s}{4m^2}\right) + \ln\left(\frac{u}{4m^2}\right)\Big] + 2\Big[Li_2\left(-\frac{t}{u_1}\right) + Li_2\left(-\frac{t}{s_1}\right) - Li_2\left(\frac{t4m^2}{s_1u_1}\right)\Big]\\
&+\Big[\ln^2\left(\frac{su}{4m^2u_1}\right) + \ln^2\left(\frac{su}{4m^2s_1}\right) - \ln^2\left(-\frac{su}{s_1u_1}\right)\Big] - \zeta(2)\Big\},\\
&D_0(0,t,m^2+\frac{t_1}{2},m^2+\frac{u_1}{2},0,m^2,0,0,0,m)\\
&= iC_\varepsilon \frac{1}{tu_1}\Big\{\frac{3}{2}\frac{1}{\varepsilon^2} - \frac{1}{\varepsilon}\Big[2\ln\left(\frac{-u_1}{2m^2}\right) - \ln\left(\frac{-t_1}{2m^2}\right) + \ln\left(\frac{-t}{m^2}\right)\Big]\\
&+2\ln\left(\frac{-u_1}{2m^2}\right)\ln\left(\frac{-t}{m^2}\right) - \ln^2\left(\frac{-t_1}{2m^2}\right) - 2Li_2\left(1-\frac{t_1}{u_1}\right) - \frac{13}{4}\zeta(2)\Big\},\\
&D_0(0,m^2,0,m^2+\frac{u_1}{2},m^2+\frac{s_1}{2},m^2+\frac{t_1}{2},0,0,m,m)\\
&= iC_\varepsilon \frac{1}{s_1t_1}\Big\{\frac{1}{\varepsilon^2} + \frac{2}{\varepsilon}\Big[\ln\left(\frac{-u_1}{2m^2}\right) - \ln\left(\frac{-t_1}{2m^2}\right) - \ln\left(\frac{-s_1}{2m^2}\right)\Big] + 2\ln^2\left(\frac{-s_1}{2m^2}\right) + 2\ln^2\left(\frac{-t_1}{2m^2}\right)\\
&-2\ln^2\left(\frac{-u_1}{2m^2}\right) + 4Li_2\left(\frac{u_1-s_1}{s_1}\right) - 4Li_2\left(\frac{u_1-t_1}{s_1}\frac{u_1-s_1}{t_1}\right) - \frac{3}{2}\zeta(2)\Big\},\\
&D_0(m^2,0,0,m^2+\frac{s_1}{2},m^2+\frac{t_1}{2},s,0,m,m,m)\\
&= iC_\varepsilon \frac{1}{t_1s}\frac{4}{\lambda}\Big\{Li_2\left(\frac{\lambda-1}{\lambda+\beta}\right) + Li_2\left(\frac{\lambda-1}{\lambda-\beta}\right)Li_2\left(\frac{\lambda+1}{\lambda+\beta}\right) - Li_2\left(\frac{\lambda+1}{\lambda-\beta}\right)\Big\},
\end{aligned}
\tag{C.9}
$$

where $\lambda \equiv \lambda(s_1,t_1) = \sqrt{\frac{s_1}{s_1+4m^2}\frac{t_1+4m^2}{t_1}}$.

C.1 Abelian five-point integrals

The five-point scalar integrals that we need for our computations are of the type

$$
\begin{aligned}
&E_0(p_c, p_c-k_1, p_c-k_1-k_2, p_{\bar{c}}, 0, m, m, m, m) =\\
&\mu^{4-n}\int \frac{d^nq}{(2\pi)^n}\frac{1}{[q^2][(q+p_c)^2-m^2][(q-p_{\bar{c}})^2-m^2]}\\
&\times\frac{1}{[(q+p_c-k_1)^2-m^2][(q+p_c-k_1-k_2)^2-m^2]}.
\end{aligned}
\tag{C.10}
$$

The Abelian scalar five-point functions are UV-finite, but IR- and Coulomb-divergent. Their singular pieces are determined by the small momentum integration region $q \to 0$. The structure of the divergences can be extracted neglecting the loop momentum in the

IR-finite propagators. It is easy to see that in this limit we get an IR-divergent scalar three-point function multiplied with the remaining IR-finite propagators. As regularization scheme we can use dimensional regularization and the poles arise as $1/\epsilon_{IR}$. We can also assign a mass to the photon (gluon) and the IR-divergences appears as $1/m_\lambda$, where λ is the photon mass. The finite part of the scalar five-point functions should be the independent of the regularization scheme, so that we can write the equality:

$$E_0^{(fin)} = E_0^{(D)} - E_{div}^{(D)} = E_0^{(\lambda)} - E_{div}^{(\lambda)}, \tag{C.11}$$

where the superscript (D) or (λ) refer to dimensional- and respectively mass-regularization scheme. The generic type of useful scalar three-point function is
$C_0(p_c, -p_{\overline{c}}, 0, m, m) \leftrightarrow C_0(p, -p, \lambda, m, m)$, where

$$C_0(p_c, -p_{\overline{c}}, 0, m, m) = -iC_\varepsilon \frac{1}{2m^2}\left[\frac{1}{\varepsilon_{IR}} + \frac{\pi^2}{2v} - 2\right]. \tag{C.12}$$

where we have chosen the small relative velocity v as an IR-regulator, defined by
$|\mathbf{p_c} - \mathbf{p_{\overline{c}}}| = 2mv$. If we assign a small mass λ to the photon, then the above mentioned scalar three-point function can be expressed as

$$C_0(p, -p, \lambda, m, m) = -iC_\varepsilon \frac{1}{2m^2}\left[\ln\left(\frac{\lambda^2}{m^2}\right) + \frac{2\pi}{\lambda}m - 2\right]. \tag{C.13}$$

It is obvious that we can make the correspondence

$$\begin{aligned} \ln\left(\frac{\lambda^2}{m^2}\right) &\iff \frac{1}{\varepsilon_{IR}} \text{ (IR-singularity)}, \\ \frac{2\pi}{\lambda}m &\iff \frac{\pi^2}{2v} \text{ (Coulomb-singularity)}. \end{aligned} \tag{C.14}$$

In our computation we encounter also Coulomb-divergent four-point functions of the form $D_0(p_c, p_c - k_1, -p_{\overline{c}}, 0, m, m, m)$, whose divergent parts are

$$D_0^{(IR)}(-p_c, p_c - k_1, -p_{\overline{c}}, 0, m, m, m) = \frac{1}{\left[(p_c - k_1)^2 - m^2\right]} C_0(p_c, -p_{\overline{c}}, 0, m, m), \tag{C.15}$$

and whose finite parts can be expressed as $D_0^{(fin)} = D_0 - D_0^{IR}$. If we use v as a regulator, we obtain [14] :

$$\begin{aligned} & D_0^{(fin)}(p_c, p_c - k_1, -p_{\overline{c}}, 0, m, m, m) \\ \equiv\ & D_0(p_c, p_c - k_1, -p_{\overline{c}}, 0, m, m, m) - \frac{1}{\left[(p_c - k_1)^2 - m^2\right]} C_0(p_c, -p_{\overline{c}}, 0, m, m) \\ =\ & iC_\varepsilon \frac{2}{t_1 m^2}\left[\frac{1}{\beta(t)} \ln\left(\frac{1-\beta(t)}{1+\beta(t)}\right) - \ln\left(\frac{2m^2}{t_1}\right)\right]. \end{aligned} \tag{C.16}$$

The singularity structure of the scalar five-point functions is easy to be obtained considering the IR-limit. The finite part defined as

$$\begin{aligned} & E_0^{(fin)}(p_c, p_c - k_1, p_c - k_1 - k_2, p_{\overline{c}}, 0, m, m, m, m) \equiv \\ & \quad E_0(p_c, p_c - k_1, p_c - k_1 - k_2, p_{\overline{c}}, 0, m, m, m, m) \\ & - \frac{1}{\left[(p_c - k_1)^2 - m^2\right]\left[(p_c - k_1 - k_2)^2 - m^2\right]} C_0(p_c, -p_{\overline{c}}, 0, m, m) \end{aligned} \tag{C.17}$$

can be analytically obtained using the relative velocity v [14] or the photon mass λ as a regulator. We have chosen the second method and compare our analytical result with Ref. [64]. Since the expression is rather large, we present here only the technique of the calculation.
Using the equality

$$\begin{aligned} & \frac{1}{[q^2 - \lambda^2][(q+p)^2 - m^2][(q-p)^2 - m^2]} \times \frac{1}{[(q+p-k_1)^2 - m^2][(q+p-k_1-k_2)^2 - m^2]} \\ = \; & \frac{1}{2\lambda^2}\left(\frac{1}{[q^2 - \lambda^2]} - \frac{1}{[q^2]}\right)\left(\frac{1}{[(q+p)^2 - m^2]} - \frac{1}{[(q-p)^2 - m^2]}\right) \\ \times \; & \frac{1}{[(q+p_c-k_1)^2 - m^2][(q+p_c-k_1-k_2)^2 - m^2]}, \end{aligned} \tag{C.18}$$

the scalar five-point function can be expressed as

$$\begin{aligned} & E_0(p, p - k_1, p - k_1 - k_2, -p, \lambda, m, m, m, m) = \frac{1}{2\lambda^2} \\ & \times [D_0(p, p - k_1, p - k_1 - k_2, \lambda, m, m, m) - D_0(p, p - k_1, p - k_1 - k_2, 0, m, m, m) \\ & + D_0(p, p + k_3, p + k_3 - k_2, \lambda, m, m, m) - D_0(p, p + k_3, p + k_3 - k_2, 0, m, m, m)]. \end{aligned} \tag{C.19}$$

To get the divergent and finite parts of the E_0 we have expressed the sum of D_0 functions on the right hand side of the last equation as a power expansion in λ^2 up to $\mathcal{O}(\lambda^4)$. For the analytical expression of D_0 functions we have used the formulation outlined in [65]. For the divergent part of E_0 we get

$$\begin{aligned} & E_0^{IR}(p, p - k_1, p - k_1 - k_2, -p, \lambda, m, m, m, m) \\ = \; & \frac{4}{t_1 s_1} C_0(p, -p, \lambda, m, m) \\ = \; & \frac{4}{t_1 s_1}\left\{-iC_\varepsilon \frac{1}{2m^2}\left[\ln\frac{\lambda^2}{m^2} + \frac{2\pi m}{\lambda} - 2\right]\right\}. \end{aligned} \tag{C.20}$$

The five-point tensor integrals are defined as

$$E_{\alpha,\alpha\beta,\alpha\beta\gamma,\alpha\beta\gamma\delta}(p_c, p_c - k_1, p_c - k_1 - k_2, p_{\bar{c}}, 0, m, m, m, m) = \mu^{4-n} \int \frac{d^n q}{(2\pi)^n} \frac{q_\alpha, q_\alpha q_\beta, q_\alpha q_\beta q_\gamma, q_\alpha q_\beta q_\gamma q_\delta}{[q^2][(q+p_c)^2 - m^2][(q-p_{\bar{c}})^2 - m^2]} \times \frac{1}{[(q+p_c-k_1)^2 - m^2][(q+p_c-k_1-k_2)^2 - m^2]}. \quad \text{(C.21)}$$

They are IR- and Coulomb-finite, so that the tensor reduction can be performed at $v = 0$ and $\lambda = 0$ respectively. The IR- and Coulomb-singularities are contained only in C_0, D_0, E_0 that emerge from the tensor reduction. Since we have only three linearly independent external momenta, we have performed the Passarino-Veltman [66] reduction only for special cases, it i.e. those required in our computations of virtual corrections. So that we have dealt with scalar products in the numerators of the tensor integrals instead of n-dimensional vector components.

Using the linear dependence of the external momenta we can express the scalar products appearing in the reduction of the five-point tensor integrals considered before as:

$$\begin{aligned} q \cdot p &= \frac{1}{4}\{[(q+p)^2 - m^2] - [(q-p)^2 - m^2]\}, \\ q \cdot k_1 &= \frac{1}{2}\{[(q+p)^2 - m^2] - [(q+p-k_1)^2 - m^2] + t_1/2\}, \\ q \cdot k_2 &= \frac{1}{2}\{[(q+p-k_1)^2 - m^2] - [(q+p-k_1-k_2)^2 - m^2] + (u_1/2 + s_1)\}. \end{aligned} \quad \text{(C.22)}$$

It is trivial to show that all five-point tensor integrals reduce to four-point and lower tensor integrals and scalar five-point functions. To reduce the two-, three- and four-point tensor integrals we have used Mathematica package FeynCalc [67]. As a check we have implemented the Passarino-Veltman reduction as described in Ref.[68] in a FORM [69] routine.

C.2 Non-Abelian five-point integrals

An example of Feynman pentagon diagrams containing non-Abelian vertices was shown in Fig. 4.11 . We refer to the involved five-point integrals as non-Abelian five-point functions. Due to the structure of triple gluon vertices, we can easily reduce the five-point integrals to a set of lower n-point functions. In our particular computations we have only one type of non-Abelian five-point function, since the two diagrams differ only by the fermion flow in the heavy quark lines. Using the simple algebraic relation

$$\frac{1}{[q^2][(q+k_3)^2][(q+k_3+p)^2 - m^2][(q-p)^2 - m^2][(q+k_1-p)^2 - m^2]}$$

$$
\begin{aligned}
&= \frac{2}{s_1}\Big\{\frac{1}{[q^2][(q+k_3)^2][(q+k_3+p)^2-m^2][(q+k_1-p)^2-m^2]} \\
&+ \frac{1}{[q^2][(q+k_3)^2][(q-p)^2-m^2][(q+k_1-p)^2-m^2]} \\
&- \frac{1}{[q^2][(q+k_3+p)^2][(q-p)^2-m^2][(q+k_1-p)^2-m^2]} \\
&- \frac{1}{[(q+k_3)^2][(q+k_3+p)^2][(q-p)^2-m^2][(q+k_1-p)^2-m^2]}\Big\}, \qquad \text{(C.23)}
\end{aligned}
$$

it is easy to see that this type of five-point function can be reduced to a set of four four-point integrals. These are usually known, and the D_0, C_0, B_0 required in this computation are listed in the last subsection. For the scalar five-point function we have

$$
\begin{aligned}
&E_0[k_3, p+k_3, k_1-p, -p, 0, 0, m, m, m,] = \\
&\frac{2}{s_1}\Big\{D_0[k_3, p+k_3, k_1-p, 0, 0, m, m,] + D_0[k_3, -p, k_1-p, 0, 0, m, m] \\
&-D_0[p+k_3, k_1-p, -p, 0, m, m, m] - D_0[p+k_3, k_2-p, -p, 0, m, m, m]\Big\}. \qquad \text{(C.24)}
\end{aligned}
$$

The resulting D_0-functions contain IR- and are free from UV- and Coulomb-singularities.

Appendix D

Angular integrals

Here we give the angular integrals that arise in our computations [70]

$$I_n^{(k,m)} = \int_0^\pi d\,\theta \sin^{n-3}\theta \int_0^\pi d\,\phi \sin^{n-4}\phi (a + b\cos\theta)^{-k}(A + B\cos\theta + C\sin\theta\cos\phi)^{-m} \quad \text{(D.1)}$$

where $n = 4 - 2\epsilon$, $a \neq b$, and $A^2 \neq B^2 + C^2$:

$$\begin{aligned}
I_n^{(0,0)} &= 2\pi(1 + 2\varepsilon + 4\varepsilon^2), && \text{(D.2)}\\
I_n^{(-1,0)} &= 2\pi a(1 + 2\varepsilon + 4\varepsilon^2), && \text{(D.3)}\\
I_n^{(0,-1)} &= 2\pi A(1 + 2\varepsilon + 4\varepsilon^2), && \text{(D.4)}\\
I_4^{(1,0)} &= \frac{\pi}{b}\ln\frac{a+b}{a-b}, && \text{(D.5)}\\
I_n^{(0,1)} &= \frac{2\pi}{\sqrt{B^2+C^2}}\Big\{\ln\Big(\frac{A+\sqrt{B^2+C^2}}{A-\sqrt{B^2+C^2}}\Big) && \text{(D.6)}\\
&- \varepsilon\Big[Li_2\Big(\frac{2\sqrt{B^2+C^2}}{\sqrt{B^2+C^2}-A}\Big) + Li_2\Big(\frac{2\sqrt{B^2+C^2}}{\sqrt{B^2+C^2}+A}\Big)\Big]\Big\},\\
I_n^{(-1,-1)} &= 2\pi\left[\left(aA + \frac{1}{3}bB\right) + 2\varepsilon\left(aA + \frac{4}{9}bB\right)\right], && \text{(D.7)}\\
I_n^{(0,2)} &= 2\pi\frac{1}{A^2 - B^2 - C^2}\left[1 + \varepsilon\frac{A}{\sqrt{B^2+C^2}}\ln\frac{A+\sqrt{B^2+C^2}}{A-\sqrt{B^2+C^2}}\right], && \text{(D.8)}\\
I_n^{(0,-2)} &= 2\pi\left[A^2(1+2\varepsilon) + \frac{1}{3}\left(B^2+C^2\right)\left(1 + \frac{8}{3}\varepsilon\right)\right], && \text{(D.9)}\\
I_n^{(-2,0)} &= 2\pi\left[a^2(1+2\varepsilon) + \frac{1}{3}\,b^2\,\left(1 + \frac{8}{3}\varepsilon\right)\right]. && \text{(D.10)}
\end{aligned}$$

Useful mathematical formulae

For computing the above listed angular integrals we have used the folowing relation [71]

$$\int_0^{\pi/2} \frac{\sin^\mu x \cos^\nu x}{(a - b\cos^2 x)^\rho} dx = \frac{1}{2a^\rho} B\left(\frac{\mu+1}{2}, \frac{\nu+1}{2}\right) F_1\left(\frac{\nu+1}{2}, \rho, \frac{\mu+\nu}{2}+1; \frac{b}{a}\right), \quad \text{(D.11)}$$

where $B(a,b) = \frac{\Gamma(a)\,\Gamma(b)}{\Gamma(a+b)}$ [so called Beta-function], with $\Gamma(z)$ defined by

$$\Gamma(z) = \int_0^\infty \exp^{-t} t^{z-1} dt \;\; , Re(z) > 0, \quad \text{(D.12)}$$

and $F_1(a,b,c;z)$ is the hypergeometric function. The hypergeometric series is definied by

$$F_1(a,b,c;z) = 1 + \frac{a\cdot b}{c\cdot 1} z + \frac{a(a+1)\cdot b(b+1)}{c(c+1)\cdot 1\cdot 2} z^2 + \cdots \quad \text{(D.13)}$$

In our calculations we need to expand the results of angular integrals up to order ϵ^2. The hypergeometric functions encountered in our computations are

$$\begin{aligned}
F_1\left(\frac{1}{2}, 1, \frac{1}{2} - \epsilon, z^2\right) &= \frac{1}{1-z^2}\Big[1 + \epsilon \cdot z \log\left(\frac{z+1}{1-z}\right) \\
&\quad -\epsilon^2 \cdot z \left(Li_2\left[\frac{2z}{z-1}\right] - Li_2\left[\frac{2z}{z+1}\right]\right) + \mathcal{O}(\epsilon^3)\Big], \quad \text{(D.14)} \\
F_1\left(\frac{1}{2}, 1, \frac{3}{2} - \epsilon, z^2\right) &= \frac{1}{2z}\Big[\log\left(\frac{z+1}{1-z}\right) - 2\epsilon \log\left(\frac{z+1}{1-z}\right) \\
&\quad -\epsilon \left(Li_2\left[\frac{2z}{z-1}\right] - Li_2\left[\frac{2z}{z+1}\right]\right) + \mathcal{O}(\epsilon^2)\Big], \quad \text{(D.15)} \\
F_1\left(\frac{3}{2}, 1, \frac{3}{2} - \epsilon, z^2\right) &= (1-2\epsilon) F_1\left(\frac{1}{2}, 1, \frac{1}{2} - \epsilon, z^2\right) \\
&\quad +2\epsilon\, F_1\left(\frac{1}{2}, 1, \frac{3}{2} - \epsilon, z^2\right). \quad \text{(D.16)}
\end{aligned}$$

[For more details see Ref. [72]].

Bibliography

[1] G. T. Bodwin, E. Braaten and G. P. Lepage, Phys. Rev. D **51**, 1125 (1995) [Erratum-*ibid.* **55**, 5853 (1997)];
G. T. Bodwin, E. Braaten and G. P. Lepage, Phys. Rev. D **46**, 1914 (1992).

[2] E. L. Berger and D. L. Jones, Phys. Rev. D **23**, 1521 (1981).

[3] R. Baier and R. Ruckl, Z. Phys. C **19**, 251 (1983).

[4] E. Braaten and S. Fleming, Phys. Rev. Lett. **74**, 3327 (1995);
E. Braaten and T. C. Yuan, Phys. Rev. D **52**, 6627 (1995).

[5] P. L. Cho and A. K. Leibovich, Phys. Rev. D **53**, 150 (1996);*ibid.*, 6203 (1996).

[6] CDF Collaboration, F. Abe *et al.*, Phys. Rev. Lett. **69**, 3704 (1992);*ibid.* **71**, 2537 (1993); *ibid.***79**, 572 (1997);*ibid.* **79**, 578 (1997);
D0 Collaboration, S. Abachi *et al.*, Phys. Lett. B **370**, 239 (1996);
D0 Collaboration, B. Abbott *et al.*, Phys. Rev. Lett. **82**, 35 (1999).

[7] M. Klasen, B. A. Kniehl, L. N. Mihaila and M. Steinhauser, Phys. Rev. Lett. **89**, 032001 (2002).

[8] Š. Todorova-Nová, Report No. hep-ph/0112050, in *Proceedings of the XXXI International Symposium on Multiparticle Dynamics*, Datong, China, 1–7 September 2001 (World Scientific, Singapore, to appear); M. Chapkin, talk presented at *7th International Workshop on Meson Production, Properties and Interaction (Meson 2002)*, Krakow, Poland, 24–28 May 2002 and private communication.

[9] M. Krämer, Prog. Part. Nucl. Phys. **47**, 141 (2001).

[10] M. Klasen, arXiv:hep-ph/0206169.

[11] M. Beneke, M. Krämer and M. Vänttinen, Phys. Rev. D **57**, 4258 (1998).

[12] S. Fleming, I. Z. Rothstein and A. K. Leibovich, Phys. Rev. D **64**, 036002 (2001).

[13] E. Braaten, B. A. Kniehl and J. Lee, Phys. Rev. D **62**, 094005 (2000).

[14] M. Krämer, Nucl. Phys. B **459**, 3 (1996);
M. Krämer, J. Zunft, J. Steegborn and P. M. Zerwas, Phys. Lett. B **348**, 657 (1995).

[15] A. Petrelli, M. Cacciari, M. Greco, F. Maltoni and M. L. Mangano, Nucl. Phys. B **514**, 245 (1998).

[16] F. Maltoni, M. L. Mangano and A. Petrelli, Nucl. Phys. B **519**, 361 (1998);
M. L. Mangano and A. Petrelli, Int. J. Mod. Phys. A **12**, 3887 (1997);
M. Cacciari, M. Greco, M. L. Mangano and A. Petrelli, Phys. Lett. B **356**, 553 (1995).

[17] H. Bethe and E.Salpeter, Quantum mechanics of one- and two-electron atoms (Plenum, New York, 1977), Chapter 1b.

[18] J. S. Schwinger, Proc. Nat. Acad. Sci. **37**, 452 (1951).

[19] E. E. Salpeter and H. A. Bethe, Phys. Rev. **84**, 1232 (1951).

[20] F.Gross, Phys. Rev. **186** (1969) 1448;
W. Caswell and P. Lepage, Phys. Rev. A**18** (1978) 810;
R. Barbieri and E. Remiddi, Phys. Nucl. B**141** (1978) 413.

[21] G. Bodwin, D. Yennie and M. Gregorio, Phys. Lett. **48** (1982) 1799; Rev. Mod. Phys. **57** (1985) 723.

[22] W. Caswell and P. Lepage, Phys. Lett. B**167** (1986) 437.

[23] T. Appelquist and H. Politzer, Phys. Rev. Lett. **34** (1975) 43;
A. De Rújula and S. Glashow, *ibid.* **34** (1975) 46.

[24] B. Humpert, Phys. Lett. B **184**, 105 (1987);
R. Gastmans, W. Troost and T. T. Wu, Nucl. Phys. B **291**, 731 (1987).

[25] W. Pauli and M. Fierz, Helv. Phys. Acta **12**, 297 (1939).

[26] R. Barbieri, M. Caffo and E.Remiddi, Phys. Lett. B**95** (1980) 93; Nucl. Phys. **B192** (1981) 61.

[27] G. P. Lepage, L. Magnea, C. Nakhleh, U. Magnea and K. Hornbostel, Phys. Rev. D **46**, 4052 (1992);
E. Braaten, arXiv:hep-ph/9702225;
A. V. Manohar and I. W. Stewart, Nucl. Phys. Proc. Suppl. **94**, 130 (2001);
A. V. Manohar and I. W. Stewart, Phys. Rev. Lett. **85**, 2248 (2000).
M. E. Luke and A. V. Manohar, Phys. Rev. D **55**, 4129 (1997);
A. V. Manohar,Phys. Rev. D **56**, 230 (1997).

[28] T. Kinoshita, J. Math. Phys. **3**, 650 (1962);
T. D. Lee and M. Nauenberg, Phys. Rev. **133**, B1549 (1964).

[29] J. H. Kühn, J. Kaplan and E. G. Safiani, Nucl. Phys. B **157**, 125 (1979);
B. Guberina, J. H. Kühn, R. D. Peccei and R. Ruckl, Nucl. Phys. B **174**, 317 (1980).

[30] E. Witten, Nucl. Phys. B **120**, 189 (1977).

[31] L. Stodolsky, Phys. Rev. Lett. **18**, 135 (1967);
E. Auge *et al.* [NA14 Collaboration], Phys. Lett. B **168**, 163 (1986).

[32] M. Drees and R. M. Godbole, J. Phys. G **21**, 1559 (1995).

[33] R. M. Godbole, D. Indumathi and M. Krämer, Phys. Rev. D **65**, 074003 (2002).

[34] C. F. von Weizsäcker, Z. Phys. **88**, 612 (1934);
E. J. Williams, Proc. R. Soc. London A **139**, 163 (1933).

[35] S. Frixione, M. L. Mangano, P. Nason and G. Ridolfi, Phys. Lett. B **319**, 339 (1993).

[36] M. Glück, E. Reya and I. Schienbein, Phys. Rev. D **64**, 017501 (2001).

[37] P. Ko, J. Lee and H. S. Song, Phys. Rev. D **54**, 4312 (1996).

[38] L. K. Hao, F. Yuan and K. T. Chao, Phys. Rev. Lett. **83**, 4490 (1999).

[39] M. Cacciari and M. Krämer, Phys. Rev. Lett. **76**, 4128 (1996);
J. Amundson, S. Fleming and I. Maksymyk, Phys. Rev. D **56**, 5844 (1997);
F. Maltoni, M. L. Mangano and A. Petrelli, Nucl. Phys. B **519**, 361 (1998);
S. Fleming and T. Mehen, Phys. Rev. D **58**, 037503 (1998).

[40] J. P. Ma, B. H. McKellar and C. B. Paranavitane, Phys. Rev. D **57**, 606 (1998).

[41] G. Japaridze and A. Tkabladze, Phys. Lett. B **433**, 139 (1998).

[42] M. Klasen, B. A. Kniehl, L. Mihaila and M. Steinhauser, Nucl. Phys. B **609**, 518 (2001).

[43] M. Cacciari, M. Greco and M. Krämer, Phys. Rev. D **55**, 7126 (1997).

[44] T. Mehen, Phys. Rev. D **55**, 4338 (1997).

[45] Particle Data Group, D.E. Groom *et al.*, Eur. Phys. J. C **15**, 1 (2000).

[46] OPAL Collaboration, G. Abbiendi *et al.*, Report No. OPAL Physics Note PN455 (August 2000); see also L3 Collaboration, M. Acciarri *et al.*, Phys. Lett. B **503**, 10 (2001).

[47] A.D. Martin, R.G. Roberts, W.J. Stirling, and R.S. Thorne, Eur. Phys. J. C **4** , 463 (1998).

[48] CTEQ Collaboration, H.L. Lai *et al.*, Eur. Phys. J. C **12**, 375 (2000).

[49] F. Bloch and A. Nordsieck, Phys. Rev. **52**, 54 (1937).

[50] G. 't Hooft, Nucl. Phys. B **33**, 173 (1971).

[51] G. 't Hooft, Nucl. Phys. B **35**, 167 (1971).

[52] Nucl. Phys. B **51**, 125 (1973) [Erratum-*ibid.* B **58**, 643 (1973)].

[53] W. J. Marciano and A. Sirlin, Phys. Rev. D **22**, 2695 (1980) [Erratum-ibid. D **31**, 213 (1985)];
A. Sirlin, Phys. Rev. D **22**, 971 (1980);
A. Sirlin and W. J. Marciano, Nucl. Phys. B **189**, 442 (1981).

[54] J. C. Taylor, Nucl. Phys. B **33** (1971) 436;
A. A. Slavnov, Theor. Math. Phys. **10**, 99 (1972) [Teor. Mat. Fiz. **10**, 153 (1972)].

[55] T. Muta, World Sci. Lect. Notes Phys. **5**, 1 (1987).

[56] K. G. Chetyrkin, B. A. Kniehl and M. Steinhauser, Nucl. Phys. B **510**, 61 (1998).

[57] H. Lehmann, K. Symanzik and W. Zimmermann, Nuovo Cim. **1**, 205 (1955).

[58] G. Altarelli and G. Parisi, Nucl. Phys. B **126**, 298 (1977).

[59] A. Bassetto, M. Ciafaloni, G. Marchesini and A. H. Mueller, Nucl. Phys. B **207**, 189 (1982);
M. L. Mangano, S. Parke and Z. Xu, Nucl. Phys. B **298**, 653 (1988);
M. L. Mangano and S. J. Parke, Phys. Rept. **200**, 301 (1991).

[60] M. A. Nowak, M. Praszalowicz and W. Slomiński, Ann. Phys. (NY) **166** (1986) 443.

[61] T. Wengler, Report No. hep-ex/0009043, to be published in the proceedings of 30th International Conference on High-Energy Physics (ICHEP 2000), Osaka, Japan, 27 July – 2 August 2000.

[62] S. Catani, Y. L. Dokshitzer, M. H. Seymour and B. R. Webber, Nucl. Phys. B **406**, 187 (1993);
S. D. Ellis and D. E. Soper, Phys. Rev. D **48**, 3160 (1993)

[63] G. Leibbrandt, Rev. Mod. Phys. **47**, 849 (1975).

[64] S. Dittmaier, private communication.

[65] A. Denner, Fortsch. Phys. **41**, 307 (1993).

[66] G. Passarino and M. J. Veltman, Nucl. Phys. B **160**, 151 (1979).

[67] R. Mertig, M. Böhm and A. Denner, Comput. Phys. Commun. **64**, 345 (1991).

[68] W. Beenakker, Ph.D.Thesis, Univ. Leiden, October 1989,

[69] J. A. M. Vermaseren, *Symbolic Manipulation with FORM*, (Computer Algebra Netherlands, Amsterdam, 1991).

[70] W. Beenakker, H. Kuijf, W. L. van Neerven and J. Smith, Phys. Rev. D **40**, 54 (1989).

[71] I. S. Gradshteyn and I. M. Ryzhik *Tables of integrals, Series, and Products- Enlarged Edition*, Academic Press, 1980.

[72] I. Bojak, Dissertation, Univ. Dortmund, April 2000 (unpublished).

ACKNOWLEDGMENTS

First of all I would like to thank Prof. Bernd A. Kniehl for offering me the opportunity to work up this thesis on a very interesting topic. Its structure is based on Prof. Bernd. A. Kniehl's generous support and helpful advice.

I am particularly grateful to Dr. Michael Klasen and Dr. Matthias Steinhauser for their collaboration on this project and for their advice in the every-day life. I have benefited a lot from their kindness to teach me and to share their knowledge with me. They have performed independent calculations for most of the results presented in this thesis. I would also like to thank them for carefully reading the manuscript and giving me plenty of useful suggestions.

Special thanks to Dr. Simon Albino for reading the manuscript and for helping me to improve the English of the thesis.

I would also like to thank my colleagues Fantina Madricardo and Stefan Berge for the pleasant time spent together and for the interesting physics discussions we had throughout these years.

Multumesc parintilor mei pentru suportul moral si dragostea transmise in fiecare zi, in ciuda distantei ce ne desparte.

Multumesc celui care a avut puterea sa-mi ramana alaturi pe drumul lung si adeseori anevois ce l-am avut de parcurs pana aici.